CRITICALITY IN CELLULAR MEMBRANES AND THE INFORMATION GEOMETRY OF SIMPLE MODELS

A Dissertation

Presented to the Faculty of the Graduate School

of Cornell University

in Partial Fulfillment of the Requirements for the Degree of

Doctor of Philosophy

by

Benjamin Brooks Machta

January 2013

CRITICALITY IN CELLULAR MEMBRANES AND THE INFORMATION

GEOMETRY OF SIMPLE MODELS

Benjamin Brooks Machta, Ph.D.

Cornell University 2013

This thesis is divided into two parts. Chapters 2-5 describe work on the statistical physics of cellular membranes, motivated by experiments that suggest they are tuned close to a two dimensional liquid-liquid critical point. Chapter 6 describes work towards an information theoretic understanding of how simple effective descriptions emerge out of systems with complicated microscopic details. Chapter 1 gives a detailed introduction to both of these topics.

Chapter 2 presents a minimal model for a cellular membrane consisting of a nearly critical two dimensional fluid coupled to a fixed cortical cytoskeleton. We argue that proximity to criticality is thermodynamically necessary to explain the presence of heterogeneity at $10 - 100$nm, as is commonly observed in experiments. We further show that this model naturally recapitulates many of the findings in the membrane 'raft' literature.

In chapter 3 we argue that proximity to criticality in the membrane is distinguished, in part, by the presence of long ranged critical Casimir forces that act between membrane bound proteins. We estimate the form of this potential using several techniques, and show that it is expected to be $\sim k_B T$ over tens of nanometers. We further argue that these forces could be playing important roles in cellular processes.

In chapter 4 we show that the dynamics of synthetic membranes tuned close to a critical point are in a newly predicted universality class particular to two

dimensional liquids immersed in a three dimensional, non-critical, bulk fluid. With just a single free parameter, a model for this universality class quantitatively describes all of the observable time dependent correlation functions.

In chapter 5 we explore the possibility that general anesthetics act by taking the membrane away from its liquid-liquid critical point. We present experimental evidence that shows that general anesthetics do indeed depress the critical temperature (T_c) in cell-derived vesicles by approximately 4K. In addition, we show that a receptor allosterically regulated by the membrane's composition *could* be sufficiently disrupted by this change in T_c to explain the most relevant phenomenology of anesthesia- that certain ligand-gated ion channels have their response to ligand dramatically potentiated.

In chapter 6 we apply an information theoretic framework to two models from statistical physics, where we see the emergence of a continuum description of diffusion and of the universal behavior seen at the Ising critical point. As these develop, we find that a characteristic hierarchy of parameter importance emerges, similar to that seen in 'sloppy' models from systems biology and elsewhere.

BIOGRAPHICAL SKETCH

The author grew up in Amherst, Massachusetts, the son of Jon Machta and Betsy Brooks. His love of physics was nurtured from an early age, especially by his physicist father and a family which valued curiosity and always encouraged him to follow his interests. Through high school, at Amherst Regional, his interests mostly consisted of physics, photography and life in the outdoors. Ben attended Brown University from 2002-2006, earning a B.Sc. in Physics and developing an interest in neuroscience.

Ben began his studies at Cornell in 2006. He joined Jim Sethna's group, where he has happily spent the last several years. After graduation, he plans to start as a postdoctoral fellow at the Lewis-Sigler Institute for Integrative Genomics at Princeton University.

To my sister, my parents, and my grandparents.

ACKNOWLEDGEMENTS

her, first by watching her design and carry out experiments, and later by helping her do the same while working in her new lab in Ann Arbor, Michigan. She showed me how to critically read experimental papers in biology and how to think about what the right next steps, both experimental and theoretical. In addition to being a wonderful mentor, she and Erin Hunter welcomed me into their home in Ann Arbor for several wonderful months during which we made much progress on several of the chapters in this work. I hope that our ongoing projects can continue as a collaboration during my post-doc.

Finally I must thank Jim Sethna. I could not have asked for more from an advisor. Jim is always up for a discussion of whatever is on my mind, and he brings an unparalleled creativity and joy to the process. He encourages, reworks and refocuses even my silliest ideas, and after a good meeting it is often hard to identify which ideas were mine and which were his. His tireless, positive attitude always motivates me to do better. If I am lucky enough to have students of my own some day, I will strive to give them as much of an opportunity to develop their interests as Jim does. I hope that this marks only the end of formal advising from Jim, but not the end of our collaboration.

<h1 style="text-align:center">TABLE OF CONTENTS</h1>

LIST OF FIGURES

CHAPTER 1

INTRODUCTION

What general statements can be made about the physics of biological sys-
tems? Since the decline of explanations for life involving a vital essence, there is
agreeement that biological systems obey and are limited by the same fundamen-
tal laws of physics that govern the motion of rocks, elementary particles and
superconductors. However, just as a beautiful theory of superconductors re-
quires physics that cannot be easily derived from a quantitative understanding
of the underlying particles that make them up [2], we should expect that simple
yet quantitative theories in biology will also involve mathematical formalism
and physical quantitates that do not appear in descriptions of their microscopic
components.

One area of physics which very dramatically limits biological systems is
thermodynamics and statistical physics. The first two laws of thermodynam-
ics state that while energy must be conserved, the entropy of the universe must
increase, on average, as any physical process proceeds. Biological systems obey
these laws in the sneakiest of ways- they carry out an agenda which seems at
many levels to be reducing entropy, turning microscopic building blocks into
ordered strands of DNA and broadly organizing their microscopic components
into structures that seem to be more ordered than their inputs. They do this
by ensuring that each seemingly entropy reducing step is coupled to the move-
ment of energy from a high temperature bath (eventually in the form of photons
from the sun) to a low temperature bath (waste heat here on earth). In this re-
spect, biological systems are somewhat analogous to a heat engine, like the one
that drives a car. They are certainly subject to the same constraints relating the

amount of work it can do given a fixed amount of chemical energy.

However, other statistical issues that biological systems face seem to have few parallels with familiar statistical mechanical problems. What sets the accuracy with which your brain can determine that a face is familiar? How well can the immune system distinguish a chemical signature of an invading pathogen from a native 'self' part? At a more microscopic level, how much free energy must be expended to accurately copy the information in a DNA strand?

A recent approach has focused on using the tools of information theory [123, 25] to analyze statistical noise in biological systems [136, 137, 138, 163, 9, 10, 38, 54]. This approach seems very natural. The eventual goal of an organism (or its genes) is to produce copies of itself that faithfully contain the information for making more copies. At a smaller level, all cells are involved in information processing to varying degrees. A neuron, most obviously, must take input from a variety of different sources and decide when to fire an action potential [94]. Immune cells must survey their chemical environment and detect signs of foreign substances and infection. Even muscle cells must contract reliably only after receiving proper signals from other cells, and they must adjust their metabolism accordingly. At the molecular level proteins must appropriately respond to chemical signals. For example, ion channels in neurons must open and close according to the electrical potential across the membrane, the chemical potential of various second messengers like calcium and the presence of specific signaling molecules. They must do this processing in the presence of substantial noise coming from (for example) the shot noise associated with the need to detect a concentration through the diffusion of individual particles [10, 38], and thermal noise associated with the need to distinguish chemical

specificities which are frequently of order $k_B T$ [72, 133, 63].

My thesis can be roughly grouped into two main areas each of which hopefully shed light on particular ways in which the statistical mechanics of biological systems are unique, and the ways in which they are similar to descriptions of models from other areas of physics. Chapters 2-5 focus on the statistical physics of cellular membranes. This work is motivated by an astonishing experimental finding- that the plasma membranes of cells seem to be tuned close to a 2D liquid-liquid critical point [147]. Although these critical points have been the focus of intense study in physics, cellular membranes are the first clear example of a system which seems to be *naturally* tuned close to a thermal critical point. The finding inspires a wide array of questions, which this thesis just begins to address. A more detailed introduction to this work is provided in section 1.1. Chapter 6 describes work towards a geometric framework for understanding the statistics of modeling. Why is it that the behavior of biological systems is often comprehensible, despite the enormous complexity and appearent randomness of its microscopic parts? A quantitative answer for this is suggested by the finding that effective models for these systems are often *sloppy* [59] with a hierarchy of importance in parameter space. Chapter 6 examines multi-parameter models from physics and shows how they become sloppy as they are observed at coarser scales. An introduction to that work is provided in section 1.2.

1.1 Statistical physics of cellular membranes

The plasma membranes of cells are complex two dimensional soups composed of thousands of different lipids and proteins arranged into a fluid bilayer. In addition to separating the inside of the cell from the outside, an enormous

number of chemical processes are carried out in the membrane itself. In particular, most signaling systems begin with the binding of a signaling molecule to a receptor, with the first few steps of the signaling cascade occurring at the membrane [65, 39, 124]. Early models assumed that membranes were uniform at lengths larger than a few nanometers, the natural length of a lipid, with lipids acting essentially as two-dimensional solvents for embedded proteins. A wide array of recent biochemical evidence suggests, surprisingly, that bilayers are actually heterogeneous with liquid structures ranging in size from a few to hundreds of nanometers [105, 90]. Early evidence came from studies that showed that certain detergents extracted a reproducible subset of membrane bound components, leaving the rest intact [96]. Since then, a wide range of techniques have seen evidence of these structures [121, 160, 107].

There is also accumulating evidence for their role in regulation, particularly in signaling [129, 120, 90, 65, 67, 127, 4]. Cholesterol depletion and other experimentally induced lipid perturbations can have profound implications on functional signaling outcomes. Furthermore, the addition of signaling molecules typically leads to changes in the spatial distribution of receptors, often initiating clustering of specific components including receptors, and other necessary downstream components, while excluding inhibitors in a manner sensitive to lipid perturbations [143, 145]. Perhaps most striking, experiments from the Baird-Holowka group performed with structurally defined trivalent DNA ligands [67] showed that signaling outcomes are strongly dependent on the spatial separation of the binding sites.

In parallel, work in Giant Plasma Membrane Vesicles (GPMVs, see figure2.1B) isolated from living cells have shed light on the physical mecha-

nisms underlying these biochemical findings. The first such study [6] showed that by cooling these GPMVs below room temperature, they would phase separate into two macroscopic liquid phases. This has not been observed in intact cells, which we argue is due to interactions with the cytoskeleton (Chapter **??** and [93]). Precedence for this type of phase separation is found in synthetic systems of three components where the two phases are termed liquid ordered and liquid disordered and are determined primarily by the packing of the lipid chains, with fully saturated lipids and cholesterol prefering the liquid ordered phase [150, 146, 71]. Quite surprisingly, further studies of these GPMVs showed that they pass very near to a critical point in the Ising universality class on the way to phase separation [147]. This finding was quite unexpected; these critical points can be found in model membranes [150, 146] but require the careful tuning of composition and temperature (or of two composition controls at a given temperature). The Ising up-down symmetry is emergent at this critical point-the two liquid phases are quite different, and so both 'magnetization' (here related to the chemical potential of some combination of components) and 'reduced temperature' (a combination of temperature and the chemical potential of other components) must *both* be tuned.

In fact, the finding of criticality, though surprising, goes far in explaining the biological findings described above. Indeed, it solves a thermodynamic puzzle. The natural length scale of a lipid is 1nm. Given this, structures ∼ 10nm should cost enormous free energies to maintain. Far from a critical point, assuming an entropic cost of $k_B T$, with no balancing energetic cost, organizing a circular region of radius 20nm should cost roughly $400\pi k_B T$. Such a structure would also be very unstable in a liquid membrane, presumably disintegrating by diffusion (typically $D \approx 1\mu m^2/s$) giving a lifetime of around $1ms$. However, near a crit-
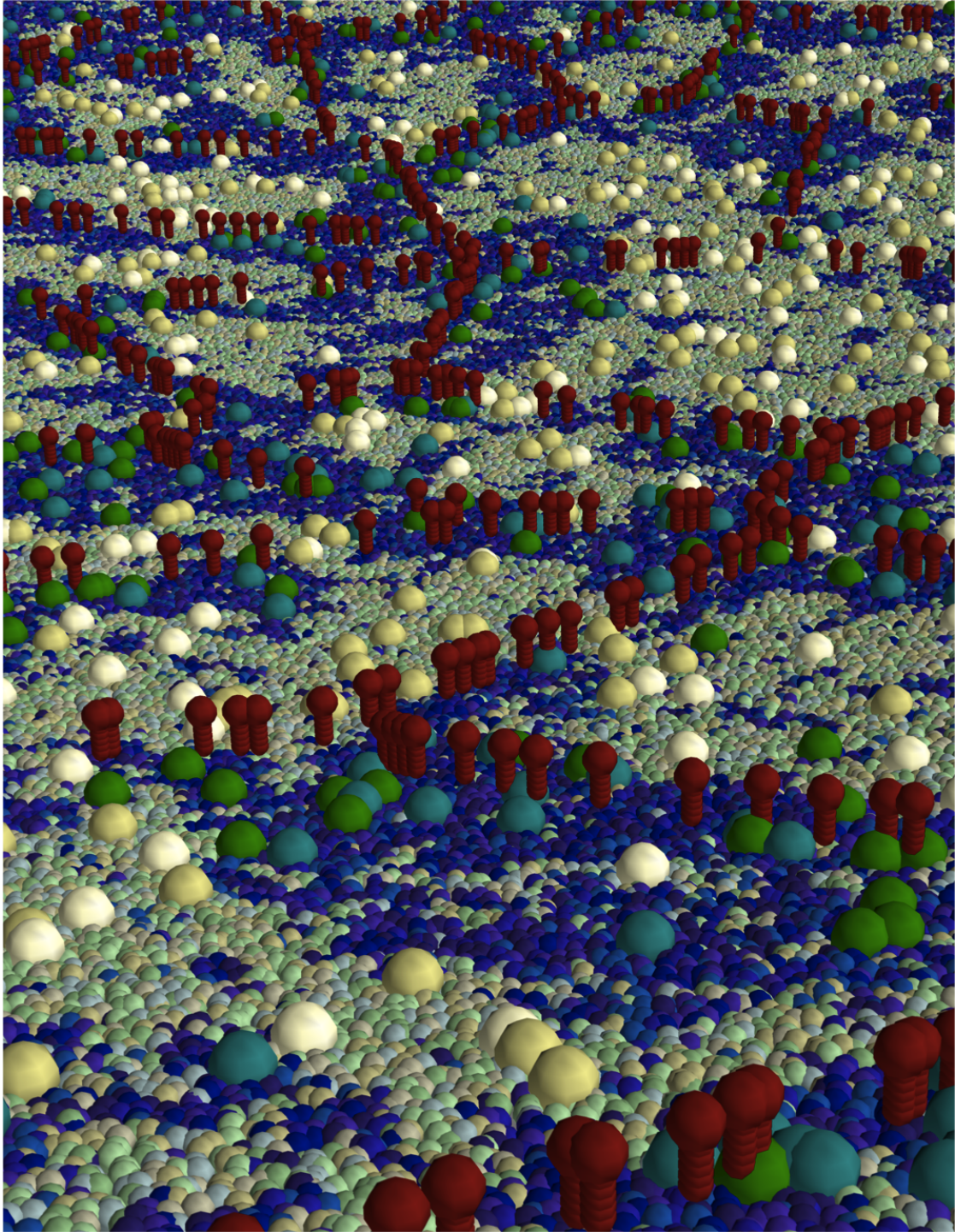
Figure 1.1: We predict that the membrane is heterogeneous with fractal puddles enriched in specific components (light vs dark here) all coupled to a rigid cytoskeletal meshwork (red posts). In chapter 2 we show that this model naturally explains many of the mysteries in the literature of biological membranes.

ical point, we expect to see structures of this size as manifestations of critical phenomenon. In [93] we propose a model (shown pictorially in figure 1.1 and described in detail in chapter 2) wherein these critical fluctuations, coupled to the underlying cytoskeleton are responsible for the large and long-lived structures seen in the biological literature.
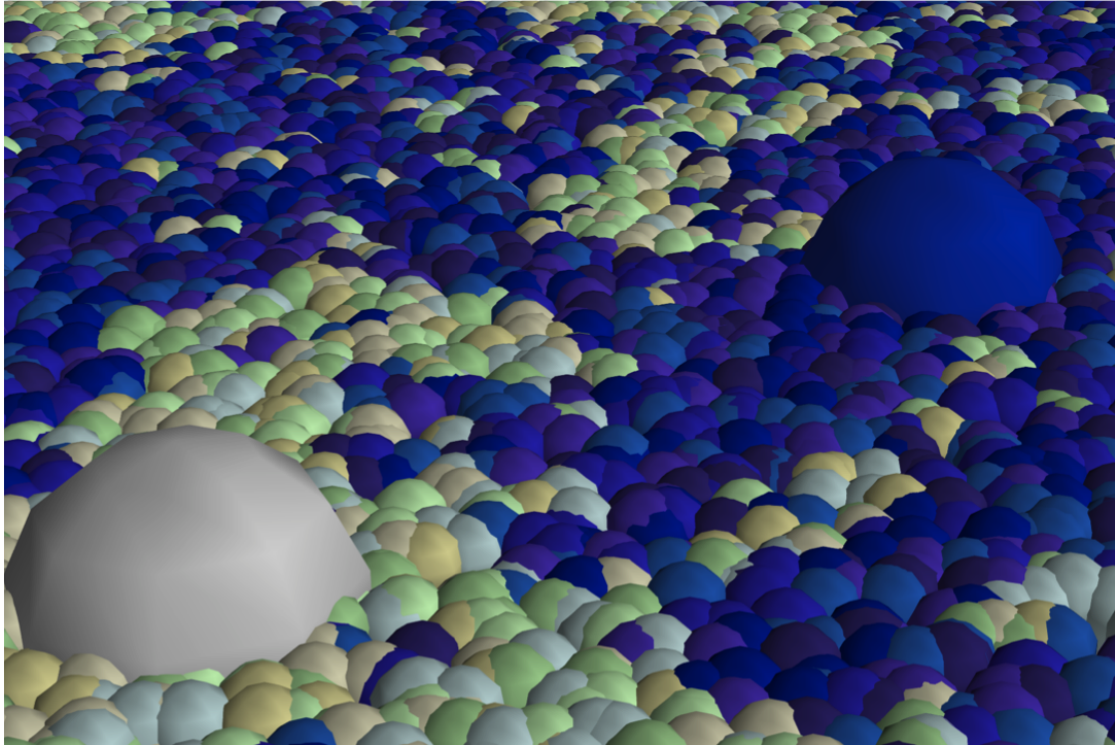
Figure 1.2: In Chapter 3 we show that membrane bound proteins feel an effective force mediated by critical composition fluctuations of the membrane itself. We show that this force decays over a length of roughly $\xi \sim 20$nm, much longer ranged than electrostatic interactions which are screened over less than 1 nm in the ion rich environment of the cytoplasm.

How could a cell make use of such proximity to this critical point? A wide variety of systems are thought to make use of 'lipid rafts' and we would like to say that most of these processes are, by extension, making use of the proximity of the cell to criticality. The hypothesis that criticality mediates these effects allows more specific statements to be made. In chapter 3 we explore the pos-

sibility that proximity to criticality allows proteins to exert forces on each other over tens of nanometers. Although the magnitude of this potential is of order the thermal energy, $k_B T$, it is much longer ranged than more familiar electrostatic forces which die off over ~ 1nm in the highly screened ionic environment of the cytoplasm. This membrane-mediated force could profoundly influence signaling cascades, and it seems possible that the cell could make use of it to allow for information from a large number of receptors to be more rapidly and efficiently integrated.

Alternatively, one could imagine that proteins embedded in the membrane are able to directly read out the membrane's order parameter, or composition, by coupling its functional state to its boundary conditions with the surrounding membrane. Proteins subtly change their structure, or allosteric state, either in response to changes in their environment, or upon their modification by a non-equilibrium event (such as phosphorylation). The prototypcical example of the former is hemoglobin [79], which changes its affinity for oxygen in response to pH (and by extension CO_2 levels) to more efficiently deliver oxygen to more active tissues. Other proteins are allosterically sensitive to calcium levels, voltage (for membrane bound proteins), and a plethora of other local conditions. There is evidence that membrane bound proteins are allosterically mediated by the composition of the membrane they are in, and, perhaps by extension, the local Ising fluctuations. Soubias et. al. [131], showed that Rhodopsin, (a G-protein coupled receptor sensitive to light) adjusts the height of its membrane spanning region to conform to its surrounding lipids, and that further, its efficiency at transducing signals is strongly dependent on its lipid environment. More circumstantial evidence comes from general anesthesia, whose affects are thought to be exerted through the allosteric modification of membrane bound ion chan-

nels. There is considerable controversy as to whether this effect is directly mediated by the anesthetics, or as a secondary effect mediated by the membrane itself [58]. In chapter 5 we show that one effect of anesthetics is to move the membrane away from its liquid-liquid critical point. We further argue that this change could have a profound affect on a membrane protein which makes use of the critical point for allosteric regulation. In particular, we show that an ion channel with particular boundary conditions would be ~ 50% more sensitive to its natural ligand under anesthetic conditions, roughly in agreement with the findings of the anesthetic literature.

Pressing questions about the statistical physics of membranes remain unanswered by this thesis. Should we expect other cellular systems to be close to thermal critical points? Work by Bialek and collaborators [98] has suggested that biological systems are often tuned close to statistical and other more broadly defined critical points, although we are not aware of any other biological systems that seem poised at analogous thermal critical points. In addition, a quantification of the usefulness of criticality remains elusive. Why should the cell use critical forces to communicate between receptors, rather than by producing second messengers or by simple diffusion? Are there general reasons why a cell might want to have its statistical state spatially entangled, as happens near the Ising critical point [1]? Finally, it would be interesting to understand, mechanistically, how cells tune their membrane close to a critical point. I hope that I can help answer these questions in future work.

---

[1]This was suggested by Paul Ginsparg, and despite much musing and discussion I think that that the details in this thesis offer only a partial answer to the question.

1.2 Information geometry and Sloppy models

Biology is extremely complicated at the molecular level. Composed of thousands of types of molecules diffusing and carrying out complicated reactions, a microscopic characterization of the full behavior of a single cell at the microscopic level is surely an impossible task. Nonetheless, certain aspects of the behavior of biological systems can be very predictable. Indeed, models often quantitatively describe their behavior without any reference to the individual molecules that make up the system.

Work by Jim Sethna's group quantified this and shed some light on how it occurs, by considering the dependance of observable data on the parameters of seventeen models from the system's biology literature [59][2]. They found that all of these models had a very striking hierarchy of importance in parameter space. They quantified this structure by finding the best fit to data for a particlar model, where the gradient of the cost with respect to parameters is 0. At that point they looked at the Hessian, the second derivative of the cost with respect to all parameters. They found that in each model the Hessian has a characteristic 'sloppy' structure (see figure 1.3). A few 'stiff' parameter combinations have large eigenvalues, corresponding to directions in parameter space that can be readily inferred from data: in these parameter space directions, a small change leads to a large increase in the cost. The remaining 'sloppy' directions are progressively harder to measure, with each successive direction harder to measure by a similar amount from the previous one.

Mark Transtrum, Jim Sethna and I [139, 140] developed a geometric frame-

---

[2]Indeed, the sloppy spectrum they found is not limited to biological systems, and can also be found in the parameter dependance of quantum Monte-Carlo and in interatomic potentials, as well as in a wide range of models with many parameters.
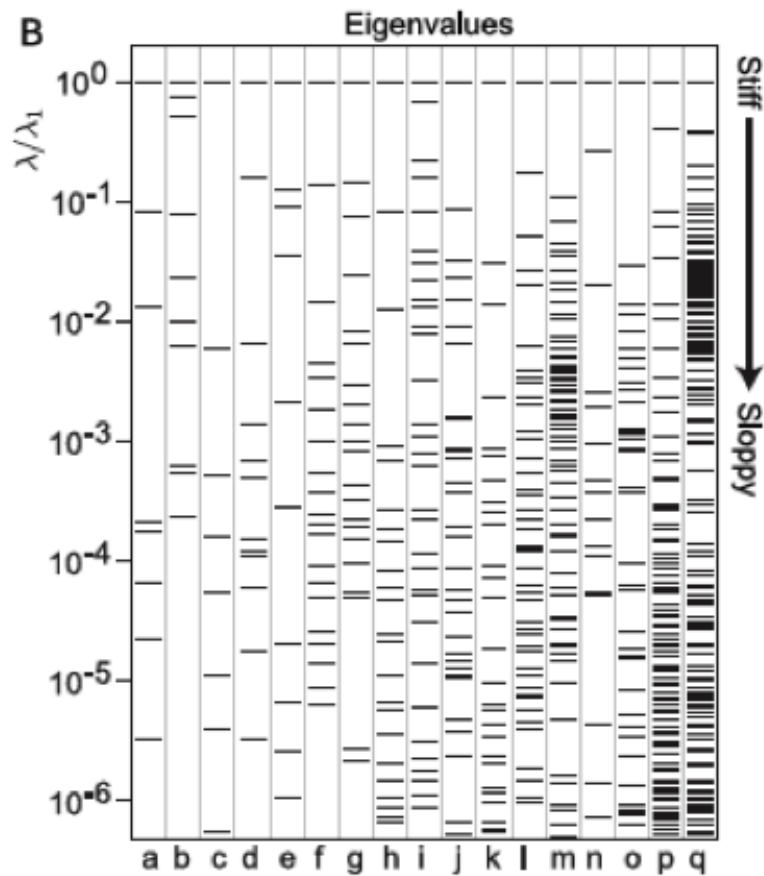
Figure 1.3: Eigenvalues of the Hessian are evenly spaced in log in seventeen models from the systems biology literature (a-q). This spectrum implies a hierarchy of importance in parameter space. Some 'stiff' parameter combinations can be inferred with may orders of magnitude more precision than other 'sloppy' ones. Figure is from Gutenkunst et. al. [59] on which I am not an author.

work to answer additional questions about this structure. Firstly we wanted to demonstrate that it was not simply the result of a bad choice of parameterization. Often, model parameters can have different units, and we wanted to ensure that the observed sloppy spectrum wasn't merely an artifact of our particular choice of parameter labeling. To do this we used information geometry [1] to define a manifold of possible models (a mathematical derivation of this is provided in chapter 6) whose shape transcends the particular choice of

Figure 1.4: Three dimensional cross-sections of the model manifold (see figure 1.6 for two alternative views) for a model consisting of a sum of exponentials. Each direction of the model corresponds to the value of the function $F(t) = \sum_\mu A^\mu \exp(-t/\tau^\mu)$ for a particular t, where As and τs are model parameters constrained to be greater than zero. The model has a characteristic 'hyperribbon' structure, with a long direction, a medium width and an extremely thin third direction. Notice that all points inside of the model manifold are 'close' to a model boundary, where some parameter(s) are infinite or 0. Figure is from Transtrum et. al. [139]

parameters that label it, much as the shape of the surface of the earth transcends the longitude and latitude lines we use to label it.

We found that typical manifolds have a characteristic 'hyper-ribbon' structure (see figure 1.4). This structure shows that the local parameter hierarchy is mirrored in a hierarchy of importance in the set of all possible models. Some directions in model space can be followed for long distances, defining a large one-parameter ensemble of possible models. Other directions quickly lead to model boundaries, where some parameters have become infinite (or zero) without dramatically changing model behavior [3]. We furthermore showed that the widths are roughly proportional and aligned with the Eigenvalues and Eigenvectors of the Hessian, which, as we will see forms a metric on the model manifold (see figure 1.5 and chapter 6)

In addition, our geometric approach led to a deeper understanding of why these models so often have this hyper-ribbon, or sloppy structure. In [139] we argued that typical presentations of data in least squares problems *constrain themselves*. Such data often come in the form of a time-series, or other continuous function sampled at discrete points. Presuming that this function is smooth, constraining the value of the data at a few points can dramatically constrain the value that the function can take at other points (see figure 1.6). Constraining the value of the function at a point corresponds to taking a cross-section of the model manifold, and this immediately implies that cross-sections of the model tend to be much thinner in their longest direction than the manifold itself. In [139] we showed that this naturally leads to the hyper-ribbon structure so characteristic of multi-parameter models.

---

[3]Mark Transtrum is currently exploring the intriguing possibility that these boundaries can be used to make an automatic procedure for model reduction- by iteratively moving to the closest model boundary
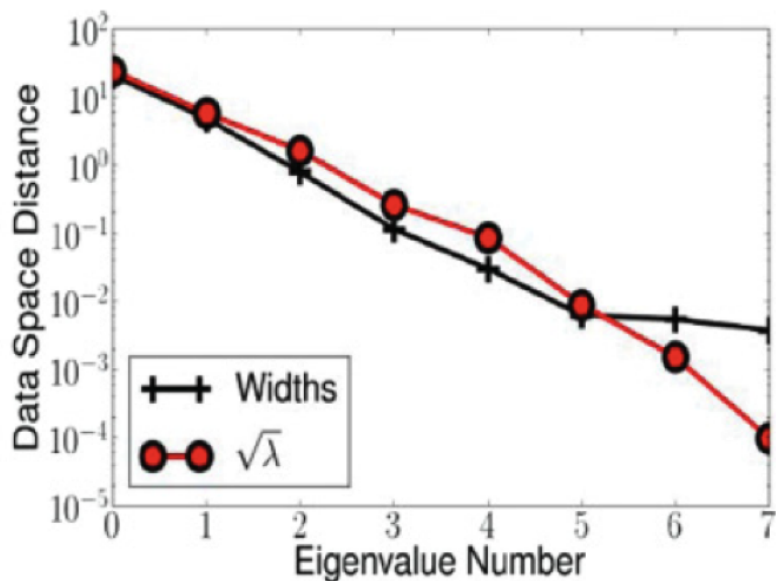
Figure 1.5: In an 8 dimensional model in which four exponentials are summed, the manifold's widths are mirrored in the eigenvalues of the Hessian, which forms a metric on the model manifold(see chapter 6). Figure from Transtrum et. al. [140]

The implications of this sloppy structure are manyfold. Firstly, it means that it is possible to make predictive models without complete, or even partial knowledge of the underlying microscopic details of a system. In our view, modeling is best thought of as constrained interpolation, and 'good' data should be expected to constrain possible model behavior to a small region of the model manifold, but not necessarily to a small region of parameter space. As such, we also predict that most microscopic parameters cannot be inferred from data.

The work presented in chapter 6 attempts to connect these findings to models from physics, where a similar hierarchy is also often present. Continuum limits describe many systems with seemingly very different underlying details. For example, the collective behavior of a large number of molecules is often described by the continuum limit of a liquid, with the macroscopic parameters of density, viscosity and compressibility being the only ones needed to describe
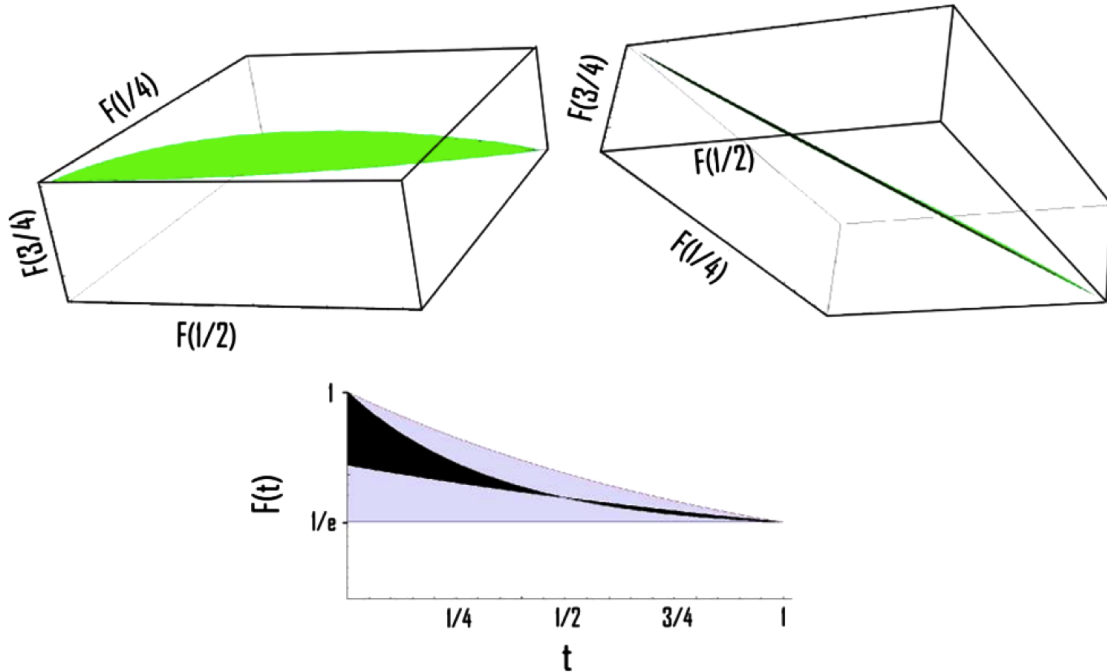
Figure 1.6: Typical data constrains itself naturally leading to the hyper-ribbon structure of typical model manifolds. The possible value of a sum of exponentials $F(t)$ with positive decay rates is shown, under the constraints that $F(0) = 1$ and $F(1) = 1/e$. Constraining the value at $F(1/2)$ dramatically restricts the values that F can take nearby (in black), leading to a hierarchical hyper-ribbon structure. Figure from Transtrum et. al. [139]

most observable phenomenon. Just as in typical systems biology models, these effective parameters are not related in any obvious way to microscopic parameters. The viscosity of water, for example, would be extremely difficult to calculate from a molecular level description of water, and, conversely, we wouldn't dream of trying to infer molecular details of water by measuring the rate at which different objects fall through it under gravity. In chapter 6 we show that the typical ways that our measurements are limited, by spatial or temporal blurring, selectively and anisotropically blur information about molecular level details. The result is that coarsened data often leads to a model manifold with a similar sloppy spectrum to that seen in least squares problems.

CHAPTER 2

CRITICALITY AND THE CYTOSKELETON

Abstract [1] - We present a minimal model of plasma membrane heterogeneity that combines criticality with connectivity to cortical cytoskeleton. Our model is motivated by recent observations of micron-sized critical fluctuations in plasma membrane vesicles that are detached from their cortical cytoskeleton. We incorporate criticality using a conserved order parameter Ising model coupled to a simple actin cytoskeleton interacting through point-like pinning sites. Using this minimal model, we recapitulate several experimental observations of plasma membrane raft heterogeneity. Small ($r \sim 20$nm) and dynamic fluctuations at physiological temperatures arise from criticality. Including connectivity to cortical cytoskeleton disrupts large fluctuations, prevents macroscopic phase separation at low temperatures ($T \leq 22^o$C), and provides a template for long lived fluctuations at physiological temperature ($T = 37^o$C). Cytoskeleton-stabilized fluctuations produce significant barriers to the diffusion of some membrane components in a manner that is weakly dependent on the number of pinning sites and strongly dependent on criticality. More generally, we demonstrate that critical fluctuations provide a physical mechanism to organize and spatially segregate membrane components by providing channels for interaction over large distances.

2.1 Introduction

It is hypothesized that the fluid plasma membranes of mammalian cells are heterogeneous over distances much larger than the nanometer size typical of their lipid and protein components [128, 3]. Furthermore, it is thought that this heterogeneity, often called lipid rafts can impact the localization and dynamics of membrane bound proteins involved in functional processes [83, 35, 128, 3]. The physical origins and functional significance of this structure are contentious [101, 35], and the hypothesis itself poses a thermodynamic puzzle: building an extended fluid region rich in specific membrane components should cost a free energy proportional to the regions area due to the loss of entropy. The same structure potentially gains free energy proportional to its area by bringing together components which have lower interaction energies. Both of these effects are of the order $k_B T$ per lipid area, where k_B is Boltzmanns constant and T is the temperature. Barring a remarkable cancellation, a domain with a size of 20nm would seem extremely unstable. Either the entropic contribution should win and the equilibrium structures should be much smaller, or energy should win, and the structures should be permanent and macroscopically phase-separated. One way a cell could make stable domains with dimensions in the tens to hundreds of nanometers is to carefully balance the entropic and energetic contributions, tuning the fluid membrane near to a miscibility critical point (Figure 2.1A). Under these conditions, structures with characteristic sizes much larger than individual molecules naturally emerge because the free energy required for their formation is near $k_B T$. When not exactly at the critical point these critical fluctuations are cut off at a size called the correlation length. In a simple system of two components, the two parameters that need tuning would typically be

temperature and the ratio of the two components; in multi-component model membranes or compositionally complex cell membranes at fixed temperature, these two parameters could be the molar fraction of any two components. Miscibility critical points, and their associated long-range critical fluctuations, have been observed experimentally in three component bilayer membranes containing cholesterol using a variety of methods [40, 68, 148, 150]. When membrane lipid composition is carefully tuned and temperature is set above the critical temperature, membranes are in a single yet heterogeneous liquid phase as verified by NMR and fluorescence microscopy [148, 68, 69, 150]. Below the critical temperature, membranes contain two distinct phases, called liquid-ordered and liquid-disordered. At temperatures below but close to the critical temperature, the line tension is small leading to undulations of domain boundaries (< 250nm) [40, 68]. In model membranes, manifestations of critical behavior are expected [5] (Figure 2.1A), near critical points [148, 150]. However, compositions must be carefully tuned to see this near-critical regime. For the vast majority of compositions, the miscibility transition is observed as an abrupt appearance of a second liquid phase either by lowering temperature or changing membrane composition [28, 149, 150].

Remarkably, there is experimental evidence that plasma membranes of mammalian cells have compositions tuned near to a critical point at physiological temperatures. Giant plasma membrane vesicles (GPMVs) isolated from living cells appear homogenous to light microscopy at 37^oC (310K), indicating that they are uniform at optical (250nm) length scales. However, below a critical temperature around 22^oC (295K), these vesicles phase separate into two macroscopic fluid domains [7]. Near the transition, GPMVs undergo equilibrium fluctuations that are visible at micron scales, in quantitative agreement with the
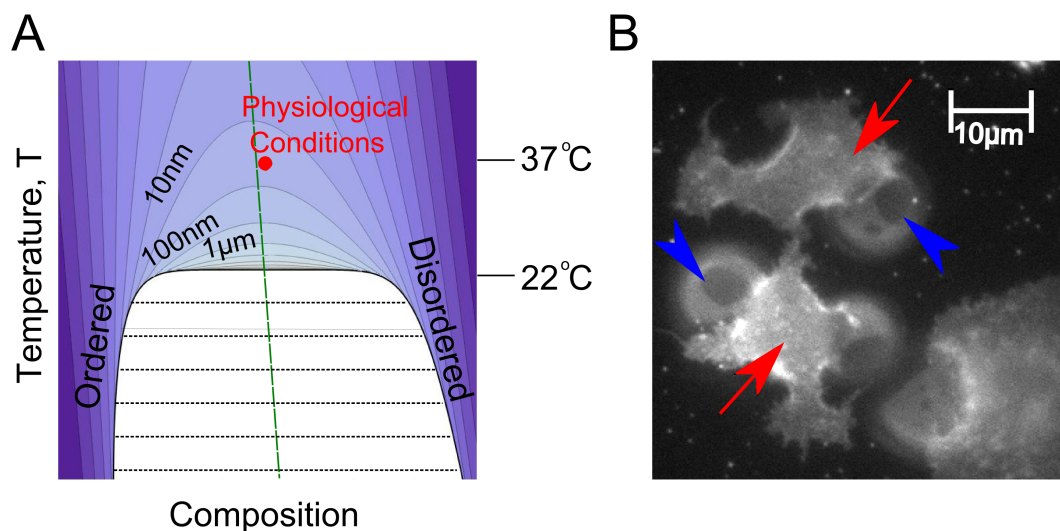
Figure 2.1: Ising criticality in the Plasma Membrane. (A) The model presented here assumes that cell plasma membranes are tuned to the proximity of a 2-D Ising critical point with a miscibility phase boundary given by the thick (black) line. Contours show regions of constant correlation length. Their shapes are identical for any system in the 2-D Ising universality class except for the slope of the rectilinear diameter (long-dashed (green) lines tilt, see Supplement), which describes how the fraction of phases changes with temperature. Experiments in GPMVs give a critical temperature around 22C and calibrate the contours [147]. Most simulations are conducted at the (red) point which is hypothesized to represent physiological conditions. (B) Below the critical temperature, intact plasma membranes on living cells appear uniform at optical length scales ((red) arrows), while attached plasma membrane vesicles are macroscopically phase separated ((blue) arrowheads point to phase boundaries). Detailed methods for (A) and (B) are provided in Supplementary Material at the end of this chapter.

fluctuations observed in purified model membranes carefully tuned to a critical point, as well as with theoretical predictions of two dimensional criticality [147]. One prediction that arises from this past GPMV study is that cell plasma membranes at physiological temperatures of 37°C (310K) reside only 5% above this critical point in the absolute Kelvin units natural to thermodynamics. This implies an experimentally extrapolated correlation length of roughly 20nm in GPMVs at 37°C (Figure 2.1A). This experimental result motivates the current simulation study. One major aim of our current work is to demonstrate that

criticality in plasma membranes, normally found only in carefully tuned laboratory environments, explains many experimental observations of membrane heterogeneity typically associated with lipid rafts. Plasma membrane vesicles differ from intact cell plasma membranes in many important ways; most notably, GPMVs lack connectivity to the cytoskeleton. In intact cells, the plasma membrane couples to cortical cytoskeleton through diverse and partially understood interactions [22, 114]. In addition to providing structural support, there is increasing evidence that the cytoskeleton plays a role in promoting lateral heterogeneity at the cell surface. It is widely speculated that connections to the cytoskeleton prevent the large-scale accumulation of membrane components into phase separated domains [7, 90, 65], even under conditions where phase separation is readily observed when membrane-cytoskeleton coupling is disrupted; macroscopic phase separation is easily observed in cell-attached GPMVs even as the remaining intact plasma membrane remains homogeneous (Figure 2.1B). Here we explore a minimal model for an intact plasma membrane coupled to its cortical cytoskeleton by taking advantage of a remarkable property of nearly critical systems called *universality* The shapes, sizes, and lifetimes of fluctuations depend only on the dimensionality of the system, the universality class, and the parameters that describe the relative proximity to the critical point (Figure 2.1A). Universality enables us to make quantitative predictions about compositionally complex cell plasma membranes through simulations of much simpler model systems. We stress that though cell membranes are not exactly at a critical point at 37^oC, they are tuned close enough to feel its universal features.

2.2 Methods

All simulations use a square lattice Ising model with a conserved order parameter implemented in the standard way. A detailed description of all methods can be found in Supplementary Material at the end of this chapter and are summarized below. Temperatures are calibrated by setting the critical temperature of the Ising Model to 295K. All simulations are performed on periodic $400x400$ arrays, with a pixel length corresponding to 2nm. Simulations performed to deduce static properties use non-local dynamics to decrease equilibration times. Dynamical simulations use Kawasaki dynamics supplemented with moves which swap like pixels at the same attempt frequency as unlike pixels. Simulation steps are converted into time using a conversion factor of approximately $D = 4\mu m^2/s$. Correlation functions are normalized to one at spatial infinity. We implement a cytoskeletal meshwork using a random, periodic, Voronoi construction to generate filaments that have a width of one pixel (1nm). The pinning sites are chosen randomly along these lines with constant density, which is 0.4 except in Figure 2.5 where it varies. A pixel sitting on a pinning site is constrained to be white. In diffusion experiments other white pixels are free to swap with pixels sitting on the pinning sites. Strongly coupled objects have infinitely strong interactions with their neighbors, forbidding any move which ends with a black pixel as a nearest neighbor to a strongly coupled white object or vice-versa. Modifications of the Ising Model have previously been used to model the thermodynamic properties of purified bilayer membranes in the vicinity of the main chain transition temperature [33], where there is some evidence of critical behavior [49]. In these models, while membrane composition is conserved, components are allowed to flip between two or more internal

states which in turn interact differently with neighboring components. We have chosen to implement a standard conserved order parameter 2D Ising model to model cell plasma membranes because it is the simplest possible model that incorporates criticality, because its behavior is in quantitative agreement with micron-sized fluctuations observed in isolated GPMVs and three component model membranes [147, 68], and because it represents the expected universality class for liquid-liquid phase separation (see section 2.6).

2.3   Results

2.3.1   Overview of the model

We model the plasma membrane using a 2D Ising model as described in Materials and Methods. In our model, membrane components such as lipids and proteins are represented as black or white pixels on a square lattice, where pixels of one type (e.g. white) correspond to components that tend to populate one membrane phase (liquid-ordered vs. liquid-disordered). We implement a conserved order parameter, meaning that the number of white (or black) pixels does not change with time. This model does not accurately reproduce the detailed arrangement of lipids and proteins that occur at very short distances less than several nanometers, since their arrangement will depend strongly on detailed molecular interactions. Consequently we choose to not refer to pixels as lipids or proteins. Though microscopically different, the Ising model will produce an accurate description of plasma membrane organization on larger distances, if our basic assumption of criticality holds. Though theory and experiment sug-

gest Ising criticality, we expect that our results would hold even if more exotic criticality turned out to be present in the system. They arise from a large correlation length and time, both of which are generically present in critical systems, and both of which have been directly observed in GPMVs [147].

In the Ising model, the critical point occurs when there are equal numbers of black and white pixels, with temperature tuned to the onset of phase separation. This corresponds to a membrane that has an equal surface area of liquid-ordered and liquid-disordered phase at the miscibility phase boundary. In most of this study, we assume that the plasma membrane has a critical composition, with a phase diagram similar to that shown in Figure 2.1A. We also assume that the surface fraction of phases does not change substantially with temperature. Such temperature dependence would lead to a tilt in the systems rectilinear diameter (green line in Figure 2.1A). In simulations this would manifest itself as a temperature dependent change in the ratio of black to white pixels. Though experimental observations of GPMVs show nearly equal fractions of coexisting phases at temperatures well below T_c(at experimentally observable $T_c - T \sim 10^o$C) we theoretically expect similar results even if this ratio were to show significant temperature dependence (see section 2.6).

We generate a cortical cytoskeleton network from a Voronoi construction (see Materials and Methods). In the results presented here we choose an average length of an actin defined region of 130nm which is in the range (41-230nm) found using electron microscopy techniques [99]. We model membrane-cytoskeleton connectivity by fixing individual pixels to be in a particular state at random sites along these filaments. These fixed pixels represent locations where membrane components, either proteins or lipids, are rigidly held through ei-

ther direct or direct interactions with cytoskeleton. At these positions, there is a strong preference for either liquid-ordered or liquid-disordered components. This could represent a membrane protein that strongly prefers to be surrounded by disordered phase lipids, or a lipid such as PiP2 that could prefer to be surrounded by either liquid-ordered or liquid-disordered phase components. We pin pixels of the same type (white), presuming that the interaction with the cytoskeleton tends to prefer one of the two low temperature phases. The linear density of pinning sites has not been determined experimentally and is a parameter that is varied in our model, along with temperature and composition.

This description of cytoskeleton-membrane coupling is simplistic, but we expect it to capture the qualitative behavior as long as connections on average prefer one of the two lipid environments. In plasma membrane vesicles, critical temperatures are typically near room temperature (T_c = 22^oC = $295K$) [147]. We primarily investigate physiological temperature, T = 37^oC = $310K$ = $1.05T_c$ where T_c is measured in Kelvin. To highlight the aspects of our model that arise due to proximity to a critical point, we include simulations at physiological temperatures for homogeneous membranes whose critical points are as low as 155K (T = $2T_c$).

2.3.2   Phase separation is disrupted in the presence of cortical cytoskeleton

Below Tc, in the absence of pinning, white and black pixels organize into domains that are half the size of the simulation box, indicating that the system is phase separated (Figure 2.2A). In the presence of cytoskeletal coupling, compo-
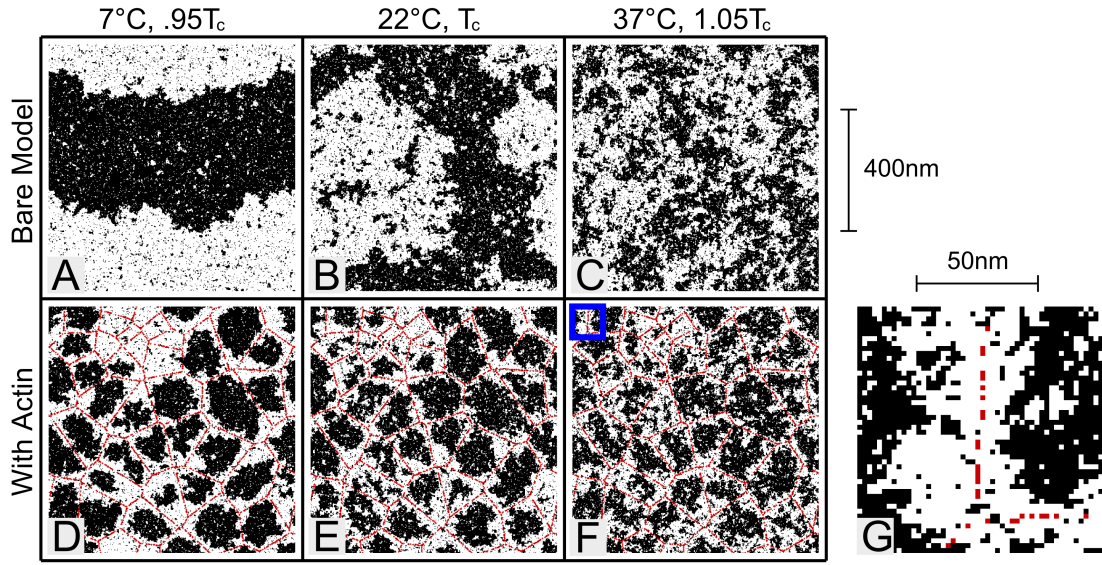
Figure 2.2: Membrane lateral heterogeneity is modulated by coupling to cortical cytoskeleton. Ising model simulations were conducted over a range of temperatures in the absence (A-C) and presence (D-F) of coupling to a cortical cytoskeleton meshwork. Red sites indicate locations where pixels are fixed to be white, mimicking a position where a lipid or protein is directly or indirectly connected to a fixed cytoskeleton. Below T_c the bare Ising model is phase separated (A). Long range order is disrupted when the model is coupled to cortical cytoskeleton (D) because the structure is cut off at the length of the cytoskeletal corrals. At Tc the bare model has structure at all length scales (B), whereas coupling to cytoskeleton cuts off the largest fluctuations (E). Above T_c, composition fluctuations that form in the bare Ising model (C) tend to localize along cytoskeletal filaments in the presence of coupling (F). (G) A higher magnification image (from boxed region in F) highlights that the cytoskeleton-preferring white phase forms channels around filaments with a width given roughly by the correlation length (20nm). The linear pinning density is 0.2 nm^{-1}.

nents instead follow the template of the underlying meshwork (Figure 2.2D). As a result, black and white pixels do not organize into domains that are larger than the characteristic size of the cytoskeletal corrals. If the average meshwork size is smaller than the optical resolution limit of light microscopy, as is the case in a variety of cell types (41-230nm) [99, 102], then our model predicts that intact cell plasma membranes would appear uniform even at temperatures where an isolated membrane would be phase separated (Figure 2.1B).

Our model is an example of a 2D Ising model with quenched (spatially fixed) random field disorder. A robust feature of the 2D Ising model [57] is that after the addition of any such disorder there is no macroscopic phase separation at any temperature. [2] This holds for arbitrarily weak (or in our case sparse) random fields or if different pixel types are held at each pinning site. The lack of macroscopic phase separation depends on the fixed anchoring of the pinning sites, since even slowly diffusing mobile components will not necessarily impede phase separation. A fundamental principle of statistical physics states that the dynamics of a system do not affect its static equilibrium properties. A consequence of this is that a slowly diffusing protein, if it is mobile at all, will still be able to partition selectively into the low temperature phases. Note that the GPMVs in Figure 2.1B contain substantial protein content. The addition of mobile components could either raise or lower the transition temperature depending on their microscopic interactions [132, 161]. We note that the quenched disorder implemented here is different from the annealed disorder investigated by Liu et al. [91] in which an actin meshwork was assembled on a pre-existing liquid-disordered domain. In this case, the authors observe that the actin meshwork stabilizes the liquid-ordered liquid-disordered phase separation. This is likely due to the presence of pinning sites occupying only a fraction of the membrane surface rather than covering the entire surface. This could be implemented in our simulations by allowing pinning sites to separate with the membrane phases.

---

[2]Consider the energy of inserting a domain of black pixels of finite size L into a region dominated by white pixels. In d dimensions, this incurs a line tension cost which is positive and scales like L^{d-1}. In the presence of a random field, there is also a random change in the energy. For large domains this random energy scales like $L^{d/2}$, the square root of the volume. For $d \leq 2$ this means that the insertion of an arbitrarily large domain can lower the energy of an ordered phase of the opposite type, so that macroscopic phase separation does not occur.

2.3.3 Membrane fluctuations mirror the underlying cytoskeleton at physiological temperature.

In the absence of coupling to cytoskeleton, large composition fluctuations occur in simulations because the free energy cost of assembling a cluster with dimensions of a correlation length is roughly the thermal energy $k_B T$. At the critical temperature the correlation length is very large (in principle infinite, but cut off at the size of the simulation box, Figure 2.2B), whereas at $1.05T_c$ the correlation length is roughly 10 lattice spacings (Figure 2.2C). We equate one lattice spacing with 2nm, to be in agreement with the extrapolated correlation length in GPMVs at 37^oC. When simulations are coupled to cortical cytoskeleton, the presence of the pinning sites disrupts the largest fluctuations (Figure 2.2E,F). More strikingly, coupling to cytoskeleton entrains channels of white, leaving puddles of black pixels in the center of each cytoskeletal corral (Figure 2.2G). This occurs even though the cytoskeleton only interacts with the membrane at local pinning sites. The effect propagates over roughly a correlation length because the system is near a critical point.

We examine the extent of cytoskeleton-induced membrane heterogeneity in our model by averaging many snapshots like those shown in Figure 2.2. Figure 2.3A shows the time-averaged pixel value at each location in the image. Continuous and wide channels of white pixels follow the underlying filaments that make up the cytoskeleton. In simulations where the critical temperature is well below physiological temperatures (Figure 2.3C, $T_c = 120^o$C), the remaining channels of white spins are thinner, have gaps, and their contrast is dramatically reduced. This highlights that robust channels arise only when the membrane is tuned close to a critical point. Our observations are quantified by

27
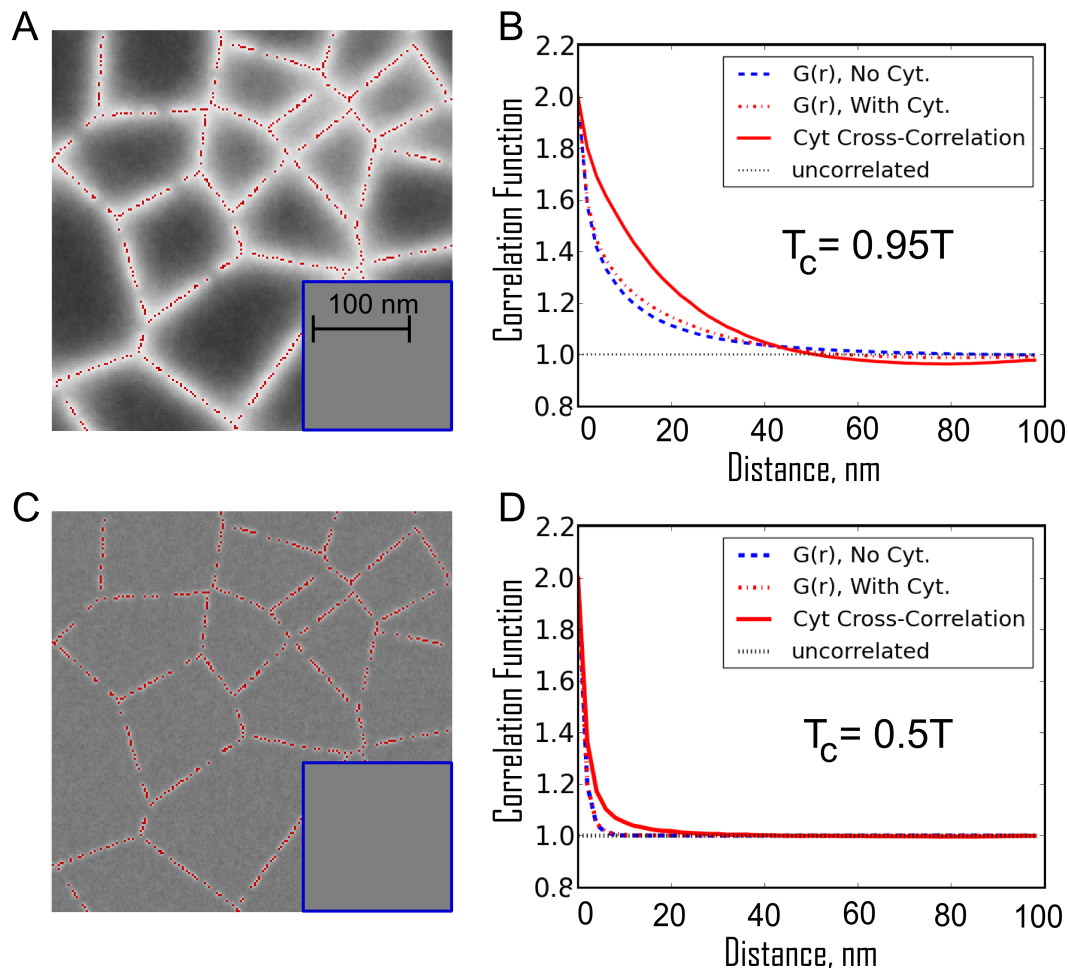
Figure 2.3: Coupling to cytoskeleton acts to entrain channels of white pixels over filaments, leaving pools of black pixels within cytoskeletal corrals. (A) The time averaged density of white pixels is correlated with the position of the cytoskeleton at 37^oC ($1.05T_C$). In the absence of cytoskeletal coupling (inset) the average density is trivially uniform. (B) The spatial auto-correlation function, $G(r)$, is not significantly altered by the presence of cytoskeletal coupling (compare dashed (blue) and dot-dashed (red) lines). In each case $G(r)$ decays over a correlation length of roughly 20nm. In addition, the spatial cross-correlation function between white pixels and pinning sites (solid (red) line) indicates that long range correlations extend over roughly one correlation length. (C) In a hypothetical membrane not tuned to the proximity of a critical point at 37^oC, but instead with a critical temperature of -120^oC, the channels gathered by the cytoskeleton are much thinner, and their contrast is diminished. This is the expected behavior for a well mixed membrane not near a critical point. (D) All of the corresponding correlation functions decay over a much shorter distance.

28

evaluating pair auto-correlation functions, $G(r)$, for the nearly critical case (Figure 2.3B) and for the far-from-critical case (Figure 2.3D). Pixels are significantly auto-correlated in simulations performed near criticality in the presence or absence of coupling to cortical cytoskeleton, and have roughly the same shape (dashed lines in Figure 2.3B). In simulations that are coupled to cytoskeleton, we also evaluate cross-correlation functions between membrane pinning sites and white pixels (solid lines in Figure 2.3B,D). In simulations near the critical point there is an increased probability of finding a white pixel out to a distance of around a correlation length ($\sim 20nm$) from a pinning site (Figure 2.3B). These long ranged correlations between the pinning sites and white pixels fill in gaps in the meshwork making the continuous channels shown in Figure 2.3A. In simulations far from criticality (Tc=0.5T), both the auto-correlations and cytoskeleton cross-correlations fall off over a few nm due to the short range of the lipid mediated effective interactions (Figure 2.3D). These auto and especially cross-correlation functions are predictions of our model that can be measured experimentally.

2.3.4   Cytoskeleton stabilized membrane heterogeneity is long lived

The lifetimes of typical fluctuations become increasingly long as the critical point is approached [64]. In order to investigate this critical slowing down in our model, we implemented locally-conserved order parameter dynamics, where pixels may only exchange with their four closest neighbors. A microscopic diffusion constant of around $D = 4\mu m^2/s$ was used to convert between

simulation steps and seconds. This value is in the range of values reported in studies looking at the diffusion of lipids at very fast time- or distance-scales [99]. Our dynamics assume that the composition is locally conserved while momentum is not conserved in the plane of the membrane due to interactions with the cytoskeleton and bulk fluid (see section 2.6). The time-time correlation functions shown in Figure 2.4A measure the probability of finding a pixel of the same type at the same location at a later time. Near the critical point with conserved order parameter dynamics, the correlation function decays with a characteristic time

$$\tau \sim \xi^z \tag{2.1}$$

where the correlation length ξ, is $\sim$ 20 nm at $T = 1.05T_c$ and z is 3.75 [64]. This means that even in the absence of coupling to cytoskeleton, fluctuations of 20nm will on average live around 100ms which is a thousand times longer than the time for a single pixel to diffuse through this same distance, and roughly a million times longer than the time for a far from critical membrane to equilibrate. In the absence of cytoskeleton, correlations decay to the uncorrelated value of one at long times (1s, Figure 2.4A).

Time-time correlation functions for simulations conducted in the presence of cytoskeleton (solid (red) and dot-dashed (green) traces in Figure 2. 4B) are qualitatively similar for short times, but approach a value greater than one as $t \to \infty$. This occurs because the locations of cytoskeletal filaments are fixed in time. In a cellular membrane, these correlations will persist until the cytoskeleton rearranges, which we expect to be on the order of seconds to hours [30]. This emergence of a slower time-scale of membrane organization correlated with the
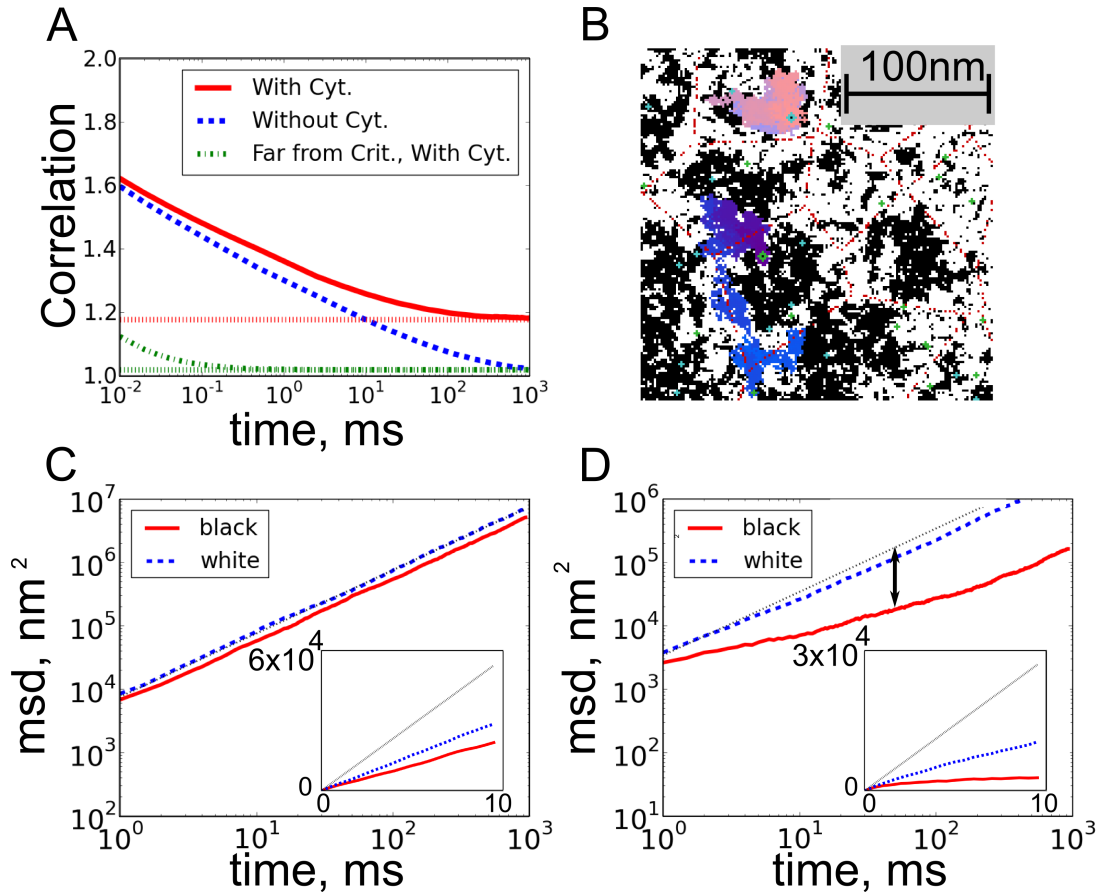
Figure 2.4: Membrane dynamics and component diffusion are sensitive to criticality and connectivity to cortical cytoskeleton.(A). Near the critical point ($T_c = 0.95T$), time-time correlation functions for membranes without coupling decay slowly, and become uncorrelated after roughly 1s (dashed (blue) line). In the presence of coupling to cortical cytoskeleton, fluctuations remain correlated even after long times (higher dotted (red) line at infinite times). By contrast, systems that are far from critical (dash-dotted (green) line, $T_c = 0.5T$) are uncorrelated after a fraction of a millisecond and coupling them to the cytoskeleton makes them decay to a small non-zero value (lower dotted (green) line). (B) Dynamics at Tc=0.95T are also measured by tracking components through simulation time-steps. Tracks for single black (light (pink)) and white (dark (blue)) strongly coupled diffusers are shown (see text). (C-D) Mean squared displacements (MSDs) are calculated from many traces and indicate that (C) weakly coupled black lipids are slightly confined while (D) more strongly coupled black crosses are more strongly confined. Freely diffusing particles have MSDs that are linear in time (dashed line in C and D with slope 1, or linear in inset). We quantify the confinement by the ratio of $D_{100\mu s}$ to D_{50ms}, whose log is the length of the double sided arrow.

location of cortical cytoskeleton is a direct consequence of our model that could be measured experimentally.

2.3.5   Membrane components undergo hop diffusion

In addition to measuring the dynamics of membrane fluctuations, we also track the dynamics of individual components. Different species can partition into the low temperature membrane phases with non-universal partitioning coefficients, which might be stronger or weaker than the partitioning coefficients of our pixels. To explore a range of these, we track two types of objects. We track single pixels which interact with their neighbors with the same energies as the pixels that make up the bulk membrane. A possible example of this type of component might be a lipid present in high abundance in the plasma membrane. We also conduct separate simulations that contain a small fraction of components that couple more strongly to their local membrane environment, effectively forming extended cross structures with twice as many nearest neighbors and three times as many bonds to their local environment. Some examples of components which couple more strongly like this might be large transmembrane proteins which have contact interactions with a large number of nearest neighbors, or minority lipid species with extreme partitioning behavior such as long chain sphingomyelin lipids or polyunsaturated glycerphospholipids. The model that contains strongly coupled diffusing crosses has four components (black and white pixels and black and white crosses) but is expected to still be in the Ising universality class. (Small changes in composition can act to effectively change the two Ising parameters of reduced temperature and magnetization. By adding the same number of up and down strongly couple particles at the critical

32

composition, our system preserves the Ising up-down symmetry and thus only can act as a change in reduced temperature. Because our components couple more strongly they lower the reduced temperature. Representative tracks for strongly coupled diffusers are shown in Figure 2.4B.

Diffusion is quantified by measuring mean squared displacements (MSDs) for a large number (1000) of tracked diffusers. In all cases, we find instantaneous diffusion constants somewhat lower than that imposed by the hop rate ($4\mu m^2$/s). At longer times, MSD curves cross over to a second regime where objects appear to undergo slower effective diffusion, indicating that they are confined. Even in the absence of cytoskeletal coupling diffusers show slightly confined diffusion. Including cytoskeletal coupling leads to significant confinement of weakly coupled black diffusers (Figure 2.4C), and even greater confinement of strongly coupled black diffusers (Figure 2.4D). This occurs even though the cytoskeletal attachment sites have substantial gaps due to the entrainment of the white channels. The resulting black tracer diffusion behavior resembles the hop diffusion reported for some plasma membrane components in living cells [99, 102].

Confinement effects are more pronounced for strongly coupled objects than for weakly coupled objects because there is a higher energy cost associated with having a strongly coupled object in an unfavorable local environment. In contrast, there is a significant probability that a single pixel will diffuse into a region rich in pixels of the other type because the energy cost to having four unlike neighbors is on the order of $k_B T$.

2.3.6 Confinement depends strongly on criticality and weakly on pinning density

Figure 2.4 demonstrates the predictions of our model on the MSDs of diffusers for a specific set of parameters. From this data we can get two diffusion coefficients, one extracted from the value of the MSD at short times ($\sim 100\mu s$), and another from the value at long times ($50ms$) [99, 102]. The ratio of these short- to long-time diffusion constants provides a measure of confinement that depends only weakly on the imposed microscopic diffusion coefficient. In Figure 2. 5 we explore how this measure of confinement for strongly coupled black diffusers is modulated by distance to criticality and pinning density, and how it varies for both black and white objects as a function of composition and pinning density.

Figure 2.5A demonstrates that in the nearly critical region most relevant to biological membranes, sparse pinning sites are able to effectively block strongly coupled black diffusers. In contrast, pickets need to be extremely dense to produce confinement in membranes that are far from criticality in temperature. As diffusion is space-filling in two dimensions, particles easily fit through openings without the long ranged effective force arising from criticality. White objects show little anomalous diffusion, even near the critical point, because they can diffuse along cytoskeletal channels. Near T_c we find values similar to those found in the literature over a wide range of picket densities. We also examine how the diffusion of strongly coupled black and white objects is modulated by changing the total fraction of white and black pixels (Figure 2.5B,C). The surface fraction of phases can be altered in plasma membranes by, for example, cholesterol depletion with methyl-β-cyclodextrin [86]. In simulations, we probe a wide range of compositions by varying the fraction of black and white pixels
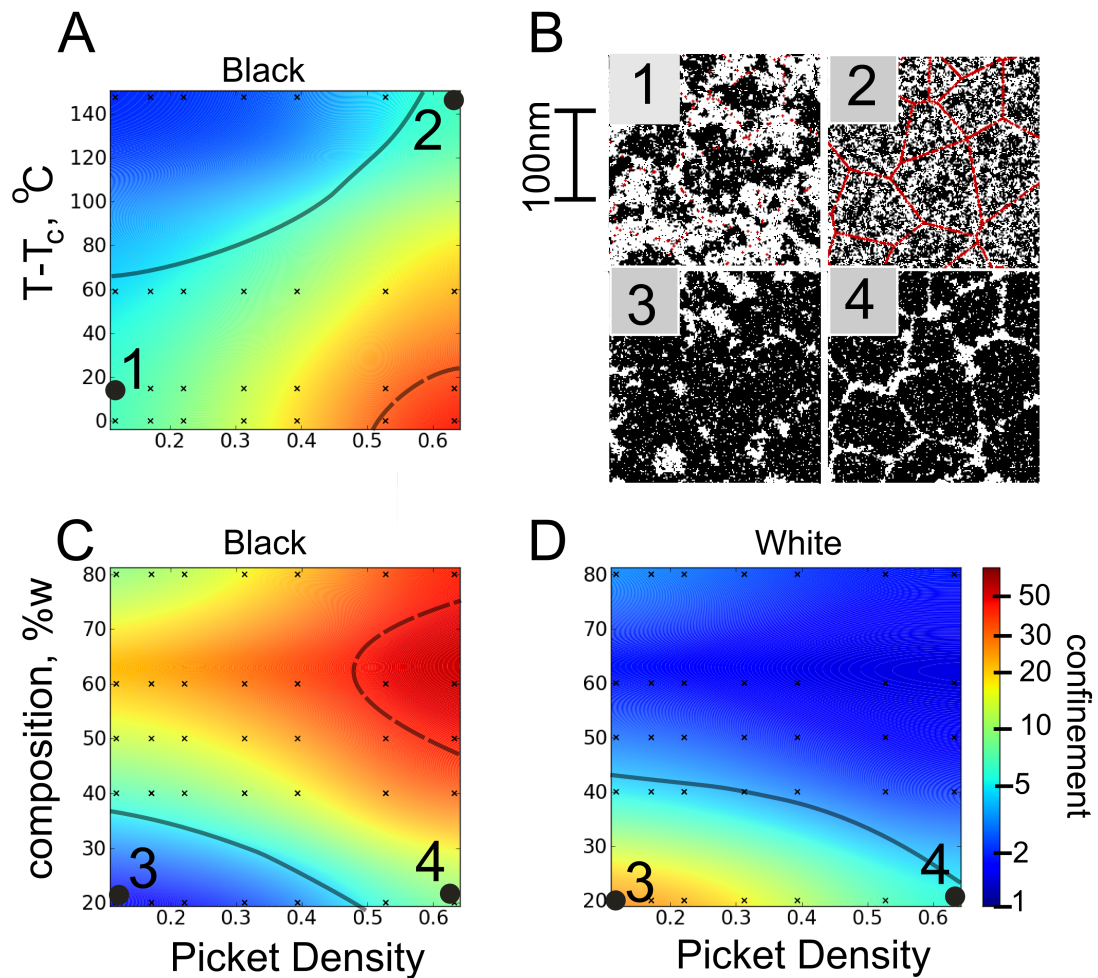
Figure 2.5: Confined diffusion depends upon criticality and the linear density of pinning sites. (A) The ratio of $D_{100\mu s}$ to D_{50ms} obtained from MSD curves like those shown in Figure 2. 4 are used to quantify the confinement of black crosses as a function of temperature and picket density. Near criticality, very weak pinning sites induce a large amount of confinement, whereas far from criticality even dense pinning leads to only slightly confined diffusion. (B) Representative simulation snapshots 1 and 2 have similar levels of confinement and have parameters indicated in part A. (C, D) The ratio of $D_{100\mu s}$ to D_{50ms} is plotted as a function of composition and picket density plot at $37^{o}C$ ($1.05T_{c}$) for both black (C) and white (D) traced crosses. When composition is varied, whichever of the two types is disconnected diffuses with more confinement (part B, images 3 and 4). The surface is a smoothed interpolation of the values from the black data points. Kusumi and coworkers [99, 102] report experimental values between 5 (thick gray line) and 50 (thick dashed line) which is similar to the numbers found here.

at a constant temperature. Changing membrane composition modulates both the continuity of each pixel type and the correlation length of fluctuations (Figure 2.1A). As before, we find that strongly coupled black objects are confined in nearly critical membranes. We more generally find that the confinement of strongly coupled black and white objects is primarily determined by the connectivity of their preferred phase. In the absence of coupling to cytoskeleton, there is a percolation-like transition when there are equal numbers of white and black pixels near T_c [3]. The presence of white pinning sites biases this transition towards larger fractions of black pixels. As a consequence, black objects have confined diffusion over a broad range of membrane compositions and pinning densities, while white objects are significantly confined only at low pinning densities and large fractions of black pixels. The magnitude of confinement arising from steric restrictions to diffusion is not expected to depend significantly on membrane temperature or composition, making this a robust prediction of our model.

2.4   Discussion

In this study, we demonstrate that many reported properties of heterogeneity in cell plasma membranes are reproduced using a simple model that incorporates critical fluctuations and coupling to a fixed cortical cytoskeleton. Critical fluctuations that occur near the liquid-ordered/liquid-disordered miscibility critical point are inherently small, heterogeneous, highly dynamic domains [105]. In

---

[3]On a 2-d hexagonal lattice a line can always be drawn horizontally from the top to the bottom through only black pixels if and only if a line cannot be drawn from the left to right touching only white pixels. Thus, whatever the picket density, there is a percolation-like transition at some composition where the white channels become disconnected and the black puddles become connected.

the absence of membrane-cytoskeleton coupling, the size, composition, and lifetime of fluctuations depends only on the relative proximity to the underlying critical point. In the presence of membrane-actin coupling, these are also governed by the dimensions and movement of the underlying cytoskeletal meshwork. We propose that relatively large (~ 20nm) and long lived (> 10ms) fluid domains as are commonly described in the membrane literature are best understood as fluctuations arising from proximity to criticality. Our model provides a simple explanation for why macroscopic domains are not readily observed in intact cell plasma membranes upon lowering temperature, even though macroscopic phase separation is routinely observed upon lowering temperature in vesicles made from purified lipids [149], cellular lipid extracts [28], isolated plasma membranes [7], and even in whole cells where plasma membranes are dissociated from cortical actin using detergents [118] or detergent-free methods [92]. In our model, macroscopic phase separation is disrupted in intact cell membranes because the size of the underlying cytoskeleton meshwork puts an upper limit on the size of domains that can form in the membrane. At physiological temperatures, in the single phase region above the critical temperature [147], our model yields more functionally relevant predictions. The presence of membrane-actin coupling leads to long lived fluctuations, whose lifetimes are determined by motion of the cytoskeleton. This coupling entrains channels of membrane components that favor cytoskeleton-membrane pinning sites, while compartmentalizing components that are associated with the other membrane state. We predict that liquid-ordered preferring raft proteins and lipids will be compartmentalized within actin-bound corrals if liquid-disordered preferring components tend to associate more closely with cytoskeleton connections. This situation is supported by model membrane studies [91] and most closely re-

sembles the schematic depictions of lipid rafts presented in the literature [128]. Alternatively, we expect to find liquid-disordered preferring non-raft components more confined within actin lined corrals if liquid-ordered preferring components tend to associate more strongly with cytoskeletal connections [66]. We imagine that any given cell could potentially exhibit both behaviors, and that there could be significant variation within single cells and between cell types. The common membrane perturbation of cholesterol depletion should increase the surface fraction of disordered components. We predict that this will lead to increased confinement of order preferring probes and decreased confinement of disorder preferring probes. Our model predicts that disruption of cytoskeleton would significantly alter the localization and dynamics of membrane components, as is frequently observed experimentally [56, 108, 84]. Our model also provides a plausible explanation for the diversity of diffusive behaviors seen for plasma-membrane-bound lipids and proteins. In the hop diffusion model presented in [99, 102], plasma membranes proteins and lipids are confined within actin-lined corrals by physical barriers. We show that by including criticality, confinement can become more robust because entrained channels fill in gaps between neighboring pinning sites. Our model predicts that the confinement of membrane components can depend on their preference for the two membrane phases in addition to their physical size. This could have functional significance; a membrane-bound receptor could significantly alter its localization and mobility upon binding to a ligand if that event modulates its coupling to a particular membrane environment. Such allosteric modulation of a receptors coupling could be a potent regulatory mechanism near criticality, possibly leading to spatial reorganization and functional outcomes. Although it is not directly explored in this study, we also predict that larger membrane-bound ob-

jects will tend to couple more strongly to membrane phases based on the larger size of their interacting surface. Since each protein typically interacts with many lipids, lipid-mediated interactions between proteins can be much stronger and more interesting than a typical lipid-lipid or lipid-protein interaction [51]. It is possible that the stronger coupling of larger objects is responsible for the significant changes observed for diffusing components upon cross-linking [29]. If, in addition, cross-linked proteins or lipids become immobile, then they could stabilize membrane domains that are rich in membrane components that prefer the same phase, as is observed in patching experiments [66], and in cells plated on patterned surfaces [154]. A similar mechanism could contribute to the accumulation of signaling proteins at sites of receptor cross-linking in mast cells or at the immune synapse [65, 62]. While the predictions of our model are in good agreement with many findings in the raft literature, several results are not easily explained in this framework. The tight clustering of components as well as the well-defined stoichiometry of clustering reported in EM [108] and homo-FRET [56] studies is not explained by our model, since interaction energies that are large compared to $k_B T$ are required to maintain this organization. Also, we are not able to reproduce the spot-size dependent diffusive behavior of fluorescently tagged sphingolipids recently reported in living cells using STED microscopy [36]. We could generate similar results if we were to allow for traced particles to experience transient pinning events, which have been observed for a variety of membrane proteins [84, 29]. Our model differs substantively from other explanations of membrane heterogeneity. Unlike micro-emulsion models, we do not require the presence of line-active components that localize on domain boundaries [7]. We expect that the inclusion of line active molecules, either as mobile or pinned components, would modulate critical temperatures

as has been shown previously [161, 157]. In our model, the long-range and dynamic nature of critical fluctuations do not require that additional energy be inserted into the system, as is needed in models that include membrane recycling to disrupt macroscopic phase separation [42]. We expect that recycling of membrane components will be important to describe the behavior at times on the order of membrane turn-over rates (min-hours) [95], which are significantly longer than those explored in this study. Our model also assumes that criticality arises from being close to a miscibility critical point that involves only liquid phases, and not a critical point postulated to be present near a transition to a gel phase [49]. In our model the presence of actin-membrane coupling does not induce phases [37], but instead it tends to gather certain pre-existing membrane fluctuations around points of cytoskeleton contact. Our results do not require a slower diffusion constant in the vicinity of the cytoskeleton [37, 82]. In conclusion, we have presented a minimal model to explain the thermodynamic basis of heterogeneity in living cell membranes. Our model proposes that critical fluctuations, modulated by connectivity to cortical cytoskeleton, are both necessary and sufficient to explain the phenomena associated with 10-100nm fluid domains commonly described in the raft literature. In this new description of lipid rafts, one major role of lipid mediated heterogeneity is to provide effective long range forces between membrane proteins that govern their organization and dynamics. Importantly, the cell could tune effective interactions between proteins by modulating overall membrane composition or by specifically altering the partitioning behavior of individual proteins. In this way, membrane heterogeneity can have direct implications on a wide range of cell functions.

2.5 Acknowledgements

2.6 Supplemental information

Sections 2.7.1-2.7.4 of this supplement serve to give more complete details of the methods used in the simulations. Sections 2.7.5-2.7.8 discuss theoretical details which underlie our choice of model, discussing in more detail its benefits and limitations. In sections 2.7.2 and 2.7.3 we discuss the construction of Figure 2.1. In section 2.7.4 we describe our simulations in sufficient detail that a reader could reproduce figures 2.2-2.5 in the main text. In section 2.7.5 we explain why we may, without significant effect, neglect the tilt of the rectilinear diameter in figure 2.1A of the main text. In section 2.7.6 we give arguments justifying our use of the Ising model to describe cell plasma membranes. In section 2.7.7, we justify our use of model B, Kawasaki dynamics. In section 2.7.8 we discuss how our results depend on the relative viscosities in the two phases.

2.6.1 Calculation of correlation length contours in figure 2.1A

Following Combescot et al. [24] the correlation length as a function of thermo-
dynamic parameters has a simple form in a sort of polar coordinates [117, 122].
A coordinate transformation takes these to the more familiar axes of reduced
temperature and magnetization. We change coordinates a second time by intro-
ducing a non-zero arbitrary tilt, allowing for a non-universal correction which
arises if a change in real temperature in a membrane corresponds to a change
in both reduced temperature and magnetization in the Ising model. In the crit-
ical region this tilt is captured in a single parameter, continuous through the
critical point, called the slope of the rectilinear diameter [164], which is non-
universal and so may be different for different systems in the same universality
class. Though it has not been quantified, in GPMVs it is within experimental
bounds of zero as can be seen in the supplemental videos of [147]. It could the-
oretically be measured by looking at the change in the surface area of bright to
dark regions as temperature is lowered below the critical point. Though experi-
ments cannot differentiate the true tilt from zero, we include a small tilt here of
0.1 to stress that we do not expect it to be exactly zero. The contours all mul-
tiply a non-universal natural length scale which is taken from experiments in
plasma membrane vesicles [147]. Finally, we note that GPMVs in [147] have
a spread in their critical temperatures of around 10^oC, which corresponds to a
spread in their reduced temperatures at 37^oC of about .03. Though it has not
been quantified, we expect there is also some spread in their effective magneti-
zations. Together, we expect that there is some variation from cell to cell both
vertically and horizontally in the exact placement of the red dot corresponding
to physiological conditions. We choose an average value of $T_c = 22^oC$ at criti-
cal composition for this figure and most of the results in the paper. Ignoring a

possible deviation in the magnetization is justified in section 5 below.

2.6.2 Preparation of cell attached plasma membrane vesicles in figure 2.1B

Cell attached plasma membrane vesicles are prepared as described previously [147, 7]. Briefly, RBL-2H3 mast cells are plated sparsely in a MatTek well (MatTek Corp. Ashland, MA) overnight. Cells are then incubated for 1h at 37^oC in the presence of active bleb buffer (2 mM CaCl2 /10 mM Hepes/0.15 M NaCl, 25 mM HCHO, 2 mM DTT, pH 7.4). Cells and attached vesicles are then labeled with DiIC12 (Invitrogen.Eugine, OR) dissolved in methanol for 5min prior to viewing on an inverted microscope (DM-IRB; Leica Microsystems, Bannockburn, IL) at room temperature. The image was taken using an EMCCD camera (iXon 897; Andor, Belfast U.K.). Under these conditions, attached blebs contain coexisting liquid-disordered (bright) and liquid-ordered (dark) phases.

2.6.3 Simulation details, acceptance criterion and equilibration procedures

All simulations were run on a 400x400 bi-periodic square lattice with spin variables living on the squares ($S_i = \pm1$, white and black pixels respectively). In all cases the standard Ising Hamiltonian is used, $H = \sum_{\{i,j\}} s_i s_j$, with summation over the four nearest neighbors. We use a conversion factor from lattice constant to real distance of 1nm. Temperatures are converted to Kelvin (and by ex-

tension Celsius) by equating the exact critical temperature given by the Onsager solution on the square lattice, $T_c = \frac{2}{\log(1+\sqrt{2})}$, with the experimentally measured $T_c = 295K$ so that $T_{sim} = .00769 T_{real}/K$. In a Monte-Carlo sweep $160,000$ (400^2) pairs of pixels are proposed (on average each pixel is proposed to exchange twice). We use Metropolis spin exchanges; each pair is exchanged or not so as to satisfy detailed balanceCYTSNewman1999. If the resulting configuration is lower in energy, the exchange is always accepted. If the energy is raised, the exchange is accepted stochastically with probability where ? is the inverse temperature and ?H is the change in energy between initial and final states. Sites occupied by pickets are taken to have an infinite field so that exchanges which propose to move a black pixel onto a picket are always rejected. Where appropriate, strongly coupled tracers have an infinite coupling to other like pixels, so that any move which ends with such a strongly coupled tracer touching an unlike pixel is always rejected. This effectively converts them into cross shaped objects (though with overlap allowed), with three times as many bonds to their local environment and twice as many neighbors.

Two types of dynamics are employed (any dynamics which satisfy detailed balance will lead to the same equilibrium ensemble of configurations). When rapid equilibration is desired we employ nonlocal moves where each of a pairs of spins are randomly chosen from all sites on the lattice. To simulate real time we use Kawasaki dynamics where we randomly choose a spin, and then randomly choose one of its four nearest neighbors to exchange with.

Equilibration is very rapid using the nonlocal dynamics, where z is near 2. We always equilibrate for $100,000$ sweeps using nonlocal moves starting from a distribution which observes the random field constraint but which is other-

wise random. $100,000$ sweeps is many times longer than the decay time of the slowest decaying system used here (the decay time is around 1000sweeps for the pinning density in figures 2.2-2.4 at $1.05Tc$ as can be seen by eye looking at snapshots at subsequent times, or quantitatively as the decay time of time-time correlations). For simulations with strong tracers we first equilibrate without tracers. We then add them randomly, run an additional $100,000$ iterations to equilibrate, and then start our dynamic simulations.

In figure 2.2 no dynamics are required as only a snapshot is given. In figure 2.3, the time averaged spatial correlation figures are averaged from 1000 snapshots each separated by 1000 sweeps of the non-local dynamics. The auto-correlation functions in figure 2.3 are produced in the standard way. We first Fourier transform the spin configuration. We then square this to get the static structure factor $S(k)$. We then perform an inverse Fourier transform on $S(k)$ and radially average the result to get $g(r)$ in a normalization which goes to 0 at infinity. To convert to the normalization used here,

$$G_(r) = \frac{\langle P_{+1}(R)P_{+1}(R+r)\rangle}{\langle P_{+1}(R)\rangle^2} \tag{2.2}$$

(where R is averaged over the entire lattice and where $P_{+1}(x)$ is the probability of an up spin at position x) we add one to these (since all of our correlation functions are plotted at m=0). We assume that the lattice sits on an infinite periodic plane so that values at infinity take the mean value of the system.

To produce the cross-correlation curves we follow the same procedure except that we replace the square of the Fourier transform with the real part of the product of the Fourier transform of the pixel configuration and the Fourier

transform of the random field configuration. This leads to

$$Gcyt(r) = \frac{\left\langle P_{cyt}(R)P_{+1}(R+r) \right\rangle}{\left\langle P_{+1}(R) \right\rangle \left\langle P_{cyt}(R) \right\rangle} \tag{2.3}$$

where $P_{cyt}(x)$ is the probability of finding a cytoskeletal pixel at position x.

For time-time correlations shown in Figure 2.4a we take the dot product of every pixel in the simulations value (±1) at time t with itself at a later time $t + \Delta t$. We average this over all pixels and all times $t < t_{max} - \Delta t$, with $t_m ax = 5,000,000$ sweeps and add one to the value for consistency with our normalization (in supplemental figure 2.6 two different realizations of this procedure are shown to give the reader an idea of the expected error). To produce the dashed lines which correspond to the asymptotic values of the correlation functions in the presence of the random field we take the average value of the square of the mean field pixel values from the configuration calculated from the non-local dynamics (which are identical and faster to equilibrate, displayed in Figure 2.3A,C) and add one to this value.

To convert from Monte-Carlo time to real time, we use a microscopic diffusion constant of $1\mu m^2/s$ which is in the middle of the range cited for membrane bound lipids and proteins (though this range spans some 2 orders of magnitude) [36, 89, 43]. In a Monte-Carlo sweep, each pixel is proposed to swap twice on average. If all swaps were accepted this would lead to a mean squared displacement $< x^2 > = 2d^2$/sweep where d is the lattice spacing. With our value of $d = 1nm$, we find that if we associate one sweep with $.5\mu s$ we arrive at the desired $D = 1\mu m^2/s$ in the formula for diffusion $< x2 > = 4Dt$. As some moves are rejected, the effective diffusion constant even at arbitrarily short times is actually somewhat lower than this for traced diffusing pixels and slower still for our more strongly coupled diffusers.
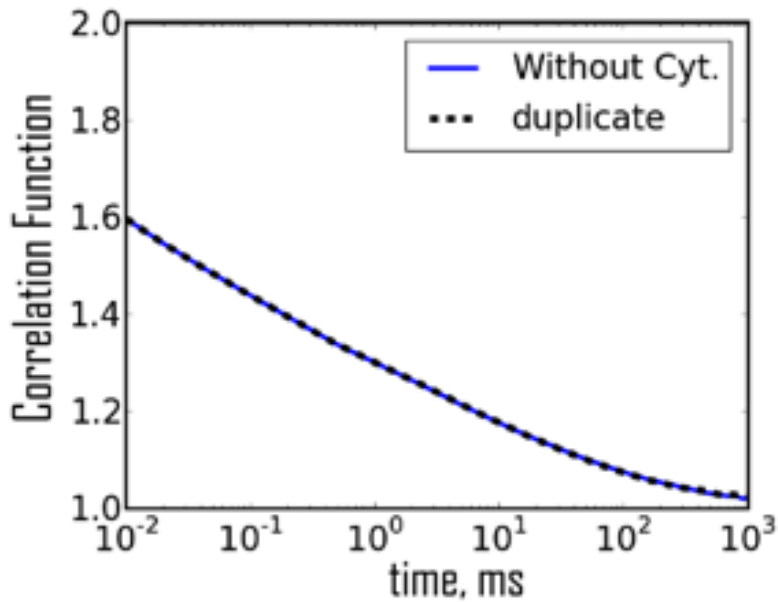
Figure 2.6: To demonstrate the accuracy of our time-time correlation functions, we reproduce the slowest decaying curve from the figure 2.4A and plot both versions on the same graph. A slight deviation is visible at very late times.

To calculate mean squared displacements we trace 1000 particles which diffuse on an infinite plane whose configuration is periodic with period 400. Whenever a particle moves through a boundary in the $\pm x$ direction (for example), its new position for the purpose of mean squared displacement calculation is changed by ± 400. This allows us to keep track of tracers which may diffuse off of the edge of the periodic simulation. We average the mean squared displacements over all traced particles.

To produce the contour plots in Figure 2.5 we extrapolate and smooth between the points where simulations are conducted by replacing each points value by an average over all simulated points weighted by $\exp(-d^2/d_o^2)$ where $d_0 = .1$ in temperature, pinning density and magnetization.

47

2.6.4 Irrelevance of a tilted rectilinear diameter to lowest order

As discussed in Calculation of correlation length contours a change in real temperature near a critical point changes both of the corresponding Ising variables of reduced temperature and magnetization. Here we show that such a tilt introduces a subdominant correction to the critical properties. In particular it does not affect the singular behavior of the correlation length

In the scaling regime, a temperature change corresponds to a change in the reduced temperature by an amount Δt and a change in the magnetization by an amount $\Delta m = a\Delta t$ where a is the tilt of the rectilinear diameterCYTSZollweg1972. We here consider a model in the scaling regime whose correlation length is given by

$$\xi(t, m) = t^{-\nu}\mathcal{F}(m^{\nu/\beta}/t) \tag{2.4}$$

where $\mathcal{F}$ is a universal function. We note that $\mathcal{F}$ is not singular at zero, since along the axis the correct scaling is given by

$$\xi(t, 0) \sim t^{-\nu} \tag{2.5}$$

We now set $m = at$ which corresponds to a membrane with critical composition taken to a temperature $T = (1 + t)T_c$. This gives:

$$\xi(t, at) = t^{-\nu}\mathcal{F}(a^{\nu/\beta}t^{\nu/\beta-1}) \tag{2.6}$$

Because $\nu/\beta = 8 > 1$, the argument of $\mathcal{F}$ is not singular near $t = 0$. As F itself

is not singular there, the scaling of the correlation length at critical composition has singular behavior which is independent of the tilt of the rectilinear diameter. (In addition to the "analytic correction to scaling" represented by the tilting of the rectilinear diameter proportional to, there is also a singular correction to scaling proportional to . Since $\alpha = 0$ for the 2D Ising model, our argument above applies without modification; this correction too is subdominant. See [122, 55, 151] for a more complete picture of subtleties involved.) This means that the critical properties of an Ising system at critical composition but slightly away from the critical temperature are dominated by its effective reduced temperature, with its effective magnetization coming in only at a higher order in the distance from the critical point. This calculation quantifies what can be seen in Figure 2.1A of the paper; Near the critical point the contours are broad and flat showing a larger dependence on the vertical reduced temperature direction than on the horizontal magnetization direction.

2.6.5   Possible universality classes

Here we give arguments to support our use of the 2-D Ising universality class to model the critical point seen in GPMVs [147]. We explain the theoretical motivation for expecting Ising criticality, discuss experimental evidence for it and argue that two other possible universality classes are unlikely to describe cellular membranes.

The Ising Universality class is expected for any system with a scalar order parameter, a single number which describes the system at larger length scales. In three dimensions, the Ising model has been shown to quantitatively describe

an enormous array of liquid-gas and liquid-liquid critical points [122] mostly involving small molecules, but also including more exotic liquid phases containing polymer blends [119]. In two dimensions there are fewer examples, but the critical phenomenon seen in three component model membranes near fluid-fluid critical points are in this class [68]. In each of these two and three dimensional examples the components (or densities) of the two low temperature phases acts as the order parameter, which is therefore a scalar. Plasma membrane vesicles are certainly more complicated than the simple systems described above at the microscopic level, but as they phase separate into two domains with different compositions below Tc, the composition difference between these phases remains a good scalar order parameter. As such, the theoretical expectation is that they should also be described by 2-D Ising Universality, which is in agreement with [147].

We cannot exhaustively dismiss other possible universality classes at present, though several cases can be ruled out. The q-state Potts universality class generalizes the Ising model ($q = 2$) to the critical point of a system which separates into q distinct liquids below Tc [27]. For $q = 3$ and 4 there are $2 - D$ critical points, while for q larger, there are only abrupt, first order transitions. These models are ruled out quite simply by the GPMV experiments. The q-state Potts model predicts that below Tc a Potts critical membrane should phase separate into q domains of approximately equal area. To our knowledge no more than two coexisting macroscopic liquid phases have been observed in any membrane system. We note as an aside that Potts models with q¿2 would be dramatically harder for a cell to tune towards. The Ising critical point contains two parameters which must be tuned. At fixed temperature we must tune the ratio of the two phases below Tc and their interaction energies. The 3-state Potts

model contains five parameters that need tuning [27]. We can think of these as two area ratios (A:B and B:C) as well as three interaction energies (A with B, B with C and A with C).

Another possibility is that the membrane might display tri-critical Ising behavior. This occurs as an Ising model is tuned (along a third dimension in parameter space) to a boundary beyond which it becomes an abrupt first order transition. This model would only require tuning one additional parameter making it at first pass more appealing. However, it predicts a value for the critical exponent of $\nu = 5/9$ [27], in contrast to $\nu = 1$ for the Ising model, which is not consistent with existing experimental data [147].

Although we are not able to conclusively demonstrate that the universality class is Ising at this time, we emphasize that our results should hold even if the universality class turns out to be more exotic. The qualitative features of our findings come about due to features which have been conclusively demonstrated in GPMV experiments [147]: A correlation length which becomes large near the critical point, and dynamics which become slow near the critical point. Although it is outside of the scope of this work, we also note that there has been significant theoretical progress towards a complete categorization of possible universality classes permissible in 2-D [27]. Though there are infinitely many, they are all indexed by a unique number between zero and one, the central charge (which is 0.5 for the Ising model). It would be an interesting project to see which if any others might be consistent with membrane experiments.

2.6.6 Dynamic universality and motivation for model B

The Ising universality class defines the coarse grained static correlation functions of our system. However, different systems in the same universality class can display different dynamics even in the scaling regime. These in turn fall into different dynamic scaling universality classes [64] which are determined by which quantities are conserved by the dynamics. In our case, we argue that the order parameter (or composition) is locally conserved, while momentum is not, as the fixed cytoskeleton breaks translational invariance, and may exchange momentum with the membrane. In synthetic membranes, hydrodynamics is certainly important[4]. With the order parameter conserved and momentum not, we expect model B [64]. The Kawasaki dynamics we implement here are also in this class [156].

Membranes are expected to have a conserved order parameter for the times relevant to this study. The two low temperature phases contain different concentrations of various components. For a regions order parameter to change, components must physically move into it from a neighboring region. Although components are found with some probability in each low temperature phase (and are able to move between them), this is not qualitatively different from the Ising model where white pixels and even white pixel clusters are found in the low temperature black pixel phase. At longer times we expect processes like trafficking of lipids to change the order parameter [42].

We also expect that in intact cell plasma membranes momentum will not be conserved at relevant lengths, leading to model B (rather than model H, which arises when momentum is also conserved). There is an emerging theoretical

---

[4]See chapter 4 for a more sophisticated treatment of dynamics

picture for the expected dynamics of model membranes near an Ising critical point, immersed in water. In two dimensions the usual Stokes-Einstein relations which predict the microscopic diffusion constant as a function of the diffusers size and the viscosity of the surrounding fluid cannot be easily applied [115] essentially because energy is not locally dissipated. For large inclusions this means that even an arbitrarily small viscosity of the surrounding fluid enters into the microscopic diffusion rate. It also means that this diffusion constant depends only logarithmically on the size of the diffuser, crossing over to a rate determined by the 3-D viscosity (which scales as $1/r$) for large enough r [23]. For lipids in a bilayer membrane, the picture is somewhat simpler. Such lipids show an enormous temperature dependence in their microscopic diffusion rates [43] consistent with an energy barrier of 20-30 KBT. These rates are approximately two orders of magnitude faster than the rates predicted by the hydrodynamic diffusion constant extrapolated from the movement of micron sized diffusers [23] in similar liquid environments. This suggests the following picture [142]: rather than their motion being dominated by hydrodynamic flow, lipids sit in deep potential wells in the membrane. Their microscopic diffusion rate is set by the likelihood of thermally hopping into the next potential well model B, rather than model H, governs the particle diffusion rate. Thus membranes are similar to liquids above the glass transition, where self-diffusion (mediated by swapping particles) is much faster than bulk diffusion. (In a crystal, the latter would be zero.)

Even though particle diffusion is dominated by model B, we must address also the evolution of the order parameter field. Hydrodynamic flows are more effective at stirring the order parameter field than particle exchanges. This is reflected in the dynamical critical exponent z, which is 3.75 for model B and

around 2 for model H in two dimensions [60, 64]. Roughly, correlation times at a length-scale L scale as $(L/L_0)^z$ (critical slowing-down). Since at the lipid length scale of one nm the time scales for hopping and hydrodynamic rates differ by two orders of magnitude, this suggests that the hydrodynamic effects will become competitive with the model B dynamics at roughly 10nm (where $D_{lipid}(L/L_0)^3.75 \sim D_{hydro}(L/L_0)^2$), which is roughly the equilibrium correlation length where both power laws stop applying. In the absence of a cytoskeleton and at the critical temperature, the hydrodynamic diffusion will dominate in a range of lengths between this crossover and a crossover to a modified three-dimensional model H dynamics (when the low viscosity of the surrounding water becomes relevant, at around 1000nm) [60]. The rigid cytoskeleton will act as a fixed boundary condition at a significantly shorter length scale in our model, suppressing hydrodynamic flows entirely while permeable to hopping diffusion. (The cytoskeleton should be particularly effective at suppressing the logarithmic correlations in the 2D hydrodynamics.) Hence our model B dynamics not only dominates the diffusion of small particles, it also should dominate the dynamics of the order parameter field except for small corrections in a range intermediate between the correlation length and the cytoskeleton confinement scale. We finally note that coupling to a cytoplasm with many rigid objects nearby may lead to even more suppression of bulk flow in the membrane as discussed in [141].

2.6.7 Effects of different viscosities in the two liquid environments

The l0 and ld phases represented by our white and black pixels have viscosities which differ by a factor of around 4 though in some cases up to a factor of 10 [89, 77, 43]. A similar range is expected in the diffusion constant difference seen between lipids in the two phases. In most of the manuscript we ignore the consequences of this, but we discuss its implications here. The dynamics of the order parameter are relatively unaffected by this as order parameter changes always take place at the interface and so have a single rate which is presumably somewhere in between the rates predicted by the individual viscosities.

Traced particle diffusion, however, can be affected by this viscosity difference. We consider the case relevant to our dynamics; a particle which mostly resides in one of the two phases, but which may need to cross through the other phase to diffuse long distances. The microscopic diffusion constant will be an average of the diffusion constants in the two phases weighted by the time spent in each phase. For us it will be given primarily by the diffusion constant in the phase in which it usually resides.

To travel large distances these particles potentially needs to hop over barriers of the alternative phase, which leads to the confinement seen in our simulations. We separate this process into an attempt rate at crossing and a success probability. The total amount of time spent in the unfavorable region, as well as the success probability are determined by static energetic considerations; they does not depend on the relative viscosities. The attempt rate, however, must depend on the ratio of the diffusion constants in the two liquids. In particular,

to satisfy detailed balance it must go as the ratio of the viscosity in the usual fluid environment to that in the barrier environment. As such, particles which mostly live in the low viscosity environment make fewer attempts at crossing the barrier, while those which live mostly in the higher viscosity environment make more. This can lead to some additional confinement for particles which live in the lower viscosity phase. The extra confinement is bounded by the ratio of the two viscosities.
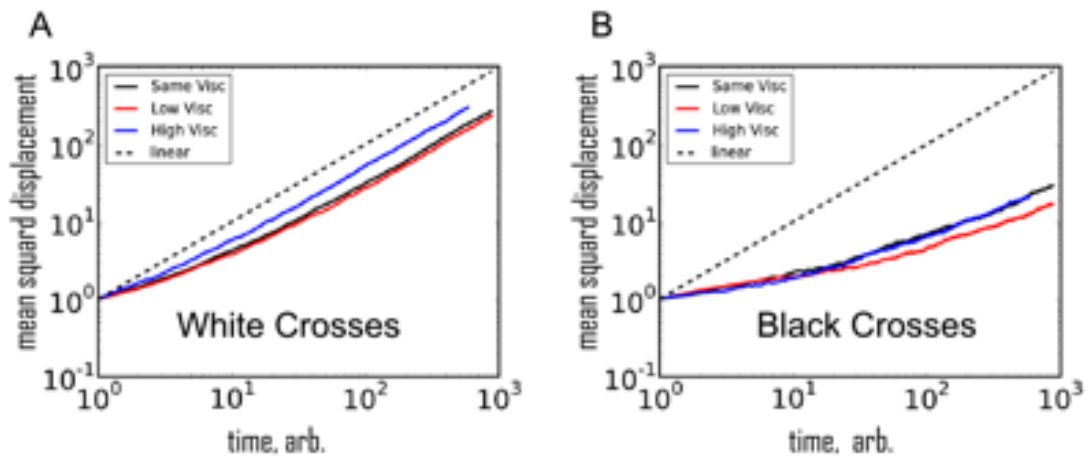
Figure 2.7: The mean squared displacement of strongly coupled white (A) and black (B) diffusers at $1.05T_c$, with the same static properties as in Figure 2.4 D of the main text. In each figure the black line shows the mean square displacement for the case when both viscosities are equal. In the other cases the diffuser is a component of the high (blue) or low (red) viscosity liquid. The y-axis is normalized to 1 at a time such that the traced particle has performed on average 2000 attempted exchanges. The x-axis is normalized so that in each case the displayed traced particles are proposed to swap approximately 2000 times (0.5 ms in the main text) so that all have an identical microscopic attempt rate. As can be seen, particles that normally inhabit the low viscosity liquid see some degree of extra confinement, and vice versa.

To demonstrate these theoretical predictions we run simulations where the diffusion rates in the two liquid environments are different by a factor of four, mimicking a factor of four change in the viscosity. We implement this by trading

like particles in the lower viscosity liquid with a rate four times that with which unlike particles and particles in the high viscosity liquid are traded. We run simulations where either the white pixels or the black ones have a higher viscosity. We then plot MSDs vs time (figure 2.7), for the cases where both liquids are equivalent, and where the given particle is either a component of the lower or higher viscosity liquid. In each case the y-axis is normalized to 1 at t=1ms (in the equal viscosity case), and we compress the x-axis for the high viscosity case so that the frequency of moves per unit time on the x-axis is the same. We also plot a dashed line corresponding to a lack of any confinement. We note that in our simulations this consequences of this effect are fairly small.

CHAPTER 3

CRITICAL CASIMIR FORCES IN CELLULAR MEMBRANES

Abstract [1]-Recent experiments suggest that membranes of living cells are tuned close to a miscibility critical point in the 2D Ising universality class. We propose that one role for this proximity to criticality in live cells is to provide a conduit for relatively long-ranged critical Casimir forces. Using techniques from conformal field theory we calculate potentials of mean force between membrane bound inclusions mediated by their local interactions with the composition order parameter. We verify these calculations using Monte-Carlo where we also compare critical and off-critical results. Our findings suggest that membrane bound proteins experience weak yet long range forces mediated by critical composition fluctuations in the plasma membranes of living cells.

3.1   Introduction

Cellular membranes are two-dimensional (2D) liquids composed of thousands of different lipids and membrane bound proteins. Though once thought of as uniform solvents for embedded proteins, a wide array of biochemical and bio-physical evidence suggests that cellular membranes are quite heterogeneous (reviewed in [105, 90]). Putative membrane structures, often termed 'rafts', are thought to range in size from $10 - 100$nm, much larger than the $a \sim 1$nm size of the individual lipids and proteins of which they are composed. This discrepancy in scale presents a thermodynamic puzzle: naïve estimates predict

---

[1]This chapter will appear in *Physical Review Letters* with coauthors Sarah L. Veatch and James P. Sethna.

enormous energetic costs associated with maintaining heterogeneity in a fluid membrane [93].

Parallel work in giant plasma membrane vesicles (GPMVs) isolated from living mammalian cells presents a compelling explanation for the physical basis of these proposed structures. When cooled below a transition temperature around 25°C, GPMVs phase separate into two 2D liquid phases [7] which can be observed by conventional fluorescence microscopy. Quite surprisingly, they pass very near to a critical point in the Ising universality class at the transition temperature [147]. Near a miscibility critical point, the small free energy differences between clustered and unclustered states could allow the cell to more easily control the spatial organization of the membrane, lending energetic plausibility to the proposed structures. Although analogous critical points can be found in synthetic membranes [150, 150, 69] these systems require the careful experimental tuning of two thermodynamic parameters, as in the Ising liquid-gas transition where pressure (equivalent to the Ising magnetization) and temperature must both be tuned. Although it has been suggested that biological systems frequently tune themselves towards *dynamical* and other statistical critical points [98], so far as we know membranes are the clearest example of a biological system which appears to be tuned to the proximity of a *thermal* critical point.

Other plausible theoretical models have focused on 2D micro emulsions (stabilized by surfactants [13], coupling to membrane curvature [116], or topological defects in orientational order [81]) but none have emerged from direct, quantitative experiments on membranes from living cells. It has been argued that Ising fluctuations should have vanishing contrast between the two phases [116].

While this is true of macroscopic regions, a region of radius R of lipids of size $a \sim 1nm$ should have contrast $\sim (R/a)^{-\beta/\nu} = (R/a)^{-1/8}$, leading to predicted composition differences of 0.7 at the physiologically relevant $20nm$ scale, and differences of 0.5 at $R = 400nm$ scale of fluorescence imaging [147]; on the length scales of interest there is plenty of contrast. Indeed, our calculations of Ising-induced forces take place at and above the critical point, where the macroscopic contrast is of course zero.

How might a cell benefit by tuning its membrane near to criticality? Presuming that functional outcomes are carried out by proteins embedded in the membrane, we focus on the effects that criticality might have on them. For embedded proteins, proximity to a critical point is distinguished by the presence of large, fluctuating entropic forces known as critical Casimir forces. Three dimensional critical Casimir forces have a rich history of theoretical study[45]. In more recent experimental work [12] colloidal particles clustered and precipitated out of suspension when the surrounding medium is brought to the vicinity of the liquid-liquid miscibility critical point in their surrounding medium. Two dimensional Casimir forces like the ones studied here have been investigated for the Ising model using numerical transfer matrix techniques [15], for a demixing transition using Monte-Carlo [110] and for shape fluctuation using perturbative analytical methods [158, 159]. Here we estimate the magnitude of composition mediated Casimir forces arising from proximity to a critical point, both in Monte-Carlo simulations on a lattice Ising model, and analytically, making use of recent developments in boundary conformal field theory(CFT) [18, 52, 27]. Our motivation is biological: in a cellular membrane, these long ranged critical Casimir forces could have profound implications. More familiar electrostatic interactions are screened over around 1nm in the cellular environment, whereas

we find the composition mediated potential can be large over tens of nanometers.

Critical Casimir forces are likely utilized by cells in the early steps of signal transduction where lipid mediated lateral heterogeneity has been shown to play vital roles. Many membrane bound proteins segregate into one of two membrane phases when biochemically extracted with detergents at low temperatures [96], or when proteins are localized in phase separated GPMVs [147]. Furthermore, there is evidence that some receptors change their partitioning behavior in response to ligand binding or down-stream signaling events [65]. Modeling this as a change in the coupling between the receptor protein and the Ising order parameter predicts that these bound receptors will see a change in their interaction partners. Supporting this view, ligand binding to receptor is often accompanied by spatial reorganization in which receptors and downstream molecules move into close proximity of one another [105, 144], perhaps because they now share a preference for the same Ising phase. Perturbations to the lipid composition of the membrane, like cholesterol depletion [86], typically disrupt this spatial reorganization [144] and have dramatic effects on the final outcomes of signaling [125, 127, 50], in our view by taking the membrane away from its critical point and interfering with the resulting long ranged forces.

3.2   Point-like approximation

We take three approaches to estimating the form of these potentials. We first consider two point-like proteins which interact with the local order parameter like local insertions of magnetic field h_1 and h_2 at $x = 0$ and $x = d$. To calcu-

late the resulting potential we write a Hamiltonian for the combined system of the Ising model with order parameter $\phi(x)$ plus proteins as $H([\phi(x)], d) = H_{Ising}([\phi(x)]) + h_1\phi(0) + h_2\phi(d)$. We then write a partition function for the combined system $Z(d) = \int D[\phi(x)] e^{-\beta H((\phi(x), d))}$ and solve to lowest order in h giving the potential $U_{eff}(d) = -\log(Z(d)) + \log(Z(\infty)) = -h_1 h_2 C(d)$ with $C(d) = \langle\phi(0)\phi(d)\rangle$ the correlation function. $C(d) \sim d^{-\eta}$ when $d \ll \xi$ with the Ising model $\eta = \frac{1}{4}$ and $C(d) \sim d^{-1/2}\exp(-d/\xi)$ for $d \gg \xi$. The potential is attractive for like and repulsive for unlike insertions of field, in agreement with the scaling of the CFT result as we will show below. A protein which does not couple to the order parameter can still feel a long-ranged force if it couples to the local energy density. The energy density is also correlated with a d^{-2} dependance. However, the magnitude of both of these potentials, as well as their shape at distances $d \sim r$ require the Monte-Carlo and CFT approaches described below.

3.3   The Bennet method on the lattice Ising model

Secondly, we numerically calculated potentials using Monte-Carlo on the lattice Ising model for like and unlike disk-shaped inclusions. Although absolute free energies are difficult to obtain from Monte-Carlo techniques, differences between the free energies of two ensembles, δF, conditioned on a subset of the degrees of freedom are readily available, provided the degrees of freedom in the two 'macro-states' can be mapped onto each other and have substantial overlap. This information is implicitly used in a Monte-Carlo scheme where both 'macro-states' are treated as members of a larger ensemble and are switched between so as to satisfy detailed balance. The Bennett method [8, 75], uses this information more explicitly, noting that $\exp(-\beta\delta F) = \langle e^{-\beta\delta E}\rangle$ can be estimated without bias

from either distribution.

Our 'macro-states' are the location of two blocky 'disks' as shown in fig 3.1C. All spins either contained in or sharing a bond with these disks are constrained to be either all up or all down. We map the degrees of freedom in one macro-state to a neighboring one by moving all of the spin values 1 lattice spacing to the right or left of the fixed spin region onto fixed spins on the other side. By integrating our measured $\beta\delta F = -\log\langle exp(-\beta\delta E)\rangle$ over many sites outwards to infinity, we can in principle measure this potential to arbitrary distance. However, because the potential is long-ranged at T_c, we integrate it out to 50 lattice spacings and add the CFT prediction for the potential at that distance as described below. We perform simulations using the Wolff Algorithm on 500×500 lattices under the constraint that any cluster which intersects a disk is rejected, enforcing our fixed boundary conditions. We supplement these with individual spin flips near the inclusions where almost all Wolff moves are rejected. The resulting potentials are plotted in fig. 3.1A. We collapse the Monte-Carlo curves by using the the effective radius given by the farthest point from the origin contained in the blocky lattice inclusion as the effective radius.

3.4   Conformal field theory approach at T_c

Finally, we use conformal field theory to make an analytical prediction for the form of these potentials. Our calculation makes extensive use of the conformal invariance of the free energy which emerges at the critical point. An element from the global conformal group can take us from the configuration in fig. 3.2A to that shown in fig. 3.2B where the two disks are concentric with spatial infinity
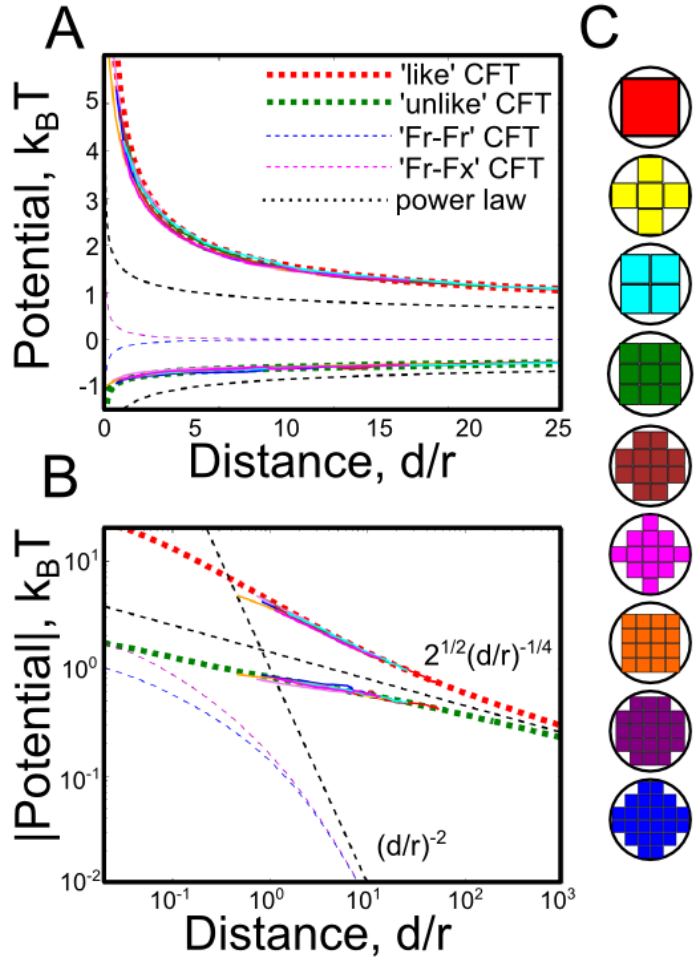
Figure 3.1: Effective potentials between bound inclusions are plotted on linear (top) and log-log (bottom) graphs, for inclusions where $r_1 = r_2 = r$. The CFT results for both like and unlike interactions (thick dashed lines) and for potentials containing a free BC agree with the power-law scaling of the two-point function (thin black dashed line) at large lengths, but separate at small separations. We also compare to Bennett method simulations at T_c as described in the text. We run simulations for each of the blocky spheres shown in (C). Each curve is plotted collapsed by using r as the distance to the farthest point from its center, with no free parameters. The results of our Monte-Carlo pair potentials are all shown plotted against d/r (thin solid lines with colors as in (C)) with the theory curves in dashed lines. The CFT prediction is in excellent agreement with simulation data even for very small inclusions well past the applicability of the power law prediction of the perturbative approach. The value of the potential is fit at the farthest accessible simulation point, where we add the CFT prediction.

in fig. 3.2A now lying between the two cylinders on the real axis. The radius of the outer circle $R(d, r_1, r_2)$ is now given by:

$$R(d, r_1, r_2) = \frac{x - 2 + \sqrt{(x-2)^2 - 4}}{2}, \quad x = \frac{(d + 2r_1)(d + 2r_2)}{r_1 r_2} \tag{3.1}$$

The much larger local conformal group, particular to 2D, is the set of all analytic functions. We use the transformation $z' = \frac{\log(z)}{2\pi}$ gluing together the boundaries at $x = 1$ and $x = 0$ to give the cylinder shown in fig. 3.2C with a circumference of 1 and length:

$$\tau(d, r_1, r_2) = i \log(R(d, r_1, r_2))/2\pi \tag{3.2}$$

This transformation breaks global conformal invariance and so increases the free energy by $c \log(R)/12$ [52], where $c = 1/2$ in the Ising model. Defining a $1 + 1$ dimensional quantum theory on the cylinder (see [52]) with 'time', t running down its length, our Hamiltonian for t translation is $H = 2\pi(L_0 + \bar{L}_0 - \frac{c}{12})$, where $L_0 + \bar{L}_0$ is the generator of dilation in the plane.

Partition functions in this geometry are linear sums of characters of the conformal group. The representations of the conformal group particular to the Ising universality class have characters given by [52, 19]:

$$\chi_0(\tau) = \frac{1 + q^2 + q^3 + \cdots}{q^{1/48}} = \frac{1}{2\sqrt{\eta(\tau)}} \left[\sqrt{\theta_3(q)} + \sqrt{\theta_4(q)} \right]$$

$$\chi_{1/16}(\tau) = \frac{1 + q + q^2 + 2q^3 + \cdots}{q^{1/48 - 1/16}} = \frac{1}{\sqrt{2\eta(\tau)}} \left[\sqrt{\theta_2(q)} \right] \tag{3.3}$$

$$\chi_{1/2}(\tau) = \frac{1 + q + q^2 + \cdots}{q^{1/48 - 1/2}} = \frac{1}{2\sqrt{\eta(\tau)}} \left[\sqrt{\theta_3(q)} - \sqrt{\theta_4(q)} \right]$$

where $q = \exp(i\pi\tau)$, with $\eta(\tau)$ the Dedekind η function and with $\theta(\tau)$ the Jacobi, or elliptic Theta functions.

Conformally invariant boundary conditions (BCs) can be deduced by demanding consistency between two parameterizations of the cylinder [19]. In
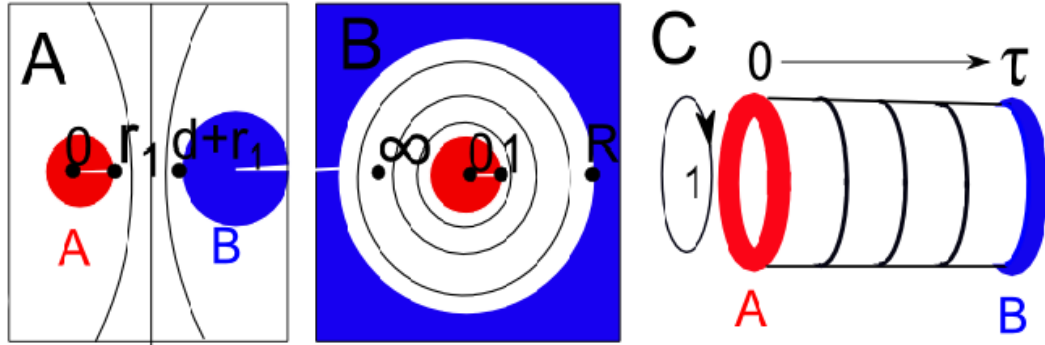
Figure 3.2: We consider potentials of mean force in configuration (A), with disks of radius r_1 and r_2 separated by a distance d with boundary conditions A and B. We conformally map this to configuration (B), where both disks are centered on the origin, with the first at radius 1 and the second at radius $R(d, r_1, r_2)$. We then map this to a cylinder shown in (C) of circumference 1 and length $-i\tau = \log(R)/2\pi$ where we associate restricted partition functions in an imaginary time $1 + 1$D quantum model with potentials of mean force in the original configuration.

one, time moves from one BC to the other across the cylinder with the usual Ising Hamiltonian. Alternatively, time can move around the cylinder with the BCs now entering into the Hamiltonian. There are three allowed BCs [19] which, by considering symmetry can be associated with 'up', 'down' and 'free'. These three BCs have four non-trivial potentials between them; a repulsive 'unlike' interaction between 'up' and 'down' BCs, an attractive 'like' interaction between 'ups' and 'ups' or 'downs' and 'downs', an attractive 'free-free' (Fr-Fr) interaction between two 'free' BCs and a repulsive 'free-fixed' (Fr-Fx) interaction between a 'free' BC and either an 'up' or a 'down'.

The free energy in the configuration shown in figure 3.2A can be interpreted as a potential of mean force between the bound inclusions. Choosing the convention that the potentials go to 0 as $d \rightarrow \infty$, the potential is given by $U(d) = F_{AB}(\tau) - F_{AB}(\infty)$. After undoing the mapping which changes the free en-

66

ergy by a central charge dependent factor so that $F_{AB}(\tau) = -\log Z_{AB}(\tau) + c\pi\tau/6$ (with $k_B T = 1$) the potentials are given by:

$$U_{\text{like}}(d, r_1, r_2) = -\log\left(\chi_o(2\tau) + \chi_{1/2}(2\tau) + \sqrt{2}\chi_{1/16}(2\tau)\right) + \frac{\pi\tau}{12}$$

$$U_{\text{unlike}}(d, r_1, r_2) = -\log\left(\chi_o(2\tau) + \chi_{1/2}(2\tau) - \sqrt{2}\chi_{1/16}(2\tau)\right) + \frac{\pi\tau}{12}$$

$$U_{\text{Fr-Fr}}(d, r_1, r_2) = -\log\left(\chi_o(2\tau) + \chi_{1/2}(2\tau)\right) + \frac{\pi\tau}{12}$$

$$U_{\text{Fr-Fx}}(d, r_1, r_2) = -\log\left(\chi_o(2\tau) - \chi_{1/2}(2\tau)\right) + \frac{\pi\tau}{12}$$

(3.4)

with χ_h as defined in eq. 4.7, and τ as defined in eqs. 3.1 and 3.2. These potentials are plotted on regular and log-log graphs in figure 3.1. Their form is in agreement with the numerical results obtained using transfer matrix methods in [15].

At large d, we can examine the asymptotics of the potentials using the form of each potential in eq. 3.4 and the series expansion of the characters as shown in eq. 4.7. For fixed BCs, the leading contribution to the potential of mean force is equal to $\pm\sqrt{2(r_1 r_2)^{1/4}}d^{-\frac{1}{4}}$, with a sign which differs depending on whether the two BCs are like or unlike, in agreement with the point like approximation. For potentials that involve at least one 'free' BC, similar analysis shows that the leading contribution is proportional to d^{-2}. All four potentials diverge at short distances like $\pm d^{-1/2}$ where in all cases the sign is positive unless both BCs are identical. We note that the origins of the two techniques leading to the curves shown in fig. 3.1 are very different; arguably as different from each other as each are from a lipid bilayer. The very close agreement, even at lengths comparable to the lattice spacing speaks to the power of universality.

We also compare the form of the potential with Monte-Carlo results performed at temperatures away from the critical point where the potential has a range given roughly by ξ. In each case the resulting potential is a one di-

mensional cut through a four dimensional scaling function which could depend nontrivially on $d/r_1, d/r_2, d/\xi$ and the 'polar' coordinate $h/t^{\beta\delta}$ [117] describing the proximity to criticality. The dashed lines show the CFT prediction for $T = T_c$, with numerical results at 1.05, 1.1 and 1.2T_c, all for the 2×2 block sphere shown at right in fig. 3.3. The repulsive potential is both deepest and sharpest at T_c, while the the attractive force is sharpest slightly above T_c, with the final potential of very similar magnitude.

We expect our results to apply, with a few caveats, to proteins embedded in real cell membranes. Proteins couple to their surrounding composition through the height of their hydrophobic regions, interactions of their membrane-proximal amino acids with their closest lipid shell and by covalent attachment to certain lipids which themselves strongly segregate into one of the two low temperature phases. In simulation our proteins couple strongly to their nearest neighbor lipids leading to potentials in excellent agreement with CFT predictions that are very different in origin. These are expected to describe any uniform boundary condition in an Ising liquid, in the limit where all lengths are large compared to the lattice spacing. When separated by lengths of order a lipid spacing (1nm) we might expect additional corrections to this form, and in particular, a weakly coupled protein may have behavior intermediate between a 'free' and a 'fixed' BC. In addition, a protein that couples non-uniformly around its boundary might have interesting behavior not addressed here. We note that our boundary conditions couple to two long-ranged scaling fields- the magnetization field which falls off with the a power of $-1/4$ and the energy density which falls off with a power of -2, both of which must be present in membranes or any other system near an Ising critical point.

It is interesting to compare this composition mediated force to other forces that could act between membrane bound proteins. Electrostatic interactions are screened over around $1nm$ in the cellular environment, making them essentially a contact interaction from the perspective of the cell. There is an analogous shape fluctuation mediated Casimir force that falls off like d^{-6} [158, 159], and is therefore also very short ranged. Membrane curvature can also mediate forces with a leading attractive term that falls off like d^{-2} and a leading repulsive term that falls off like d^{-4}. Although they decay with a much larger power than the critical Casimir forces described above, curvature mediated potentials depend on elastic constants and are not bound to be of order $k_B T$ allowing them to become quite large at shorter distances. Using typical values [111] the potentials are comparable at lengths $\sim 5 - 10nm$ to the composition mediated potential we find here [32]. There are numerous examples of biology using these relatively short ranged but many $k_B T$ potentials for coordinating energetically expensive and highly irreversible events like vesiculation [111]. We propose that critical Casimir forces could mediate long ranged and reversible interactions useful for regulating a protein's binding partners. More generally, this work demonstrates that the hypothesis of criticality enables a quantitative understanding of the broad range of phenomena frequently associated with 'raft' heterogeneity in cell membrane.

3.5   Acknowledgements
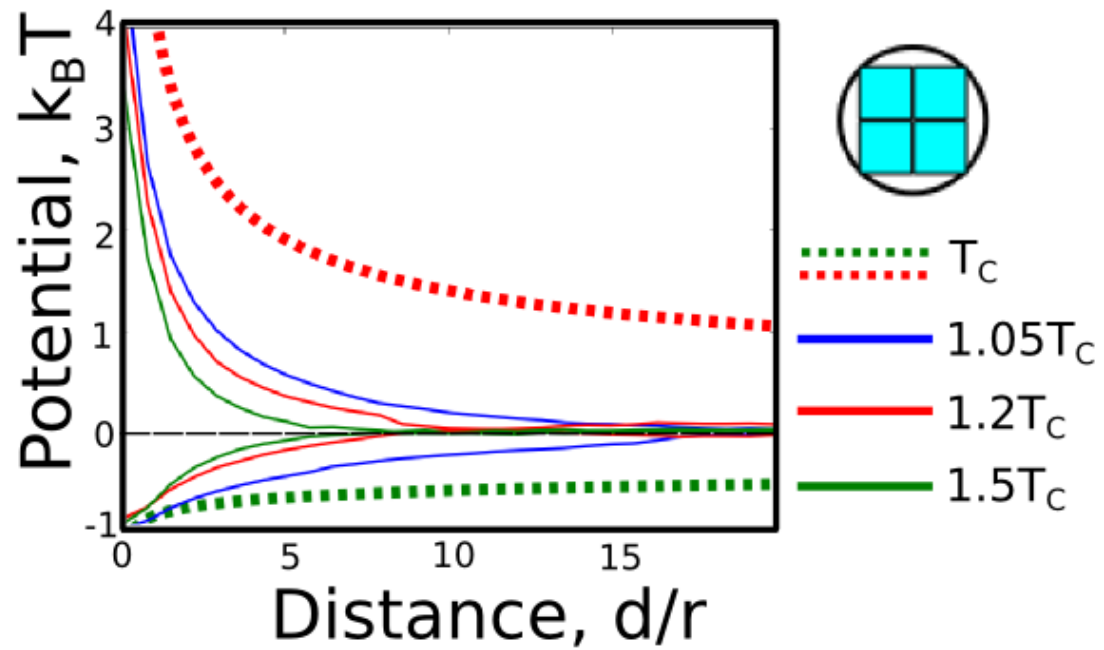
Figure 3.3: We compare our critical results with potentials obtained from Monte-Carlo simulations away from the critical point along the temperature axis. As can be seen, the potentials are longest ranged at the critical point. The repulsive interaction is also steepest at the critical point, though the attractive one has a larger force at short distances slightly away from the critical point.

CHAPTER 4

CRITICAL DYNAMICS IN SYNTHETIC MEMBRANES

Abstract[1] -Near a critical point, the time scale of thermally-induced fluctuations diverges as governed by the dynamic universality class. Accord between theory and measurement of critical exponents has been found for 3D, but not 2D, systems with conserved order parameter. Here we analyze time-dependent correlation functions to show that critical dynamics of a quasi-2D lipid bilayer in water agree with a recently predicted universality class. In particular, the effective dynamic exponent, z_{eff}, rises from ~ 2 to ~ 3 as the correlation length of fluctuations exceeds a characteristic hydrodynamic length.

4.1 Introduction

Lipids self-assemble in water to form sheets that are two molecules thick, within which the lipids are free to diffuse. When composed of several lipid species these two-dimensional (2D) liquid membranes can demix into coexisting liquid phases, termed L_o and L_d, over a range of temperatures and compositions, and can exhibit critical behavior [150, 41, 68, 69]. Among 2D critical phenomena, composition fluctuations in membranes are rather unique in that their large sizes and long decay times are accessible to optical microscopy. For example, Fig. 1 and supplementary movies show a vesicle (a spherical membrane shell) in which correlated regions reaching 10 μm persist for seconds 4.5. Direct visualization of these equilibrium fluctuations has recently been used to show that

---

[1]Most of this chapter was published in *Physical Review Letters* with first author Aurelia Honerkamp-Smith and Sarah L. Keller [70]. All experiments were performed by Aurelia Honerkamp-Smith and Sarah L. Keller, and analysis and writing was shared.

71

static critical exponents for lipid membranes are consistent with the 2D Ising universality class [68, 147]. Here we exploit the ability to visualize *dynamics* of these fluctuations to examine for the first time the dynamic critical phenomena in this system. We find that although the statics are 2D phenomena, the critical dynamics are modified by hydrodynamic coupling to the surrounding 3D fluid.

Static critical exponents, which describe how observables such as correlation length vary as the critical point is approached, are identical for all systems in a given universality class, independent of their detailed microscopic physics [53, 122]. For example, although membranes have a conserved order parameter and ferromagnets do not, membranes exhibit static exponents $\nu = 1.2 \pm 0.2$ and $\beta = 0.124 \pm 0.03$, consistent with the expected 2D Ising values of $\nu = 1$ and $\beta = 1/8$ [68]. Results in plasma membrane vesicles are also consistent with 2D Ising exponents $\nu = 1$ and $\gamma = 7/4$ [147]. Systems that are in the same static universality class can fall into different dynamic universality sub-classes determined by conservation laws constraining how fluctuations dissipate [64]. The critical exponent z for each dynamic subclass quantitatively describes the scaling of the dynamics. It relates how the correlation time τ_s diverges as temperature T approaches the critical temperature T_c, such that $\tau_s \propto |(T - T_c)/T_c|^{-\nu z}$ where ν is the static critical exponent. Experiments measure an effective exponent z_{eff} that approaches z as $T \to T_c$ and $\xi \to \infty$. Dynamic sub-classes relevant to 2D systems with conserved order parameter are notable equally for their wealth of theoretical predictions [64, 60, 74] and for the lack of experiments that systematically test those predictions.

Only a few previous measurements of dynamic critical exponents in 2D systems exist. Most experiments have been conducted on magnetic films.
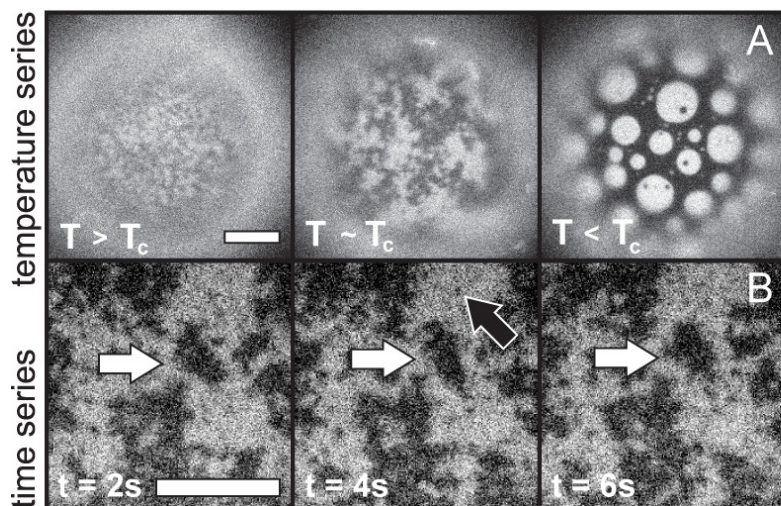
Figure 4.1: Fluorescence micrographs of vesicles of diameter 200 μm. (A) As temperature changes from $T > T_c$ ($T = 31.25$°C, $T_c \approx 30.9$) to $T \sim T_c$ ($T = 31.0$°C) fluctuations in lipid composition grow. Below T_c, at $T = 28$°C, domains appear. Scale bar = 10 μm. (B) A movie of composition fluctuations within a vesicle above T_c. Large fluctuations persist for seconds (white arrows), whereas small ones disappear by the next frame (black arrow). Scale bar = 20 μm.

Using ferromagnetic films of ~ two monolayers, Dunlavy and Venus found $vz = 2.09 \pm 0.06$, with $v = 1$ [34]. Fewer experiments have been conducted on systems with conserved order parameter. Careful attempts to measure z were made in thin films of lutidine and water, but were unable to reach the 2D critical regime [20]. In plasma membrane vesicles from living rat basophil leukemia cells, fluctuation decay times were reported to be consistent with $z \approx 2$ [147].

Here we obtain z_{eff} as T approaches T_c in a lipid membrane surrounded by water and compare to theory recently developed for an analogous system: a 2D critical binary fluid embedded in a non-critical bulk fluid [60, 74].

4.2 Theoretical overview

This new theory incorporates three essential features of lipid bilayer dynamics: conserved order parameter, collective hydrodynamics, and hydrodynamic coupling between the bilayer and bulk [60, 74]. Inclusion of only the first feature within an Ising model yields Model B, in which composition fluctuations dissipate through diffusion of microscopic constituents [64]. 2D Model B predicts $z = 4 - 2\beta = 3.75$ [64], and numerical schemes give $z = 3.80$ and $z = 3.95$ [156, 162]. Inclusion of the first *two* features, such that collective hydrodynamic motion replaces single particle diffusion as the dominant mechanism of order parameter relaxation, yields Model H. 2D Model H with coupling to only 2D momentum modes predicts $z \approx 2$ [64]. Inclusion of all *three* features yields Model HC, where HC denotes hydrodynamic coupling of the membrane to the bulk. This new version extends Model H to account for modes in both the 2D membrane and the 3D bulk fluid, with the result that $z = 3$ [60, 74].

Intuition for the role of the coupling between the membrane and bulk within Model HC can be gleaned from an approximation for 3D Model H by Kawasaki [78]. Critical fluctuations are treated as spherical inclusions of diameter ξ that diffuse a distance ξ to equilibrate [64, 78, 76, 126]. As such, correlation time varies as $\tau \sim \xi^2/D(\xi)$, where $D(\xi)$ is the inclusion's diffusion constant in a non-critical fluid. In 3D, $D(r) \sim 1/r$, where r is the inclusion's radius. Using $\tau \propto |(T - T_c)/T_c|^{-\nu z} \propto \xi^z$ yields $z \approx 3$. A more sophisticated theoretical treatment gives $z = 3.065$ [126]. Applying the same reasoning to 2D Model H, in which diffusion of inclusions has only a logarithmic dependence on r, yields $z \approx 2$. Again, more sophisticated treatments produce similar values; see 4.5 for more detail. This argument can be extended to predict the value z should take in a 2D

critical system embedded in a bulk fluid. Classic work by Saffman and Delbrück examined diffusion of an inclusion in a 2D liquid of viscosity η_{2D} immersed in a bulk fluid of 3D viscosity η_{3D}, where hydrodynamic length $L_h = \eta_{2D}/\eta_{3D}$ is an important parameter [115, 73]. When $r \gg L_h$, dissipation is primarily into the bulk and $D(r) \propto 1/r$ as in 3D Model H. When $r \ll L_h$, dissipation is primarily into 2D hydrodynamic modes and $D(r) \propto \ln(L_h/r)$, similar to 2D Model H. Two groups have independently noted that when L_h is considered, z_{eff} for a 2D critical binary fluid embedded in bulk liquid crosses over from $z_{eff} \approx 2$ when $\xi \ll L_h$ to $z_{eff} \approx 3$ when $\xi \gg L_h$ [60, 74].
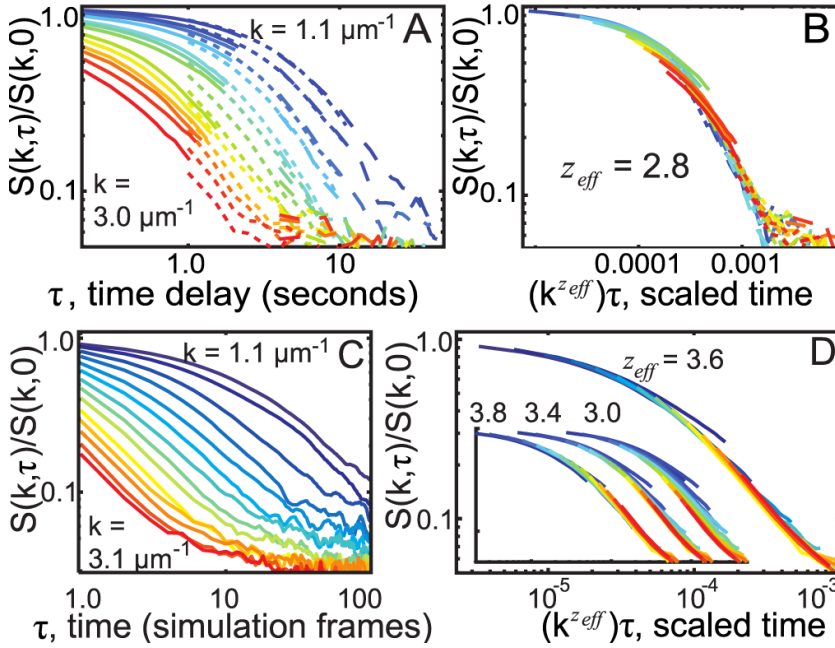
Figure 4.2: . (A and B) Rescaling experimental data closest to T_c by $k^z\tau$ collapses all curves to $z_{eff} = 2.8$, consistent with Model HC. Normalized structure factors are shown for $\xi = 13 \pm 2.2\ \mu m$ and three video rates: 10 frames per second (fps, solid lines), 2 fps (short dash), and 0.5 fps (long dash). Colors denote wavenumbers $k = 1.1\ \mu m^{-1}$ (top curve, blue) to $3.0\ \mu m^{-1}$ (bottom, red). (C and D) Simulations solely to verify technique. Structure factors of Kawasaki dynamics at $T = T_c$ blurred in time to mimic experimental limitations collapse at $z_{eff} = 3.6 \pm 0.2$, consistent with $z = 3.75$ for 2D Model B. Colors range from $k = 1.1$ μm^{-1} to $3.1\ \mu m^{-1}$. Insets show collapses used to determine bounds for z_{eff} and failure of collapse at $z_{eff} = 3$.

4.3 Results

The next four paragraphs demonstrate that experimental results here are in excellent agreement with the recent predictions of Model HC, namely that z_{eff} crosses over from ~ 2 to ~ 3 as $T \to T_c$ and $\xi \to \infty$. Further experimental details follow the results.

A time series of the order parameter, $m(r, t)$, was extracted from videos of vesicles collected via fluorescence microscopy. For membranes, $m(\vec{r})$ is the deviation from average composition as reported by an image's pixel grey scales. A time-correlation function $C(r, \tau)$, and its Fourier transform in space, the structure factor $S(k, \tau)$, were calculated for each wavenumber k.

Curves of $S(k, \tau)/S(k, 0)$ vs $k^{z_{eff}}\tau$ were plotted for a range of z_{eff} values. Fig. 2B illustrates how the correct z_{eff} was identified: for a single value of z_{eff}, all experimentally-measured curves at different k values (Fig. 2A) collapsed most fully onto a single curve, here at $z_{eff} = 2.8 \pm 0.2$. Fig. 3A shows z_{eff} values extracted in this manner from data over the entire measurable range of correlation lengths. In Fig. 3A, z_{eff} rises from from near 2 to near 3 as $T \to T_c$, in accord with Model HC [60, 74].

Fig. 2C-D validates this method by showing that standard simulations of Model B Kawaski dynamics that are blurred to mimic experimental limitations and then analyzed in the same way as the experimental data give $z = 3.6 \pm 0.2$ in agreement with the expected value of $z = 3.75$ (see 4.5 for details). Simulations were run on a 400x400 bi-periodic square lattice. Blur was achieved by averaging snapshots over 200 consecutive Monte Carlo sweeps, leaving a break of 800 sweeps without snapshots, and repeating the process, which reproduced

the effects of a camera shutter opening for 100 ms of every 500 ms.
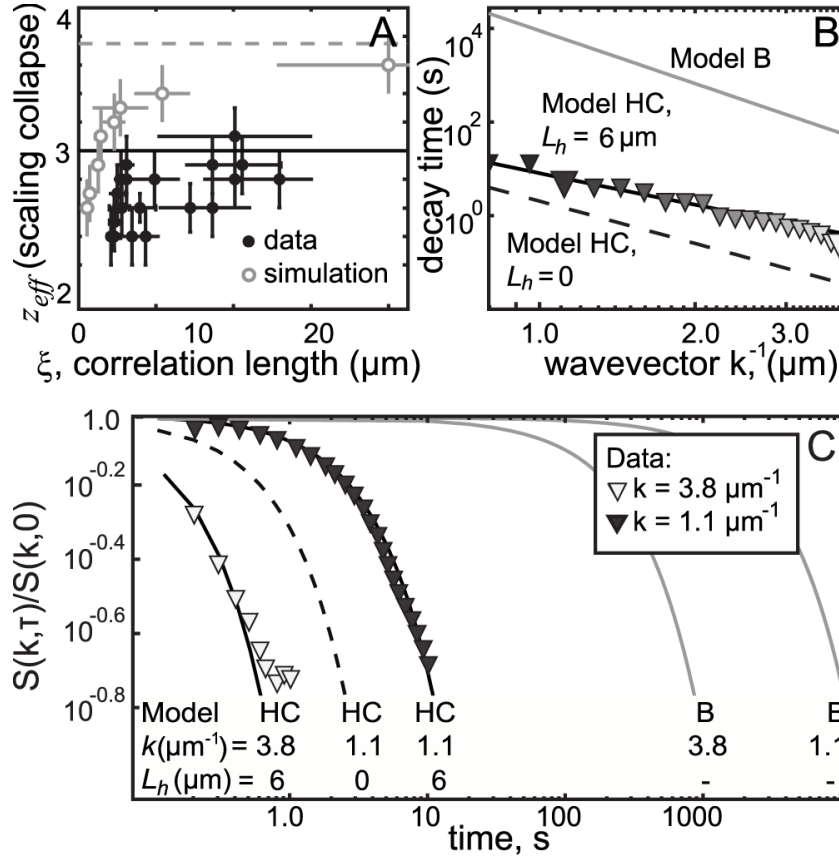
Figure 4.3: Data is in excellent agreement with Model HC. (A) Filled symbols: Dynamic exponent z_{eff} from scaling collapse of experimental data as in Fig. 2A-B. Open symbols: Model B simulation in which z_{eff} approaches ~ 3.75. (B) Decay time, defined as when $S(k,\tau)/S(k,0) = e^{-1}$. Large symbols indicate wavenumbers 1.1 and 3.3 μm^{-1}. (C) Normalized structure factors $S(k,\tau)/S(k,0)$. In panels B and C, experimental data is denoted by symbols, 2D Model B by a grey line, Model HC (HC) with $L_{\text{h}} = 6$ μm by a solid line and Model HC with $L_{\text{h}} = 0$ by a dashed line.

Excellent agreement between predicted and measured structure factors provides even stronger evidence that Model HC describes critical dynamics in membranes. Inaura and Fujitani give a prediction for the entire time-dependent structure factor $S(k,\tau)$ for Model HC, taking as input η_{2D}, η_{3D}, and a mean-field approximation for the static structure factor, $S(k,0)$ [74]. The ratio $S(k,\tau)/S(k,0)$ and its decay time will be compared between theory and experiment below. A

feature of $S(k, \tau)/S(k, 0)$ is that it needs no correction due to the microscope's point spread function. Ratios of $S(k, \tau)/S(k, 0)$ in the critical Ising model and in the mean-field approximation are similar, and do not depend strongly on correlation length, as will be shown in a future manuscript.

The HC model with $L_h = 6 \, \mu$m fits the data over all experimentally accessible wavenumbers. Fig. 3C shows the ratio $S(k, \tau)/S(k, 0)$ at wavenumbers $1.1 \, \mu\text{m}^{-1}$ and $3.8 \, \mu\text{m}^{-1}$. Fig. 3B shows decay times, defined as when $S(k, \tau)/S(k, 0) = e^{-1}$. All other models are excluded. Fig. 3A rules out 2D Model H because the measured z_{eff} rises close to 3, well above the predicted value of 2 for 2D model H. Fig. 3B-C rules out 2D Model B because measured decay times are orders of magnitude shorter than the model predicts.

Developing Model HC to completely describe membranes requires determining only membrane viscosity, η_{2D}, as an input since the viscosity of water, η_{3D}, is known. Fig. 3C indicates that η_{2D} must be nonzero. In the small k limit, Inaura and Fujitani [74] predict a structure factor that depends only on η_{3D}. This parameter-free prediction, equivalent to taking $\eta_{2D} = 0$, underestimates time decays by a factor of $5 - 10$ (dashed curve, Fig. 3C). Setting the unknown η_{2D} (or equivalently, $L_h = \eta_{2D}/\eta_{3D}$) as a single fit parameter within Model HC over the entire measured range of k yields $L_h = 6.0 \pm 1.5 \, \mu$m. This value is within the range found by tracking diffusion of liquid domains across vesicle surfaces [23, 104] and is similar to values (2-4 μm) found by other methods, albeit for different lipid mixtures [17, 31]. An essentially equivalent method of finding L_h is to calculate the Model HC structure factor using the formalism of Hohenberg and Halperin [64], and to thereby extend Model HC to incorporate Ising rather than mean field statics. Within experimental uncertainty, this mod-

est change has no effect (L_h = 5.5 ± 1.5 μm). This and other extensions of Model HC, each leading to small corrections to the ratio $S(k, \tau)/S(k, 0)$, will appear in a future manuscript.

4.4   Methods

Using lipid bilayers to measure critical exponents introduces both complexities and advantages, which are outlined further in 4.5. The first complexity is that the simplest bilayers that exhibit critical phenomena contain ternary lipid compositions. Strictly speaking, the ternary mixtures used here pass through isothermal critical mixing (plait) points rather than critical (col) points. A feature of 2D systems is that, unlike in 3D systems, no measurable change in critical exponents arises from the presence of a third component. Briefly, a small correction to scaling arises in systems that contain a third component at fixed composition rather than fixed chemical potential. Hence, T_c changes, and many effective critical exponents are renormalized by a factor of $1/(1 - \alpha)$, as discovered by Widom [153] and generalized by Fisher [44]. For the 2D Ising case here, where $\alpha = 0$, theory predicts only a logarithmic correction to singular behavior [153]. The second complexity is that when T is changed (as required in previous studies to find ν and β [68], but not required here), a bilayer with fixed composition does not necessarily follow a path with constant $\langle m(\vec{r}) \rangle$ [164]. However, since membrane phase diagrams are relatively symmetric over the range of temperatures probed and since measured values of ν and β were consistent with the 2D Ising model [68], deviations from a path of constant $\langle m(\vec{r}) \rangle$ are likely minor.

The first advantage of using lipid bilayers is that it avoids challenges of other

systems. For example, lipid monolayers have confounding effects of dipole interactions, and the task of achieving simultaneous tunability and stability of surface pressure in a stationary monolayer is formidable. The second is that correlation lengths are large, partly because ξ_0 within the relation $\xi = \xi_0 |(T - T_c)/T_c|^{-\nu}$ is on the order of the length of a lipid molecule rather than of an atom. Separately, there is an advantage in using 2D (or quasi-2D) experimental systems over 3D systems. The critical region is larger in 2D liquid-liquid critical systems than in analogous 3D ones, partially due to differences between critical exponents in 2D vs 3D Ising classes ($\nu = 1$ and $\beta = 1/8$ in 2D vs $\nu \approx 0.630$ and $\beta \approx 0.325$ in 3D [53]).

Methods used to produce the results in Fig. 3 follow. To optimize movie quality, vesicles were spherical, free-floating, unilamellar, of radius >100 μm, and electroformed by standard methods detailed in [68]. Vesicles were formed from mixtures along a line of plait points centered at 30% diphytanoylphosphatidylcholine (DiPhyPC), 20% dipalmitoylphosphatidylcholine (DPPC) and 50% cholesterol (chol), with 0.5% fluorescent dye Texas red dipalmitoylphosphatidylethanolamine (TR-DPPE). Only vesicles near a plait point were analyzed, identified by micron-scale composition fluctuations visible over the largest observed range of temperatures (> 1°C) and by equal areas of coexisting liquid phases below T_c. Each vesicle analyzed fell on a slightly different plait point, so each had a slightly different T_c [149].

Images of membranes were captured via an epifluorescence microscope with a temperature-controlled stage and a mercury lamp source. Light exposure was minimized by employing a SmartShutter (Sutter Instrument, Novato CA) controlled through NIS-Elements (Nikon, Melville NY) and by recording movies for

at least two different frame rates at each temperature. Each frame was exposed 100-150 ms, with the shutter open 10 ms before and after exposures. Movies were collected from high to low temperature in steps of $\sim 0.2°C$, equilibrated for at least 2 min. No consistent trend in intensity was observed throughout each movie, implying that the low light procedures used here eliminated significant photobleaching. To correct for lamp flickering, mean brightness was subtracted from each frame. Spatial intensity gradients due to other vesicles outside the focal plane were removed by a long wavelength filter of 100 pixels.

Images were analyzed via custom MATLAB code (The Mathworks, Natick, MA). Vesicles were tracked and centered to remove drift (typically < $25\mu m/$min). By eye, features exhibit no net translation, which implies no significant vesicle rolling. No difference in mean intensity or noise between pixels at edges vs. centers of cropped images was observed, implying that vesicles are so large that membrane curvature over images can be neglected [68]. Curvature corrections in smaller vesicles were minor [147].

The structure factor $S(k, \tau)$, the Fourier transform in space of the time-dependent correlation function, was found as previously described [68, 135]. Briefly, a discrete transform was performed for each movie image, with a buffer of zero values to correct for image non-periodicity. Transformed images were divided by the microscope's finite point spread function to yield $m(\vec{k}, t)$. The dynamic structure factor was generated at each τ by $S(\vec{k}, \tau) = 1/2 \left\langle m(\vec{k}, t)\overline{m(\vec{k}, t \pm \tau)} \right\rangle$, where $\overline{m(\vec{k}, t)}$ is the complex conjugate of $m(\vec{k}, t)$ [80]. $S(\vec{k}, \tau)$ was then radially averaged to yield $S(k, \tau)$.

Structure factors were employed in two ways. First, correlation lengths, ξ, were found by analyzing structure factors at $\tau = 0$. Specifically, a one-parameter

fit for ξ was made until all data for $k^{(7/4)}S(k)$ vs. $k\xi$ collapsed onto the single curve for the exact numerical solution of the 2D Ising model [155, 68]. Second, effective dynamic scaling exponents, z_{eff}, were found by collapsing curves of $S(k, \tau)$ (see results above and 4.5 for details). Collapse works because, according to the dynamic scaling hypothesis, structure factors within the scaling regime can be written in the form $S(k, \tau, \xi) = k^{-2+\eta}\Omega((k\xi)^{-1}, k^z\tau)$ where Ω is a universal function of $(k\xi)^{-1}$ and $k^z\tau$ [64]. Near T_c, where $(k\xi)^{-1}$ is near 0, curves of $S(k, \tau)/S(k, 0)$ vs $k^z\tau$ collected over many wavenumbers k should collapse via a one-parameter fit to produce the correct value of z. Here, Ω can also depend on kL_{h}, so that $S(k, \tau, \xi) = k^{-2+\eta}\Omega((k\xi)^{-1}, k^z\tau, kL_{\mathrm{h}})$. For collapses in Fig. 2A-B, z_{eff} refers to an effective z value which varies as ξ/L_{h} is changed. In Fig. 3B-C, comparing the entire form of the structure factor to theoretical predictions directly verifies the value of z as well as the dependence of the universal function on kL_{h} and $k^z\tau$.

Summary: Directly imaging composition fluctuations enables measurement of effective dynamic critical exponents of a lipid membrane embedded in bulk water. Experimental structure factors are in excellent agreement with an emerging theoretical prediction in which 3D hydrodynamics affects critical slowing down in a 2D membrane. The theory invokes hydrodynamic coupling between the membrane and bulk fluid such that Ising degrees of freedom are coupled to momentum modes [60, 74]. As predicted, a shift in z_{eff} from ~ 2 to ~ 3 as $T \to T_c$ and $\xi \to \infty$ is observed.

kindly provided the domain-tracking Matlab routine [68] customized here. J.R. Ashcraft, M.E. Cates, R.E. Goldstein, M. Haataja, T. Lubensky, D.R. Nelson, M. den Nijs, P.D. Olmsted, G. Garbès Putzel, M. Schick, J.V. Sengers, J.P. Sethna, S.L. Veatch, B. Widom and A. Yethiraj are thanked for insightful conversations.

4.5 Supplemental material

4.5.1 Introduction

This supplemental section contains details regarding analysis, calculation, and theory not found in the main text. Two movies are also included as supplementary material, where Movie 1 is at $30.25°C$, and Movie 2 is at $29.75°C$, with $T_c \approx 29.5°C$. Both movies are $35\mu m$ wide. Section 4.5.2 contains additional information on analysis procedures. Section 4.5.3 explains why Fisher renormalization does not affect the observed static critical exponents in 2D Ising systems, and why lipid membrane systems can have larger correlation lengths than binary liquids in 3D. Section 6.7 details the Ising model simulations that we used to verify our analysis. Section 4.5.5 reviews previous theoretical results for purely 2D critical hydrodynamics.

4.5.2 Details of analysis

In the definition of $S(\vec{k}, \tau) = \left\langle m(\vec{k}, t) \overline{m(\vec{k}, t + \tau)} \right\rangle$, the value of $S(k, \tau = 0)$ is guaranteed to be real not only as an expectation value but from run to run since each term appears with its complex conjugate. For $\tau \neq 0$, the expectation value

83

of the imaginary part of S is guaranteed to be real by time-reversal invariance expected of systems in equilibrium. However, each term contributes an imaginary component. Adding the complex conjugate and dividing by two leads to an effective measurement of $1/2(s(k, \tau) + s(k, -\tau))$, which for an equilibrium system is equal to $S(k, \tau)$. The inclusion of zeros required to pad the raw data in $m(k, t)$ introduces a small error in the calculation of $S(k, \tau)$ which can be corrected for by dividing $S(k, \tau)$ by the correlation function of pure ones and zeros in the real space correlation function. For calculations in k-space, there is no simple correction (the real space correction has an ill-posed Fourier transform and so introduces unacceptable noise in k-space). Nevertheless, any correction is expected to be small (values of $S(k, \tau)$ were similar when calculated with vs without zero padding). More importantly, any correction would cancel out of the main results presented here because values are divided by $S(k, \tau = 0)$. For movies at the slowest frame rate, 0.5 fps, noise in $S(k, 0)$ caused an offset from the rest of the structure factor. For calculations made with those data sets, the measured value of $S(k, 0)$ was replaced by the value extrapolated from an exponential fit to the 2nd through 5th points in $S(k, \tau)$.

4.5.3 Experimental advantages of lipid bilayers

This section explains why Fisher renormalization does not affect the observed static critical exponents in 2D Ising systems, and why lipid membrane systems can have larger correlation lengths than binary liquids in 3D.

Widom-Fisher rescaling leads to only an immeasurably small correction to 2D critical exponents: Concentration fluctuations consistent with static 2D Ising criti-

cal exponents were previously observed in membranes over our entire range of $k\xi$ [68]. As we show below, this observation is not at odds with the fact that our ternary system is subject to rescalings first discovered by Widom [153] and generalized by Fisher [44]. Rescaling corrections apply to any system with a quantity whose chemical potential smoothly affects the critical temperature. When a component is instead held at fixed composition (as our three components are) then the observed critical behavior receives non-analytic corrections, essentially because the chemical potential of the third component has singular behavior near the critical point when held at fixed composition. As a result, the singular form of the coexistence curve near the critical point is changed from its usual exponent β to $\beta' = \beta/(1 - \alpha)$. Here α is the static critical exponent for specific heat. Other critical exponents that relate singular behavior of a quantity to the distance in temperature from the fixed point (for example α, β, ν and γ) receive similar corrections. For example, the specific heat exponent itself becomes $\alpha' = \alpha/(1 - \alpha)$[44]. The rescaling correction is not confined to ternary systems: binary systems held at fixed density, rather than fixed pressure undergo similar rescalings, as does any system in which a density variable is held fixed in a phase diagram rather than it's conjugate field.

Fortunately for the current study, Widom-Fisher rescaling in the 2D Ising model leads to an immeasurably small change in the singular behavior and no change in the critical exponents themselves. As noted above, α is the static critical exponent for specific heat, C, which diverges as $C \sim ((T - T_c)/T_c)^{-\alpha}$. In the 2D Ising model, specific heat diverges as $C \sim \log((T - T_c)/T_c)$, which is slower than any power law divergence, so that α is said to be zero. As explicitly discussed in both [153] and [44], there is potentially a logarithmic correction to the singular behavior of quantities whose critical exponents are usually multiplied

by $(1 - \alpha)^{-1}$. For example, the correlation length ξ, which is usually written as $\xi \propto (\frac{T-T_c}{T_c})^{-\nu}$, becomes $\xi \propto (\frac{-\log(T-T_c)(T-T_c)}{T_c})^{-\nu}$ after rescaling. In this case, $\nu' = \nu$, so rescaling does not change the critical exponent. For a system described by the 3D Ising model (rather than the 2D Ising model as in the current study), $\alpha \approx 0.11$ [44, 21], such that the effect of rescaling is small but observable in the critical exponents.

Although the effect of rescaling on the dynamic exponent z is not discussed explicitly in the literature, we expect that z would not be affected by rescaling even for systems in which $\alpha \neq 0$. The dynamic exponent z describes scaling of the time scale as the length scale is changed, with $\tau_{system} \propto \xi^z$. The product νz describes critical slowing with respect to temperature, where $\tau_{system} \propto (\frac{T-T_c}{T_c})^{\nu z}$. As such, νz does describe the singular behavior of a quantity (here the time scale) as temperature is changed and it receives a correction of $\frac{1}{1-\alpha}$ through the parameter ν.

Values of static critical exponents β and ν allow for a large correlation length ξ: Correlation lengths $\xi \sim 10 \mu m$ are regularly observed in vesicle membranes. These correlation lengths are larger than those typically observed in 3D binary mixtures, even though control over lipid composition in membranes is coarser. As described in the main text, 2D critical exponents allow for coarser tuning in temperature and composition for a given correlation length. Also, lipids are molecules with length scales of $\xi_0 \sim 1nm$, whereas molecules employed in many studies of 3D critical phenomena are an order of magnitude smaller, with $\xi_0 \sim 0.1nm$. The length scale ξ_0 is a prefactor for the correlation length as seen in the scaling form of the correlation length: $\xi = \xi_0 t^{-\nu} \mathcal{U}\left(\phi^{1/\beta} t^{-\nu}\right)$ where $t = (T_c/(T - T_c))$ and where ϕ, the magnetization, is linearly related to compo-

sition. $\mathcal{U}(x)$ is a universal function that is monotonically decreasing in x. For large x, $\mathcal{U}(x) \sim 1/x$, and it can be normalized such that $\mathcal{U}(0) = 1$.

4.5.4 Simulation details

Simulation procedures were standard [103, 122] and briefly explained here. The standard Ising Hamiltonian given by $H = -\sum_{\{i,j\}} s_i s_j$ was used, with spin variables $s_i = \pm 1$ and summation over the four nearest neighbors (j) of every state (i). Temperatures were in terms of the exact critical temperature given by the Onsager solution [106], $T_C = 2/\log(1 + \sqrt{2})$ so that a reduced temperature $t = (T - T_c)/T_c$ corresponds to a simulation temperature of $T_{sim} = 2.269(1 + t)$. In this section, T and ΔH correspond to temperature and to the change in energy between initial and final states, respectively. Both are in dimensionless units. In a Monte-Carlo 'sweep', $160,000$ (400^2) pairs of spins were proposed to be swapped, such that each spin was proposed twice. Metropolis spin exchanges were used; each pair was exchanged or not to satisfy detailed balance [103, 122]. If the resulting configuration was lower in energy, the exchange was accepted. If energy increased, the exchange was accepted stochastically with probability $\exp(-\Delta H/T)$.

Note that any dynamics that satisfy detailed balance will lead to the same equilibrium ensemble of configurations [122]. To rapidly equilibrate the system, 'nonlocal' moves were employed in which each of a pair of spins were chosen from all sites on the lattice. Equilibration is very rapid using these nonlocal dynamics since they approximate "Model A" for large systems where z is near 2 [64]. The system was equilibrated for $100,000$ sweeps using nonlocal moves

starting from a distribution that contained the desired fraction of up spins but was otherwise random. $100,000$ sweeps is much longer than the decay time of the slowest decaying system used here. The decay time is approximately 1000 sweeps at $1.05T_C$, which can be seen qualitatively by inspecting successive snapshots or quantitatively by inspecting the decay of time dependent correlation functions. Once the system was equilibrated, dynamics relevant for the locally conserved order parameter (Kawasaki Dynamics) were employed. In this case, a single spin and one of its four nearest neighbors were chosen to form a pair proposed to be swapped.

4.5.5 Predictions for binary liquids in 2D

Model H for binary fluids in 2D predicts $z \approx 2$ using $z = 4 - \eta - x_\lambda$, where $\eta = 2\beta$ is a static critical exponent and x_λ must be calculated from an epsilon expansion (where $\epsilon = 4 - D$, and D is the number of dimensions). This yields $x_\lambda = 18/19(1 - (\text{constant})\epsilon + O\epsilon^2)$ where the constant is either 0.033 [126] or 0.039 [61]. Since the constant is small, it is plausible that the expansion applies even when $\epsilon = 2$, yielding $z = 2.00$ (which also arises from a much simpler mean field argument) or 1.98. Simulations in $2D$ binary liquids are reportedly challenging and we know of none that either verify or contradict the prediction that $z = 2$. Measurements in bulk 3D liquids far from T_c find that $z_{eff} = 2$ (e.g. [85, 134, 16]).

4.5.6 $k\xi$ of order 1 is a small correction to $\Gamma(k)$

This section shows that the seemingly drastic approximation of $(k\xi)^{-1} = 0$ in the calculation of the decay rate leads to only a small correction to $\Gamma(k)$. As such, the approximation is made in the bulk of our analysis so that one less fit parameter is carried. For plots in the main text, the exact static susceptibility at T_c of $\chi_m(k) = k^{-2+\eta}$ is used, with $\eta = 1/4$. (As can be seen in equations 4.13 and 4.14, the absolute scale of χ_m does not enter into Γ or μ). However, the actual structure factor approaches a constant, rather than infinity as $k \to 0$. To understand the effects of the approximation, a simple form is used that is similar to one commonly used when $\eta = 0$: $\chi_m(k) = (\xi^{-2} + k^2)^{-1+\eta/2}$. Using this static structure factor, a comparison is possible between $\Gamma_\xi(k)$ when the correlation length ξ is finite vs. infinite. In Supplement Fig. 4.4, the ratio $\Gamma_{\xi=10\mu m}(k)/\Gamma_{\xi=\infty}(k)$ vs k is plotted for values of k from nm^{-1} to mm^{-1}. As with Fig. 3B and C of the main text, $L_h = 5.5\mu m$ is used. In the experimentally probed region (bounded by the red dots) the ratio $\Gamma_{\xi=10\mu m}(k)/\Gamma_{\xi=\infty}(k)$ is always within ± 0.03 of the value of 1, which justifies dropping it from most analysis. Interestingly, in the region $k\xi \sim 1$ there is a local minimum in the ratio. This means that for a small range of k vectors near $k \sim \xi^{-1}$, moving closer to a critical point actually increases the speed with which some modes relax. For $k \ll \xi^{-1}$, $\Gamma(k)$ becomes proportional to k^2 rather than k^3, so that the ratio increases like $1/k$ for sufficiently small k.

4.6 Hydrodynamic mode coupling calculation

We use a perturbative mode coupling calculation similar to that for 3D fluids [64, 126] and for 2D membranes in water [74]. To [74] we add the use of the

$$\frac{\Gamma\,(\xi = 10\,\mu\mathrm{m})}{\Gamma\,(\xi = \infty)}$$

2

1.5

0.5

0.001   0.01   0.1   1   10   100   1000 $k,\ \mu\mathrm{m}^{-1}$
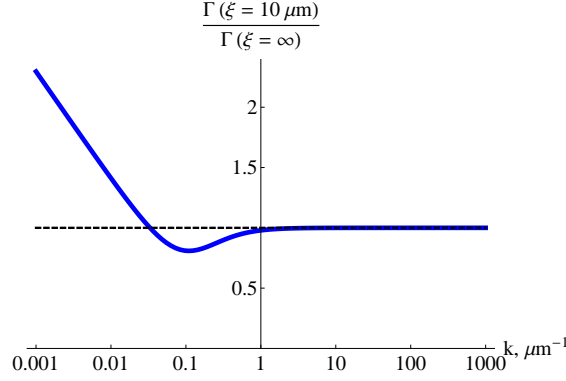
Figure 4.4: In the hydrodynamic theory described here, the value of $\Gamma(k)$ does not depend strongly on the value of ξ in the static structure factor over the range explored experimentally in this study. Experimentally measured values of ξ are on the order of $10\mu m$ ($15\mu m$ in Fig. 3B and C of the main text). This is quantified by the ratio $\Gamma_{\xi=10\mu m}(k)/\Gamma_{\xi=\infty}(k)$, where $\Gamma_{\xi}(k)$ is the decay rate predicted by the theory outlined in section 4.6 with static correlation length ξ. This ratio is plotted over a range of k values, with the fit value of the hydrodynamic length $L_h = 5.5\mu m$. Over the range of k values probed experimentally ($0.8(\mu m)^{-1} < k < 4(\mu m)^{-1}$, bounded by the red dots), the farthest this ratio deviates from a value of 1 is by 0.03.

Ising static structure factor and the formalism used in [64, 126], which allows us to take into account the back-action of Ising degrees of freedom on momentum modes in the limit where the membrane viscosity is zero. The model H variant contains order parameter modes and momentum modes with the following free energy functional:

$$F = F_0\,\{m\,(r)\} + \int d^3\vec{r}\,\frac{\left|W(\vec{r})\right|^2}{2\rho_{3D}} + \int d^2\vec{r}\,\frac{\left|V(\vec{r})\right|^2}{2\rho_{2D}}$$
$$+ \int d^2 r(-h_m(r)m(r) - h_V(r)V(r)) \tag{4.1}$$

Here $F_0\,\{m\,(r)\}$ is the free energy functional for the Ising modes $m(r)$. The hydrodynamic modes $W(r)$ describe the local $3D$ momentum density, where ρ_{3D} is the density of water. The 2D momentum modes are related to the 3D ones by: $V(x, y) = (\rho_{2D}/\rho_{3D})W(x, y, 0)$. The applied fields, h, are used in defining the susceptibilities, $\langle V(k, \omega)\rangle = \chi_V\,(k, \omega)\,h_V(k, \omega)$ and $\langle m(k, \omega)\rangle = \chi_m\,(k, \omega)\,h_V(k, \omega)$. The

fluid momentum modes are vectors, but the incompressibiliy condition makes them effectively scalars here. In k-space, the modes must be tranverse, which in 2D allows for only a single polarization. In 3D, there are always two allowed polarizations. However, a flat membrane enforces the condition that the z-component of the velocity be identically 0 at $z=0$, and so the z-component of the velocity does not couple to the membrane. Each k-vector in 3D then has a single allowed polarization perpendicular to both $\hat{z}$ and $\hat{k}^{-1}$.

The dynamics are specified by diffusion of the order parameter (which is not relevant), viscous dissipation of the hydrodynamic modes, and a Poisson bracket relation between the momentum modes and the order parameter, which enforce that the velocity field carries the order parameter along with it. The defining equations are given by:

$$\partial_t m_{(z=0)} = \lambda_0 \nabla_{2D}^2 \frac{\delta F}{\delta m} - g_0 \nabla_{2D} m \cdot \frac{\delta F}{\delta W} \tag{4.2}$$

$$\partial_t W_{(z \neq 0)} = \mathcal{T} \left[\eta_{3D} \nabla_{3D}^2 \frac{\delta F}{\delta W} \right] \tag{4.3}$$

$$\partial_t W_{(z=0)} = \mathcal{T} \left[\eta_{2D} \nabla_{2D}^2 \frac{\delta F}{\delta W} - g_0 \nabla_{2D} m \cdot \frac{\delta F}{\delta m} \right.$$
$$\left. + \eta_{3D} \frac{\partial}{\partial z} (\frac{\delta F}{\delta W}) \mid_{z=0^+} - \eta_{3D} \frac{\partial}{\partial z} (\frac{\delta F}{\delta W}) \mid_{z=0^-} \right] \tag{4.4}$$

where noise terms to enforce equilibrium statistics are not written, and where η_{2D} and η_{3D} are the viscosities of the 2D membrane and the 3D bulk, respectively. The operator $\mathcal{T}$ enforces the incompressibility condition and in k-space reads $(\mathcal{T}_k)_{ab} = (\delta_{ab} - \frac{k_a k_b}{k^2})$. The constant g_0 will eventually be set to 1, and the calculation will be in powers of g_0^2. The term proportional to λ_0 gives a diffusive contribution that is sub-dominant, and that we henceforth drop. We wish to find the frequency dependent susceptibilities of the 2D momentum modes V and the Ising modes m. The susceptibility of a mode is related to its structure factor by the fluctuation dissipation theorem (see [64] for a discussion), which relates the

Fourier transforms in time of the structure factor, $\hat{S}$ and susceptibility, $\hat{\chi}$:

$$\hat{S}(\vec{k}, \omega) = \frac{2k_B T}{\omega} \text{Im} \hat{\chi}(\vec{k}, \omega) \tag{4.5}$$

An important corrolary relates the static structure factor to the zero frequency susceptibility:

$$S(\vec{k}, t = 0) = k_B T \hat{\chi}(\vec{k}, \omega = 0) \tag{4.6}$$

As in [64], we assume that these have the form:

$$\chi_m^{-1}(k, \omega) = (1 - i\omega/\Gamma(k))\chi_m^{-1}(k) \tag{4.7}$$

$$\chi_V^{-1}(k, \omega) = \rho_{2D} - i\omega/\mu(k) \tag{4.8}$$

where $\chi_m(k)$ is the static susceptibility of the Ising modes. This form gives a time dependent structure factor that decays exponentially in time. It remains to find the unknown $\mu(k)$ and $\Gamma(k)$, the decay rates of the 2D momentum and Ising modes. First, the form of $\mu(k)$ is found to zeroth order in g_0, which is called $\mu_0(k)$. To do this, solutions for V of equations 4.3 and 4.4 were found with applied field in the $\hat{y}$ direction $h_V(r, t) = h_V(k, \omega)e^{ikx - i\omega t}$. This is solved by the following momentum field in 3D:

$$W = \frac{\rho_{3D}}{\rho_{2D}} \chi_V(k, \omega) \exp(ikx - i\omega t - \tilde{k}z) h_V(k, \omega) \tag{4.9}$$

$$\text{with } \tilde{k} = \sqrt{k^2 - i\frac{\rho_{3D}}{\eta_{3D}}\omega} \approx k \text{ for } \omega << \frac{\eta_{3D}k^2}{\rho_{3D}} \tag{4.10}$$

$$\text{and } \chi_V(k, \omega) = \rho_{2D}\frac{-i\omega}{2\eta_{3D}k + 2\eta_{2D}k^2} \tag{4.11}$$

where $\omega << \frac{\eta_{3D}k^2}{\rho_{3D}} \approx 10^6 (\mu m^2/s)k^2$ is valid over the range of ω and k values that are relevant here. This yields:

$$\mu_0(k) = \eta_{2D}k^2 + 2\eta_{3D}k = \eta_{3D}(2k + k^2 L_h) \tag{4.12}$$

where $L_h = \eta_{2D}/\eta_{3D}$. An identical result was obtained in [74] by assuming that the three dimensional flow is given by the steady state Stokes flow with the velocity field in the membrane acting as a boundary condition for the bulk fluid.

To calculate the susceptibilities to second order in g_0, integration was performed over mode couplings. Vertices proportional to g_0 couple two Ising modes and a velocity mode. The result is a pair of self-consistent equations (see [64] for details):

$$\Gamma(k) = g_0^2 \chi_m^{-1}(k) \int \frac{d^2p}{(2\pi)^2} \chi_m(p^+) \frac{kT_pk}{\mu(p^-)} \tag{4.13}$$

$$\mu(k) = \mu_0(k) +$$
$$g_0^2 \int \frac{d^2p}{(2\pi)^2} \frac{\chi_m(p^-)[\chi_m^{-1}(p^+) - \chi_m^{-1}(p^-)]pT_kp}{\Gamma(p^+) + \Gamma(p^-)} \tag{4.14}$$

where $p^{\pm} = p \pm k/2$. From these equations, several limits can be seen. In the limit where $L_h = 0$ (when the membrane viscosity is 0), $\Gamma(k) \propto k^3$, and $\mu(k) \propto k$. When η_{3D} can be neglected, $\Gamma(k) \propto k^2$, and $\mu(k) \propto k^2$ are found, both of which are in agreement with the scaling arguments discussed in the main text and as first argued in [60].

At present, solutions to equations 4.13 and 4.14 have not been found for a general set of parameters. Instead, here the equations are solved in two limits. In both cases, the Ising critical static structure factor is used at its critical point, $\chi_m(k) = k^{-2+\eta}$ to minimize fit parameters, although using an off-critical structure factor gives quantitatively indistinguishable results (discussed in section 4.5.6). In the limit in which $L_h = 0$, both $\mu(k)$ and $\Gamma(k)$ are power laws with prefactors that can be algebraically found after numerically solving the two integrals. In that case, $\mu(k) = 2.21\eta_{3D}k = 1.11\mu_0(k)$ and $\Gamma(k) = (.094k_BT/\eta_{3D})k^3$. It is this complete solution to the pair of equations at T_c that is used within this work for all theory predictions labeled with $L_h = 0$. At finite L_h no method of self-consistently solving the equations was found even when $\xi = \infty$. Instead $\mu_0(k)$ was used in place of $\mu(k)$, following [74]. We hope to present a complete self-consistent numerical solution that considers ξ and L_h in a later publication.

Although it is of theoretical interest, it is expected that inclusion of the full $\mu(k)$ rather than of only $\mu_0(k)$ will be a small correction. In the case in which $L_h = 0$, Γ is simply reduced to $\sim .9$ of its value without viscosity renormalization, and the scaling exponent is unchanged. By contrast, in purely 3D systems the viscosity renormalization does change the scaling exponent z, although by only a very small amount.

CHAPTER 5

CRITICALITY AND ANESTHESIA

Abstract [1] Giant Plasma Membrane Vesicles (GPMVs) taken from living Rat immune cells are tuned close to a liquid-liquid critical point that can be found by lowering temperature to around 295K. We demonstrate that the n-alcohol series of general anesthetics depress the transition temperature of these GPMVs by $\sim$ 4K. This change is much larger than similar changes seen in synthetic lipid systems after addition of anesthetics, and we argue that it is sufficient to potentially explain the phenomenology of anesthesia, without the need for any specific binding of anesthetics to particular proteins. In addition, we propose a simple model for an allosteric receptor that couples to the composition of the membrane surrounding it through its boundary conditions. Such a receptor would generically have its sensitivity to ligand changed by the addition of anesthetics. Our simulations predict changes to the dose-response curve of a hypothetical GABA sensitive channel that are similar to the changes seen in GABA-A channel conductance that are thought to mediate the effects of anesthesia.

5.1 Background

An enormous range of molecules, spanning inert noble gasses, diatomic nitrogen and more complicated organic molecules like Isoflurane all produce clinically similar anesthesia in higher animals, with potency well predicted by their partition coefficient in olive oil [97]. This 'generalness' led to efforts to

---

[1]This chapter is in preparation for submission with co-authors Elly Gray, James Sethna and Sarah Veatch. I aided in early experiments in Sarah Veatch's lab, but the bulk of the experimental work was performed by Elly Gray.

explain anesthesia as a biophysical perturbation acting on the membrane itself [58]. Anesthetics were shown to decrease the viscosity of synthetic membranes [11, 88], and to take single-component membranes away from a liquid-gel transition [100], both in a manner that correlated well with their potency as anesthetics. However, these affects tended to be small- in each case, they could be reproduced by raising temperature by less than $1^{o}C$ [46]. Recent work has focused on protein based mechanisms [47] and in particular, on ligand-gated ion channels many of which have been shown to have their conductance changed by anesthetics [48]. Attention has focused on the GABA-A channel in particular, whose sensitivity to the inhibitory neurotransmitter GABA increases dramatically at anesthetic concentration. Although an interpretation of this data in terms of an anesthetic binding site on the GABA-A receptor itself is appealing, such a model suffers from at least two philosophical issues: Why should the GABA-A receptor have a binding site that can accommodate such a diverse set of molecules? Furthermore, why should so many ion channels in so many species have binding sites for these molecules?

Here we present experimental evidence for a model of anesthesia that can explain the observed conductance data *without* the need for a specific anesthetic binding site on the GABA-A receptor. Recent work in diverse areas has suggested that lipid mediated heterogeneity often plays a regulatory role [90]. This ubiquitous 'lipid raft' regulation plays a functional role in many signaling pathways, and GABA-A in particular is thought to be localized and regulated in part by changing its interaction with the local membrane environment [87, 130]. We hypothesize that anesthetics disrupt this regulation, leading to the observed sensitization of receptors to GABA.
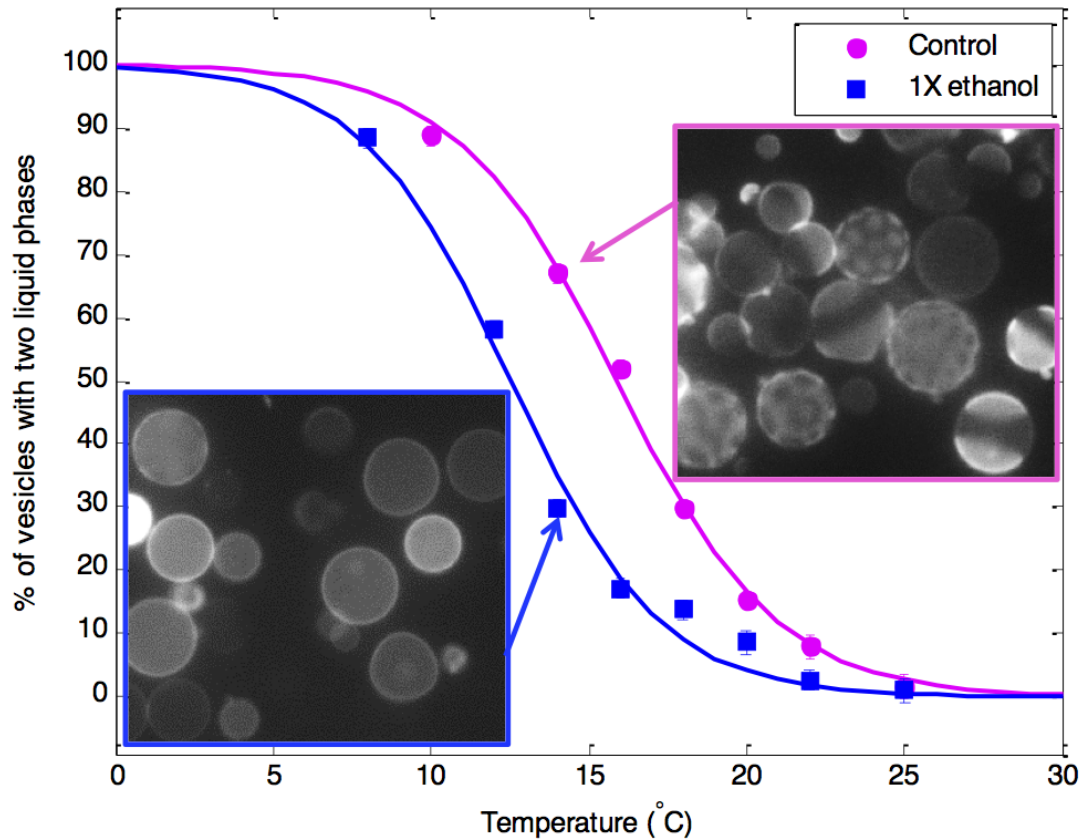
Figure 5.1: Giant Plasma Membrane Vesicles (GPMVs) taken from Rat Basophilic Leukemia (RBL) cells [7, 147] are placed in buffer with varying concentration of anesthetic. The fraction of vesicles that appear phase separated at a fixed temperatures are counted from images taken using optical microscopy. (Counting is 'single blind'-the counter does not know the temperature or anesthetic concentration of the vesicles being observed, but the microscopist does.) The resulting data is fit to a single parameter, the critical temperature. Shown are two curves, a control, and $1x$ ethanol. The insets show two images from control and $1x$ ethanol conditions respectively. At this temperature, most of the ethanol treated vesicles remain uniform, while most of the control vesicles are phase separated.

5.2   Results

To test this we took giant plasma membrane vesicles (GPMVs) from intact rat immune (RBL) cells following [7, 147]. These GPMVs go through a critical point slightly below 37°C into two two-dimensional (2D) liquid phases [147]. In previ-

ous work we argued that proximity to this critical point is thermodynamically necessary for lipid mediated regulation at 10-100nm scales as is often seen in the raft literature [93]. Here we add clinically relevant concentrations of the n-alcohol series of anesthetics to these GPMVs and measure the effect on their transition temperature (see figure 5.1). Our results, presented in figure 5.2, show that these anesthetics have a concentration dependent effect on the transition temperature that is scaled well by their potency, and not by their molar concentration in solution[2]. At ED50, the concentration at which 50% of tadpoles lose their righting reflex, transition temperatures are lowered by approximately 4^oC, much larger than effects seen in previous lipid measurements. Our response is likely larger because our cell-derived blebs are very close to a thermal critical point, a non-generic region of thermodynamic space where the system is very sensitive to perturbations[3] [122].

5.3 Model

In addition to demonstrating that anesthetics lower T_c in cell-derived blebs, we performed computer simulations that we intend to serve as a proof of principle that this change in T_c would be sufficient to lead to the observed changes in conductance. We model highly simplified hypothetical GABA receptors im-

---

[2]It should be stated that, as demonstrated by the Meyer and Overton relationship, if we plotted our results vs. the molar fraction *in the membrane* we might have a similarly good correlation.

[3]Although a 4° shift is much larger than is seen in most lipid based measurements, it is still susceptible to the argument that it is not large enough. In particular, a human with a 4^oC fever is unhappy, but conscious, and cold blooded animals which presumably tolerate much larger temperature variations show similar sensitivities to anesthetic. We note that the model we propose here does not necessarily predict that a change in temperature would mimic this change (unlike a theory where viscosity changes mediate anesthesia). If the protein's two functional states have different entropies, than biology could tune this entropy difference to compensate for temperature changes to the membrane's properties. This compensation would *not* buffer the effects of anesthetics.
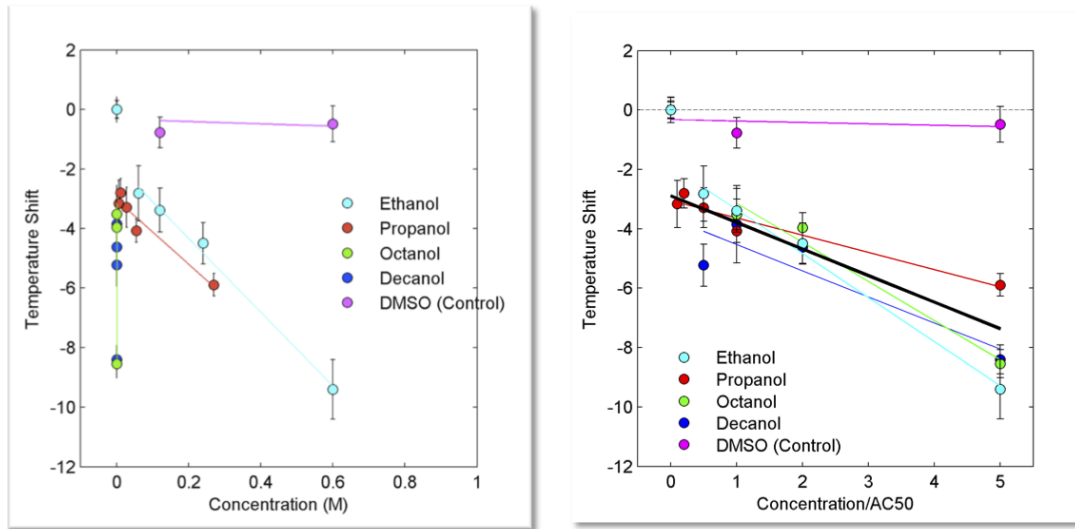
Figure 5.2: The long chain alcohols depress the transition temperature of GP-MVs taken from RBL cells, in a manner that strongly correlates with their potency as an anesthetic. On the left the change in transition temperature is plotted as a function of molar concentration of anesthetic in water, with DMSO, which does not have significant anesthetic effects plotted as a control. On the right, the same curves are plotted but with concentrations given as fractions of their AC50- the concentration at which 50% of tadpoles lose their righting reflex (see Table 1 of [109]). This rescaling approximately collapse the curves of Temperature shift vs. Anesthetic concentration.

mersed in a nearly critical two dimensional fluid (implemented in simulation on a lattice Ising model). Our model proteins prefer to be surrounded entirely by liquid-ordered (or equivalently disordered) membrane phase when not bound by GABA, and they have no preference for the local liquid environment when bound and conducting (see figure 5.3). This hypothetical protein would have an increased sensitivity to a ligand preferring the conducting state if the critical point were lowered at fixed temperature roughly because at higher temperatures the fluid becomes more uniform, favoring the bound state (see section 5.4 for details). As shown in figure 5.4, a protein 11nm in diameter (approximately the size of the GABA-A receptor) would be sufficiently large to recapitulate the observed changes in conductance seen in dose-response curves of the actual

GABA-A receptor (compare to measured curves, for example in [48]).
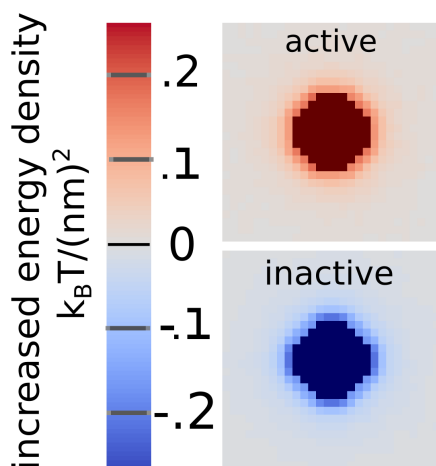
Figure 5.3: In our model a simplified ligand gated ion channel 10nm across can can exist in an agonist bound, conducting state (red) or an unbound non-conducting state (blue). We assume that the conducting state has no preference for its local liquid environment (a free boundary condition) while the non-conducting state has a strong preference for ordered lipids along its boundary. This leads to an increase in the number of ordered and disordered lipids that share boundaries, and a corresponding increase in both the energy density and the local concentration of anesthetic molecules. We map the average value of the resulting energy density around these two boundary conditions. Our model is equivalent to a direct binding model, with anesthetic 'binding sites' distributed amongst the lipids that surround the receptor. A detailed explanation of our model is provided in section 5.4.

Our results suggest an explanation for the generalness of anesthesia. Anesthetic potency is a measurement of how effective a small molecule is at taking the membrane away from its critical point. This change in membrane properties affects the large number of proteins that are regulated by their preference for the local membrane environment. Larger proteins regulated in this manner are likely to be more sensitive to this perturbation, perhaps explaining why GABA-A, a large, multi-subunit protein seems to show the largest effect. Although we don't expect that our boundary conditions accurately describe the
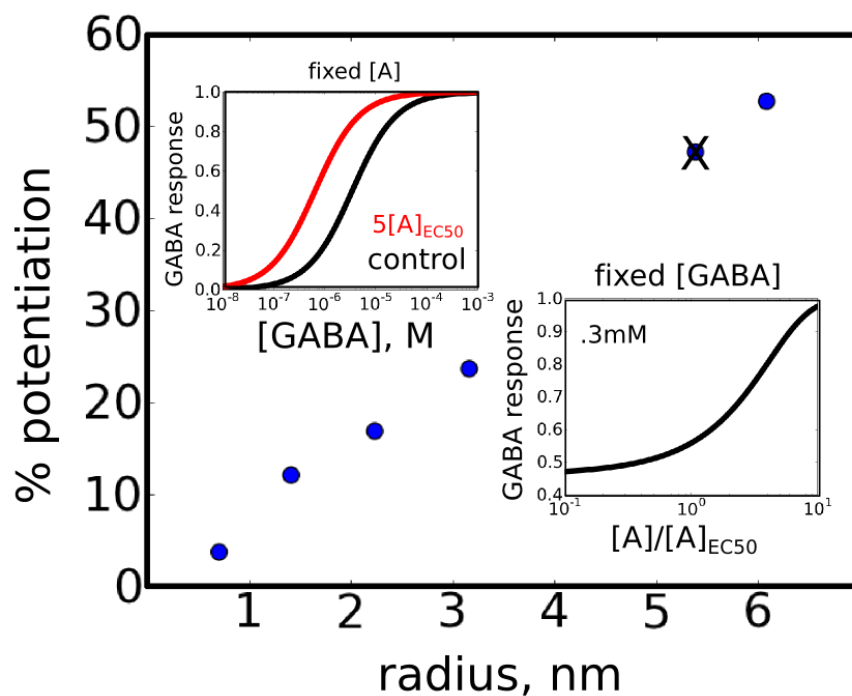
Figure 5.4: Our model predicts that the response of a hypothetical receptor to GABA, as described in figure 5.3 and section 5.4will be potentiated by anesthetic by an amount dependent on its size. A receptor 5.5nm in radius (marked with X, close to the size of the GABA-A receptor) would have its response potentiated by about 50% at anesthetic concentration $[A] = [A]_{EC50}$. For such a receptor with binding affinity for GABA of .35mM (similar to GABA-A's) we plot the response vs GABA concentration at $[A] = 5[A]_{EC50}$ and at $[A] = 0$. Finally, we show how such a receptor would respond to varying concentrations of anesthetic, $[A]$ at fixed $[GABA] = .3$mM. These results are similar to those seen for the GABA-A receptor [48].

GABA-A channel, we do demonstrate that our observed change in T_c are sufficient to lead to the observed changes in channel function in an allosterically modulated hypothetical channel sensitive to its lipid environment.

5.4　Simulation details

We model a hypothetical receptor R which can exist in two states: an active state R_a in which it is bound to a single GABA molecule and an inactive one R_i in which it is not. We allow for these two states to interact differently with the surrounding membrane.

In thermal equilibrium the probability for the *combined* system of the receptor and the surrounding membrane (with state $\{M\}$) to be in a particular state $P(R, \{M\} | [GABA])$ is given by a Boltzmann factor for the combined system:

$$P(R, \{M\} | [GABA]) = \frac{1}{Z([GABA])} e^{-\beta E_0(R, [GABA]) - \beta H_R(\{M\}) - \beta H_M(\{M\})}$$

$$Z([GABA]) = \sum_{R, \{M\}} e^{-\beta E_0(R, [GABA]) - \beta H_R(\{M\}) - \beta H_M(\{M\})}$$

(5.1)

where H_M describes the energy of all of the membrane degrees of freedom that are independent of the receptor's state, H_R describes the energy dependance of the membrane on the state of the receptor R and where $E_0(R)$ describes the dependence of the (free) energy of the receptor configuration on the concentration of GABA, $[GABA]$. Our interest is purely in the (experimentally observable and functionally relevant) activity as a function of $[GABA]$, $P(R||GABA])$, which we can in principle calculate by summing over the membrane's degrees of freedom as follows:

$$P(R|[GABA]) = \sum_{\{M\}} P(R, \{M\} | [GABA])$$

(5.2)

Presuming that an activated receptor always binds a single molecule of GABA we can write the 'bare' free energies of the receptor as $\beta E_o(R_i) = -log(k_d^0)$ and $\beta E_0(R_a) = -\log([GABA])$, allowing us to write:

$$P(R_a) = \frac{1}{Z([GABA])} \sum_{\{M\}} e^{-\beta H_{R_a}(\{M\}) - \beta H_M(\{M\}}$$

$$= \frac{[GABA]e^{-\beta F_a}}{k_d^0 e^{-\beta F_i} + e^{-\beta F_a}[GABA]}$$

$$e^{-\beta F_a} = \sum_{\{M\}} e^{-\beta H_{R_a}(\{M\}) - \beta H_M(\{M\})}$$ (5.3)

$$e^{-\beta F_i} = \sum_{\{M\}} e^{-\beta H_{R_i}(\{M\}) - \beta H_M(\{M\})}$$

Where $F_{i/a}$ is the free energy of the membrane conditioned on the the receptor being in an inactive or active state respectively. This gives a Hill equation for the probability of the receptor being active:

$$P(R_a) = \frac{[GABA]}{[GABA] + k_d}$$

$$k_d = k_d^0 e^{-\beta(F_i - F_a)}$$ (5.4)

We want to observe the dependance of k_d on a perturbation to $H_M(\{M\})$, the piece of the Hamiltonian that does not explicitly couple to the state of the receptor. This corresponds to a change in the response of the receptor to anesthetic that is not directly mediated by binding of anesthetic to receptor. (Direct binding could be modeled as a change to either H_R or $E_0(R, [GABA])$.) Consider making a small change in the Hamiltonian by an amount $\delta H'_M(\{M\})$. This would change the log of k_d by an amount:

$$\frac{\Delta \log(k_d)}{\Delta H'_M} = -\beta \frac{\Delta F_i}{\Delta H'_M} + \beta \frac{\Delta F_a}{\Delta H'_M}$$ (5.5)

If small, this can be expressed as the difference in the expectation value of the change in the hamiltonian averaged over the ensemble of membrane configurations defined by each receptor state:

$$-\beta \frac{\partial F_i}{\partial H'_M} + \beta \frac{\partial F_a}{\partial H'_M} = < H'(\{M\}) >_i - < H'(\{M\}) >_a$$ (5.6)

103

where the expectation values

$$\langle f(\{M\})\rangle_{i/a} = e^{\beta F_{i/a}} \sum_{\{M\}} f(\{M\})e^{-\beta H_{R_{i/a}}(\{M\})-\beta H_M(\{M\})} \tag{5.7}$$

are over the ensemble of membrane configurations defined by the inactive and active form of the receptors.

Our experimental results can be interpreted as measuring H' [4]. We model the membrane as a 2D Ising model with nearest neighbor interactions, and we take H' to be the change in the nearest neighbor coupling that would lead to the observed changes in T_c. We model receptors as blocky spheres like the one shown in figure 5.3 that sit on that square lattice Ising model and with active and inactive forms differing onlyin their boundary conditions. In the active form, there is no energetic coupling between the membrane and receptor (the boundary conditions are 'free'). In the inactive form, the boundary conditions are fixed, so that all lattice sites sharing a bond with the boundary are constrained to be spin up.

We generate ensembles conditioned on these receptors using the Wolff algorithm on 64x64 lattices with bi-periodic boundary conditions. We run our simulation at $1.05T_c$ as motivated by experiments [147]. The Wolff algorithm can implement a fixed boundary condition along a receptor by rejecting an entire cluster whenever a site in contact with the receptor added to it (see chapter 3). For efficiency we buffer this with Heat bath moves near the receptor, where almost all Wolff clusters are rejected. In addition the Wolff algorithm can implement a free boundary condition at the edge of a receptor by rejecting the addition of any spin to a growing cluster that lies within the receptor, while *not*

---

[4]a large family of perturbations change T_c in the Ising model, but here we assume that only the nearest neighbor interaction is changed by the addition of anesthetic.

rejecting the entire cluster. We generate equilibrium ensembles with $100,000$ independent samples for each distribution.

As the simulation proceeds, we keep track of the average energy density $< \rho(x) >_{i/a}$, which is plotted as a heat map in figure 5.3. Since the perturbation arising from anesthetics H' is a nearest neighbor coupling we can relate $\langle \rho(x) \rangle_{i/a} = (T/\Delta T_c) < H'(x) >_{i/a}$ which can be interpreted as proportional to the increased (or decreased) density of 'binding sites' for anesthetic. The output of our simulation is the change in the log of k_d which is given by equations 5.5 and 5.6. This and equation 5.4 are used to generate the plots in figure 5.4, where we have taken $T_c = 300K$, $T = 310$ and $\Delta T_c = 4K[A]/[A]_{EC50}$ throughout.

DIFFERENTIAL GEOMETRY AND COARSENING

Abstract [1] - We reformulate the continuum limit and the renormalization group- two key tools underpinning emergent theories in the hard sciences - to focus on quantifying what information remains available after coarsening. We study the susceptibility of macroscopic observables to changes in parameters of a microscopic model. We find that macroscopic behavior is sensitive to just a few 'stiff' directions in parameter space, and explain emergent simplicity in terms of a broad range of sloppy eigenvalues corresponding to unimportant parameter combinations. Similar models from systems biology and other soft sciences have exhibited a similar enormous range of eigenvalues, perhaps providing a unified information theoretic explanation for why relatively primitive models in both hard and soft sciences can often capture the behavior of complex interacting systems.

6.1   Introduction

What makes Nature comprehensible? In high-energy physics, physical theories form a nested hierarchy. Non-relativistic quantum mechanics emerges as an effective theory for quantum electrodynamics which gives a low energy approximation to the electroweak model, itself a low energy approximation to a GUT. Each theory explains a variety of experiments within a large range of lengths and energies, and each higher-energy, more 'fundamental' theory typically has more symmetry and unity than its descendants. Condensed matter

---

[1]A version of this chapter is being prepared for submission with co-authors Ricky Chachra, Mark Transtrum and James Sethna

physics shares with high-energy physics the hierarchy of broken symmetries, with superconductors inside Fermi liquid theory inside non-relativistic quantum mechanics, but here the descendent theories tend to be more elegant and comprehensible than their complex, microscopic underpinnings – comprehensibility can emerge from complexity. But what about theories of systems biology, economics, and ecology, where the underlying complexity seems irreducible (and yet the behavior is nonetheless fruitfully modeled)?

In both high-energy and condensed-matter physics, the underlying reason for comprehensibility lies in the *independence* of the behavior on the underlying microscopic theory. If solving string theory was necessary for understanding the behavior of mesons, or solving Schrödinger's equation was necessary for understanding magnets or superconductors, comprehensibility would be only of philosophical interest. In high-energy physics, this becomes the principle of renormalizability — each renormalizable theory can stand on its own in the high-energy limit, demanding bigger and bigger accelerators to directly probe for the higher scales. In condensed-matter physics, this is expressed by continuum limits (for behaviors within phases) and by the renormalization group (for behavior at a continuous phase transition) — the long-wavelength, low-energy behavior of a material is largely independent of the microscopic behavior. Fluids composed of a wide variety of molecules all obey the Navier-Stokes equations at scales large and slow compared to the molecules, with only the viscosity and mass density depending on the molecular details. Comprehensibility, at root, lies in this information compression- the complex microscopic properies of these materials only enter into the large and slow properties through their projections onto a few relevant macroscopic observables.

Recent studies of nonlinear multiparameter models – the foundation of systems biology, ecology, climate science, and parts of economics – have shown that they share striking common features. The behavior of a systems biology model with thirty interacting proteins and 48 undetermined reaction rate parameters will depend strongly on only a few linear combinations of its parameters [14]. Seventeen other systems biology models [59, 152], models from mathematics and quantum Monte Carlo variational wavefunctions, and neural network models [140] all share this behavior. The models are all *sloppy*, with a range of stiffnesses (eigenvalues of the covariance matrix) spanning six to twelve orders of magnitude — with only a few directions constrained substantially by the data, and a large space of sloppy directions which would describe the observed behavior equally well. This sloppiness would seem a kind of information compression too, without the elegant emergent theory: most of the microscopic details are unimportant to understanding the collective behavior. Indeed, one can argue that none of these multiparameter models are 'correct' — yet their predicted behaviors can be robust to changes in the details of our understanding of the underlying microscopic rules. Sloppiness may at root explain why one can predictively model complicated systems in biology (or economics, or climate) long before the parameters and even all the underlying components are discovered.

In this chapter, we will quantitatively tie our understanding of the comprehensibility of our physical world to the fuzzier comprehensibility of the softer sciences. We will adapt our analytical tools developed to study sloppiness in multiparameter models to study the emergence of simple physical laws from complex underpinnings. We shall treat both a prototypical continuum limit (the diffusion equation) and a continuous phase transition (the Ising model),

and will show that, on long length scales, the emergence of simple laws can be traced precisely to the formation of a hierarchy of stiff (macroscopic, important) and sloppy (microscopic, irrelevant) degrees of freedom. In each case we quantify the information that is preserved or lost from observables viewed at progressively coarser scales. By calculating the susceptibility of these macroscopic observables to changes in microscopic parameters, we find that a similar sloppy spectrum emerges as information about the microscopic parameters is anisotropically discarded. This gives an information theoretic explanation for the success of simple models in the hard physical sciences: coarse-grained behaviors of these systems depend only on a few parameter combinations in a microscopic model. The similarity between this emergent spectrum and the ones seen in diverse models from the soft sciences suggests that a similar philosophy underlies the success of models there- apparent model complexity is often reduced to just a few relevant macroscopic observables.

In section 6.2 we provide an overview of the information theoretic tools that we use to quantify distinguishability. In section 6.3 we apply this formalism to a model of stochastic motion from which the diffusion equation emerges, and in sections 6.4 to 6.7 we apply it to the Ising model.

6.2   Information geometry and the Fisher metric

How different are two probability distributions, $P_1(x)$ and $P_2(x)$? What is the correct measure of distance between them? To answer this question, imagine being given a sequence of *independent* data points $\{x_1, x_2, ...x_N\}$, with the task of inferring which of the two models would be more likely to generate the data.

As probabilities multiply, the probability that P_1 generated the data is given by:

$$\prod_i P_1(x_i) = \exp\left(\sum_i \log P_1(x_i)\right) \tag{6.1}$$

and by calculating this for each of the two distributions, which could see which model would be more likely to have produced the observed data.

How difficult should one expect this task to be? Presuming N to be large we can estimate the probability that a typical string generated by P_1 would be produced by P_1. To do this we simply take a product similar to that in equation 6.1 but with each state x entering into the product $NP_1(x)$ times:

$$\prod_x P_1(x)^{NP_1(x)} = \exp\left(N \sum_x P_1(x) \log P_1(x)\right)$$
$$= \exp(-NS_1) \tag{6.2}$$

where we note that this gives an alternative definition of the familiar entropy S_1 of P_1 (in nats). We can also ask how likely P_2 is to produce a typical ensemble generated by P_1. This is just given by:

$$\prod_x P_2(x)^{NP_1(x)} = \exp\left(N \sum_x P_1(x) \log P_2(x)\right) \tag{6.3}$$

We can ask how much *more* likely a typical ensemble from P_1 is to have come from P_1 rather than from P_2. This is given by:

$$\prod_x (P_1(x)/P_2(x))^{NP_1(x)}$$
$$= \exp\left(N \sum_x P_1(x) \log\left(\frac{P_1(x)}{P_2(x)}\right)\right) \tag{6.4}$$
$$= \exp\left(-ND_{KL}(P_1\|P_2)\right)$$

This defines the Kullback-Liebler Divergence, *the* statistical measure of how

different two probability distributions are [25]:

$$D_{KL}(P_1\|P_2) = \sum_x P_1(x) \log\left(\frac{P_1(x)}{P_2(x)}\right) \tag{6.5}$$

This measure has several properties that prevent it from being a proper mathematical distance measure, most obviously that it does not necessarily satisfy $D_{KL}(P_1\|P_2) = D_{KL}(P_2\|P_1)^2$. However, for two 'close-by' models D_{KL} does become symmetric. Consider a continuously parameterized set of models P_θ where θ is a set of N parameters θ^μ. The infinitesimal Kullback-Liebler divergence between models P_θ and $P_{\theta+\Delta\theta}$ can be shown to take the form [3]:

$$D_{KL}(P_\theta, P_{\theta+\Delta\theta}) = g_{\mu\nu}\Delta\theta^\mu\Delta\theta^\nu + O\Delta\theta^3 \tag{6.6}$$

where $g_{\mu\nu}$ is the Fisher Information, given by:

$$g_{\mu\nu}(P_\theta) = -\sum_x P_\theta(x) \frac{\partial}{\partial\theta^\mu} \frac{\partial}{\partial\theta^\nu} \log P_\theta(x) \tag{6.7}$$

The quadratic form of the KL-divergence at short distances motivates using the Fisher Information as a metric on parameter space. This defines a Riemannian manifold where each point on the manifold specifies a probability distribution. The tensor $g_{\mu\nu}$ can be shown to have all of the necessary requirements to be a metric- it is symmetric (derivatives commute) and positive semi-definite (intuitively because no model can fit any model better than that model fits itself). It also has the correct transformation laws under a reparameterization of P. Distance on this manifold is (at least locally) a measure of how distinguishable two models are from their data, in dimensionless units of standard deviations. This

---

[2]A distance measure should also satisfy some sort of generalized triangle inequality- at the very least $D(A, B) + D(B, C) \geq D(A, C)$ which is not necessarily satisfied here.

[3]It is an interesting exercise to show that there is no term linear in $\Delta\theta$. The crucial step uses that P_θ is a probability distributions so that $\partial_\mu \sum_x P_\theta(x) = 0$. The result, though intuitive, is not completely trivial. It means that the model most likely to reproduce typical data from any given model is that model itself.

already gives one important difference between information geometry and the more familiar use of Riemannian geometry in General Relativity. In GR distances are dimensionful, measured in meters. While certain functions of the manifold (notably the Scalar curvature) are dimensionless and can appear in interesting ways on their own, a distance is only large or small when compared to some other distance. In information geometry, by contrast, distances have an intrinsic meaning- Probability distributions are distinguishable from a typical measurement provided the distance between them is greater than one. Below we consider two special cases.

6.2.1 The metric of a Gaussian model

First, motivated by non-linear least squares we consider a model whose output is a vector of data, y_i (for $1 < i < M$). Taking the data to be normally distributed with width σ^i (so that the 'cost' or sum of squared residuals is proportional to the log of the probability of the model having produced the data) around a parameter dependent value, $\vec{y}_0(\theta)$ we can write the probability distribution of data y given a set of parameters θ as:

$$P_\theta(\vec{y}) \sim \exp\left(-\sum_i (y^i - y_0^i(\theta))^2/2\sigma^{i2}\right) \tag{6.8}$$

Defining the Jacobian between parameters and scaled data as:

$$J_{i\mu} = \frac{\partial}{\partial\theta^\mu} \frac{y_0^i(\theta)}{\sigma^i} \tag{6.9}$$

The Fisher information for least squares problems is simply given by [4] [139, 140]:

$$g_{\mu\nu} = \sum_i J_{i\mu} J_{i\nu} \tag{6.10}$$

---

[4] This assumes that the uncertainty σ^i does not depend on the parameters, and that errors are diagonal. Both of these assumptions seem reasonable for a wide class of models, for example if measurement error dominates.

This particular metric has a geometric interpretation: distance is locally the same as that measured by embedding the model in the space of scaled data according to the mapping $y_0(\theta)$ (it is *induced* by the Euclidian metric in data space). It is exactly this metric that was shown to be sloppy in seventeen models from the system's biology literature [59, 139, 140]

6.2.2   The metric of a Stat-Mech Model

Second, we consider the case of an exponential model, familiar from statistical mechanics, defined by a parameter dependent Hamiltonian that assigns an energy to every possible configuration, x, and a temperature (which we will set to 1). Each parameter θ^μ controls the relative weighting of some function of the configuration, $\Phi_\mu(x)$, which together define the probability distribution on configurations through[5]:

$$P(x|\theta) = \exp(-H_\theta(x))/Z$$
$$Z(\theta) = \exp(-F(\theta)) = \sum_x \exp(-H_\theta(x)) \tag{6.11}$$
$$H_\theta(x) = \sum_\mu \theta^\mu \Phi_\mu(x)$$

Putting the Hamiltonian into this form is a coordinate choice, at least locally and it is chosen for convenience in calculating the metric, which is written [26, 113] [6].

---

[5]Though perhaps unfamiliar, typical models can be put into this form. For example, the 2D Ising model of section 6.4 has spins $S_{i,j} = \pm 1$ on a square LxL lattice with the configuration $x = \{s_{i,j}\}$ being the state of all spins. The magnetic field, θ^h multiplies $\Phi_h(x) = \sum_{i,j} s_{ij}$, and the nearest neighbor coupling multiplies $\Phi_{01}(x) + \Phi_{10}(x) = \sum_{i,j} s_{i,j}s_{i+1,j} + s_{i,j}s_{i,j+1}$

[6]Several seemingly reasonable metrics can be defined for systems in statistical mechanics and all give similar results in most circumstances [113]. Most differences occur either for systems not in a true thermodynamic (N large) limit, or for systems near a critical point. As far as we are aware, Crooks [26] was the first to stress that the one used here can be derived from information theoretic principles, perhaps making it the most 'natural' choice. In [26] Crooks showed that when using this metric 'length' has an interesting connection to dissipation by way

$$g_{\mu\nu} = \left\langle -\partial_\mu \partial_\nu \log(P(x)) \right\rangle$$

$$= \partial_\mu \partial_\nu \left\langle H(x) \right\rangle + \partial_\mu \partial_\nu \log(z) \tag{6.12}$$

$$= \partial_\mu \partial_\nu \log(z) = -\partial_\mu \partial_\nu F$$

It might be noted that the last line does *not* transform like a metric under general reparameterizations. We have taken advantage of the fact that the Hamiltonian is linear in parameters θ^μ.

6.3   A Continuum Limit: Diffusion

With these definitions in hand, we turn to a specific problem where information about microscopic details is lost in a coarse-grained description. A prototypical example of such a continuum limit is the emergence of the diffusion equation in a system consisting of small particles undergoing stochastic motion. Diffusion effectively describes the motion of a particle provided that there is translation invariance in time and space. Microscopic parameters that describe details of the medium in which the particle is diffusing and the molecular details of such an object enter into this continuum description only through their effects on the diffusion constant, or, if it is present, the rate of drift. Furthermore, knowing molecular details (for example the bond angle of a water molecule in the medium through which a particle is diffusing) that might enter into a microscopic description of the motion would be extremely unhelpful in predicting a particle's diffusion constant.

To see how this comes about we consider a 'microscopic' model of stochastic motion on a discrete lattice of sites j. Our model is defined by $2N + 1$ parameters

of the Jarzynski equality [75].

114

θ^μ, for $-N \le \mu \le N$ which describe the probability that in a discrete time step a particle will hop from site j to site $j + \mu$. We presume that we start our particles from a distribution $\rho_0(j)$, and that our measurement data consists of the number of particles at some later time t, $\rho_t(j)$.

We first consider taking 'microscopic' measurements of our model parameters, by starting with an initial probability distribution $\rho_0(j) = \delta_{j,0}$, and observing the distribution after one time step, $\rho_1(j)$. This distribution is just given by:

$$\rho_1(j) = \theta^j \tag{6.13}$$

Presuming our measurement uncertainty is Gaussian, with width $\sigma_{mess} = 1$ [7] we can calculate the Fisher metric on the parameter space using the Least Squares metric defined in equations 6.9 and 6.10:

$$\begin{aligned} J_{i,\mu} = \partial_\mu \rho_1(i) &= \delta_{i,\mu} \\ g_{\mu\nu} = \sum_i J_{i,\mu} J_{i,\nu} & \\ &= \delta_{\mu\nu} \end{aligned} \tag{6.14}$$

This metric has $2N + 1$ eigenvalues each with value $\lambda = 1$. All of the parameters in this model are measurable with equal accuracy. Additionally, if we wanted to understand the behavior at this microscopic level, there is no reason to think that a reduced description of the model should be possible; each direction in parameter space is equally important in determining the one step evolution from the origin.

We consider two ways of coarsening our data. Firstly, we could imagine that our measurement apparatus has some uncertainty in locating the starting and

---

[7]We could carry out a more complicated calculation assuming our uncertainty comes from the stochastic nature of the model itself, but presuming we start with many particles, this approach would yield similar but less transparent results. Changing the measurement uncertainty from 1 to σ_{meas} will multiply all calculated metrics by a trivial factor of $1/\sigma_{meas}^2$ and is omitted for clarity.

ending positions of the particles, and secondly, we could imagine that we are unable to make instantaneous observations and are restricted to a measurement at time $t_m > 1$.

6.3.1 Coarsening the diffusion equation by blurring in space

The first case can be treated by starting with an initial distribution that is gaussian with width σ_{obs}, given by [8]:

$$\rho_0(j) \propto \frac{1}{\sigma_{obs}} \exp(-j^2/2\sigma_{obs}^2) \tag{6.15}$$

After a single time step, the density of particles is given by:

$$\rho_1(j) \propto \frac{1}{\sigma_{obs}} \sum_{\mu=-N}^{N} \exp(-(j-\mu)^2/2\sigma_{obs}^2)\theta^\mu \tag{6.16}$$

The Jacobian and metric are given by:

$$J_{j,\mu} \propto \frac{1}{\sigma_{obs}} \exp(-(j-\mu)^2/2\sigma_{obs}^2)$$
$$g_{\mu\nu} \sim \frac{1}{\sigma_{obs}^2} \sum_i \exp(-((j-\mu)^2 + (j-\nu)^2)/2\sigma_{obs}^2) \tag{6.17}$$
$$\sim \frac{1}{\sigma_{obs}} \exp(-(\mu-\nu)^2/4\sigma_{obs}^2)$$

Notice that in our model the parameter N plays the role of the molecular scale, while σ_{obs} plays the role of the observation scale. For a typical measurement of diffusion in (say) water, the molecular scale, N is in angstroms, while

---

[8]This is exactly equivalent to starting from a delta-function distribution but stochastically observing a particle at a position $j_{observed}$ with a probability given by the same gaussian centered on its actual position j_{actual}

the observation scale is set by the wavelength of light, $\sim 400nm$, so that our interest lies in the limit where $\sigma_{obs} >> N$. In this limit, we can expand the matrix in powers of N/σ_{obs}. To leading order we have:

$$g_{\mu\nu} \approx N/\sigma_{obs} \tag{6.18}$$

This has a single non-zero eigenvector, $v_0^\mu = 1/(2N+1)$, with eigenvalue $\sim N/\sigma_{obs}$. We can interpret this as measuring the non-conservation of particle number, which is least blurred by our coarsening, and which is often constrained to be zero by conservation of particle number[9]. To order $1/\sigma_{obs}^2$ we get:

$$g_{\mu\nu} \approx N/\sigma_{obs}(1 - ((\mu - \nu)/4\sigma_{obs})^2) \tag{6.19}$$

This matrix has one new non-zero eigenvalue with eigenvector $v_1^\mu \sim \mu$ whose eigenvalue is given by $\lambda_1 \sim (N/\sigma_{obs})^3$. This measures the drift, and it is indeed dominant over diffusion in systems where it is not constrained by a spatial symmetry to be zero (for example for a particle falling through a liquid under the influence of gravity, where it might be reasonable to neglect diffusion entirely in an effective model).

To the next order we get

$$g_{\mu\nu} \approx 1/\sigma_{obs}(1 - ((\mu - \nu)/2\sigma_{obs})^2 + ((\mu - \nu)/2\sigma_{obs})^4/2!) \tag{6.20}$$

which contributes another eigenvector, given approximately by $v_2^\mu \sim \mu^2 - N^2/3!$ and eigenvalue $\lambda_2 \sim (N/\sigma_{obs})^5$. This eigenvector measures changes in the diffusion constant, which is the dominant parameter in a model for a system in which particle number is conserved and in which the system obeys the symmetry of spatial inversion.

---

[9]Intuition might state that non-conservation of particle number would not decay at all. However our noise comes from measurement error in the individual lattice sites, and this does indeed become larger with distance.

Further terms measure higher order cumulants of the final distribution, and have eigenvectors that approach the Hermite polynomials in a suitable continuum limit. The eigenvalues scale like $\lambda_n \sim (N/\sigma_{obs})^{2n+1}$. These terms never appear in a continuum description, because they are always harder to observe than the diffusion constant by a factor of the ratio of the observation scale to the diffusion constant raised to a large power [10]. It is also worth noting that careful observation of a particular θ^μ, somewhat analogous to knowing the bond-angle of a water molecule, would give very little insight on the relevant observables.

6.3.2 Coarsening the diffusion equation by observing at long times

The molecular timescale is also typically much faster than the typical timescale of a measurement. We can also ask how our ability to measure microscopic parameters changes with experiment time. This question seems in some ways more natural- while blurring in space is an experimental limitation, the mapping from short time parameters onto late time observables is certainly a property of the system that is independent of experimental limitations.

To calculate the density of particles at position j and time t, $\rho_t(j)$, it is useful to introduce the Fourier transform of the hopping rates, as well as the Fourier

---

[10]It is not possible for the diffusion constant, as defined here to be 0 while any higher cumulants are non-zero, explaining why though drift and the diffusion constant both appear in continuum limits, the physical parameter that describes the third cumulant of a typical random does not. The third parameter does measure the Skew of the resulting density distribution, the next one measures the distribution's Kurtosis, and further parameters do not even have names
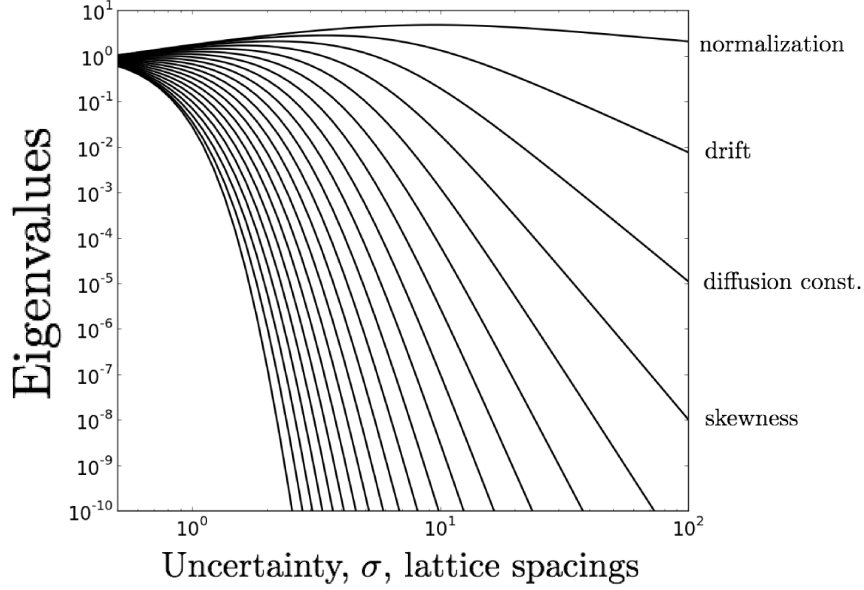
Figure 6.1: The metric's eigenvalues are plotted for a 21 dimensional model ($N = 10$) as the uncertainty, σ, is varied, as described in the text. When the uncertainty is comparable to the lattice spacing all parameters can be inferred with similar accuracy. However, as the uncertainty grows the system develops a typical sloppy spectrum, as in figure 1.3. The largest eigenvalue's eigenvector roughly measures non-conservation of particle number, the next one measures the drift, and the third one measures the diffusion constant.

transform of the particle density at time t

$$\tilde{\theta}^k = \sum_{\mu=-N}^{N} e^{-ik\mu}\theta^{\mu}$$

$$\tilde{\rho}_t^k = \sum_{j=-\infty}^{\infty} e^{-ikj}\rho_t(j) \tag{6.21}$$

$$\rho_t(j) = \frac{1}{2\pi}\int_{-\pi}^{\pi} dk e^{ikj}\tilde{\rho}_t^k$$

In a time step the density distribution is convoluted by the hopping rates. In

Fourier space this is simply written as:

$$\tilde{\rho}_t^k = \tilde{\theta}^k \tilde{\rho}_{t-1}^k \tag{6.22}$$

119

We choose initial conditions with all particles at the origin $\rho_0(j) = \delta_{j,0}$, then:

$$\tilde{\rho}_t^k = (\tilde{\theta}^k)^t$$

$$\rho_t(j) = \frac{1}{2\pi} \int\limits_{-\pi}^{\pi} dk\, e^{ikj}(\tilde{\theta}^k)^t \tag{6.23}$$

The Jacobian and metric at time t can now be written:

$$J_{j\mu}^t = \partial_\mu \rho_t(j) = \frac{t}{2\pi} \int\limits_{-\pi}^{\pi} dk\, e^{ik(j-\mu)}(\tilde{\theta}^k)^{t-1}$$

$$g_{\mu\nu}^t = \frac{t^2}{2\pi} \int\limits_{-\pi}^{\pi} dk\, e^{ik(\mu-\nu)}(\theta^k)^{t-1}(\tilde{\theta}^{-k})^{t-1} \tag{6.24}$$

The metric now depends on the θ themselves. Presuming the (positive) hopping rates θ^μ values sum to 1 with at least two non-zero, then all of the θ values are less than one and the late time behavior of $g_{\mu\nu}^t$ is dominated by small k values appearing in the integrand (equation 6.24). At small values of k:

$$\tilde{\theta}^k = 1 - ik\Delta - \frac{k^2}{2}\Sigma + O(k^3)$$

$$= \exp(-ik\Delta - D\frac{k^2}{2}) + O(k^3)$$

$$\Delta = \sum_\mu \mu\theta^\mu \tag{6.25}$$

$$\Sigma = \sum_\mu^2 \theta^\mu$$

$$D = \Sigma - \Delta^2$$

where in going from the first line to the second we note these two equations are the same to second order in k. Note that Δ is the drift and D is the diffusion constant. From this approximation we can estimate $g_{\mu\nu}^t$:

$$g_{\mu\nu}^t \approx \frac{t^2}{2\pi} \int\limits_{-\infty}^{\infty} dk\, e^{ik(\mu-\nu)} e^{-(t-1)Dk^2} \tag{6.26}$$

We can expand this in powers of the small parameter $k(\mu - \nu)$. This gives

$$g_{\mu\nu}^t \approx \frac{t^2}{2\pi} \sum_{n=0}^{\infty} (\mu - \nu)^{2n} \frac{(-1)^n}{2n!} \int\limits_{-\infty}^{\infty} dk\, (k)^{2n} e^{-(t-1)Dk^2} \tag{6.27}$$

This separates into exactly the same eigenvectors as in the previous case, but the eigenvalues are different. Here they scale like:

$$\lambda_n \sim t^2 \left(\frac{Dt}{N}\right)^{-n-1/2} \quad n \geq 0 \tag{6.28}$$
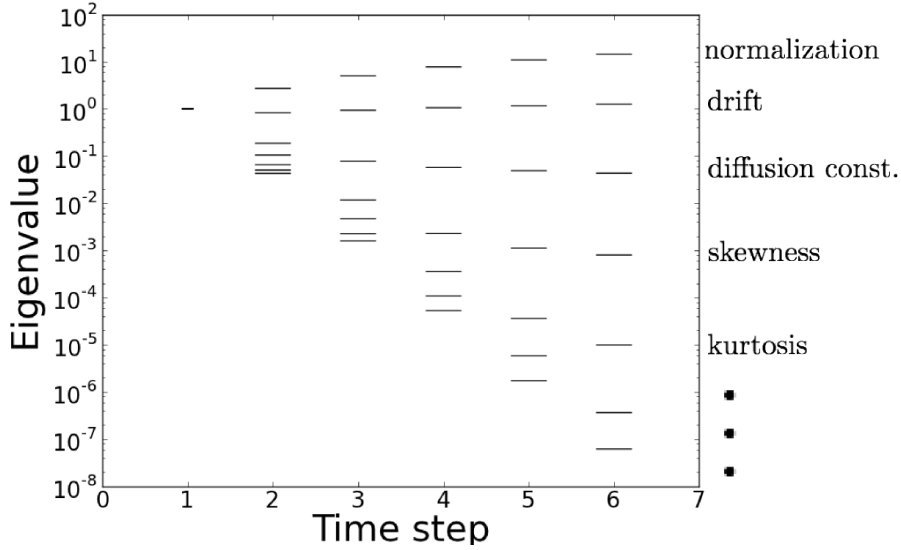
Figure 6.2: The exact metric's eigenvalues are plotted for a 7 dimensional model of diffusion ($N = 3$ as described in the text) with all parameters $\theta^\mu = 1/7$ for measurements after a certain number of discrete time steps. After a single time step, all parameters can be measured with equal accuracy. However, after multiple time steps, as with temporal blurring, a hierarchy develops. The largest eigenvalue, corresponding to non-conservation of probability becomes substantially easier to measure with time, with its eigenvalue growing like $t^{3/2}$. The drift becomes easier to measure, though with its power growing like $t^{1/2}$. The diffusion constant becomes slightly harder to measure with eigenvalue proportional to $t^{-1/2}$. At long times, as in the models shown in figure 1.3, the Fisher Information develops a very sloppy spectrum.

Dt plays a similar role to the one σ^2_{obs} played when we blurred spatially. Just as σ_{obs} can be thought of as setting the length scale associated with observations, $\sqrt{Dt}$ is the scale set by the distance a particle will diffuse in the time it takes to make a measurement. An extra factor of t^2 reflects that a changed parameter has t chances to influence the final distribution. For example, longer times would make it much easier to see if particle number is not conserved. In figure 6.2 the exact metric's Eigenvlaues are shown after multiple time steps for a 7 dimensional model ($N = 3$) for uniform hopping parameters $\theta^\mu = 1/7$. A sloppy spectrum is clearly developing as time proceeds.

6.4   A critical point: The Ising model

The success of the continuum limit might be said to rest on the 'boringness' of the large-scale behavior. All of the fluctuations in the system are essentially averaged at the scale of typical observations. This fails to be true near critical points of systems, where fluctuations remain large up to a characteristic scale ξ which diverges at the critical point itself. Perhaps surprisingly, even at these points these systems have behavior that is universal. The Ising model, for example, provides a quantitative description of both Ferromagnetic and liquid-gas critical points, describing all of the statistics of the observable fluctuations of both systems, even though they have entirely different microscopic components. Just as in diffusion, the observed behavior at these points can then be described by just a few 'relevant' parameters (two in the Ising model; the bond strength and the magnetic field).

The Ising model discussed here takes place on a square lattice (with lattice sites $1 < i, j < L$), with degrees of freedom $s_{i,j}$ taking the values of ± 1. The probability of observing a particular configuration on the whole lattice (denoted by $\{s_{i,j}\}$) is defined by a Hamiltonian ($H\{s_{i,j}\}$) that assigns each configuration of spins an energy (see equation 6.11).

The usual nearest neighbor Ising Model has two parameters: a coupling strength (J), and a magnetic field (h) through the equation:

$$H(\{s_{i,j}\}) = J \sum_{i,j} s_{ij}s_{ij+1} + s_{ij}s_{i+1j} + h \sum_{i,j} s_{ij} \tag{6.29}$$

Here we consider a larger dimensional space of possible models, by including in our Hamiltonian the magnetic field (θ^h), the usual nearest neighbor coupling term, and 12 'nearby' couplings parameterized by $\theta^{\alpha\beta}$ (see figure 6.3). We addi-

tionally allow the vertical and horizontal couplings to be different. In the form

of equation 6.11:

$$H(x) = \sum_{\alpha,\beta} \theta^{\alpha\beta} \Phi_{\alpha\beta}\left(\left\{s_{i,j}\right\}\right) + \theta^h \Phi_h\left(\left\{s_{i,j}\right\}\right)$$

$$\Phi_{\alpha\beta}\left(\left\{s_{i,j}\right\}\right) = \sum_{i,j} s_{ij} s_{i+\alpha,j+\beta} \qquad (6.30)$$

$$\Phi_h\left(\left\{s_{i,j}\right\}\right) = \sum_{i,j} s_{ij}$$

We calculate the metric along the line through parameter space that describes

the usual Ising model (where $\theta^{01} = \theta^{10} = J$ and $\theta^{\alpha\beta} = 0$ otherwise) in zero mag-

netic field ($\theta^h = 0$).
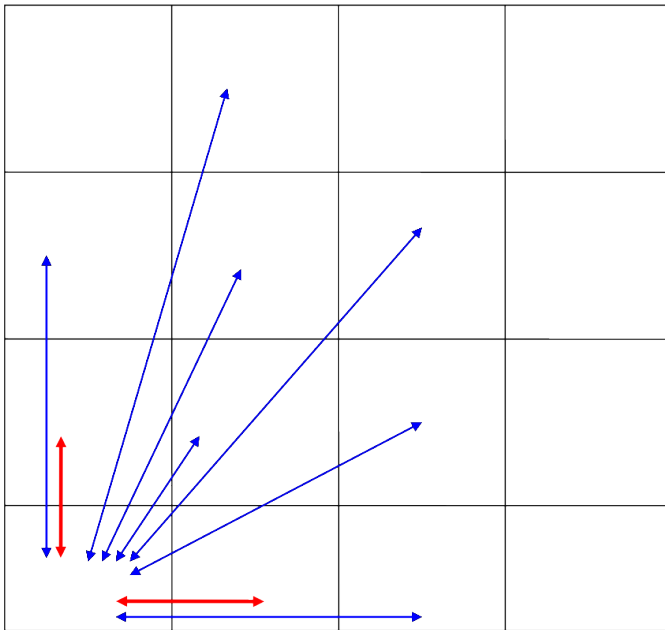
Figure 6.3: We consider a square lattice Ising model, with a magnetic field, and 12 'nearby' neighbor couplings (blue and red) which extend the usual nearest neighbor couplings (red only). We always calculate the metric in this higher dimensional space of possible parameters along the line defined by the usual nearest neighbor Ising Hamiltonian in zero magnetic field.

6.5 Measuring the Ising metric

Using equation 6.12 we can rewrite the metric in terms of expectation values of observables (where except when necessary we condense the indexes $\alpha\beta$ and h into a single μ).

$$g_{\mu\nu} = \partial_\mu \partial_\nu \log z = \left\langle \Phi_\mu \Phi_\nu \right\rangle - \left\langle \Phi_\mu \right\rangle \left\langle \Phi_\nu \right\rangle \tag{6.31}$$

Furthermore, given a configuration $x = \{s_{i,j}\}$ we can readily calculate $\Phi_\mu(x)$, which is just a particular two point correlation function (or the total sum of spins for Φ_h) [11].

To estimate the distribution defined in equation 6.31 we used the Wolff algorithm to very efficiently generate an ensemble of configurations $x_p = \{s_{i,j}\}_p$, for $1 < p < M$ for systems with $L = 64$. We also exactly enumerated all possible states on lattices up to $L = 4$ lattices to compare with our Monte-Carlo results.

With our ensemble of M lattice configurations, x_i we simply measure:

$$g_{\mu\nu} = \frac{1}{M^2 - M} \sum_{p,q=1, p\neq q}^{M} \Phi_\mu(x_p)\Phi_\nu(x_p) - \Phi_\mu(x_q)\Phi_\nu(x_p) \tag{6.32}$$

The results are plotted in figure 6.4. Away from the critical point in the high temperature phase (small βJ) the results seem somewhat analogous to those we found for the diffusion equation viewed at its microscopic scale. All of the parameters that control two spin couplings ($\theta^{\alpha\beta}$) are roughly as distinguishable as each other, with θ^h having different units. However, as the critical point is approached, the system becomes extremely sensitive both to θ^h and to a certain combination of the $\theta^{\alpha\beta}$ parameters. This divergence has been previously shown

---

[11] $\Phi_h\left(\{s_{i,j}\}\right) = \sum_{i,j} s_{i,j}$ is very simple and efficient to calculate for a given configuration $\{s_{i,j}\}$. $\Phi_{\alpha\beta}\left(\{s_{i,j}\}\right)$ is only slightly harder. One defines the translated lattice $s'_{i,j}(\alpha,\beta) = s_{i+\alpha,j+\beta}$, in terms of which we write $\Phi_{\alpha\beta}\left(\{s_{i,j}\}\right) = \sum_{i,j} s_{i,j} s'_{i,j}(\alpha,\beta)$.
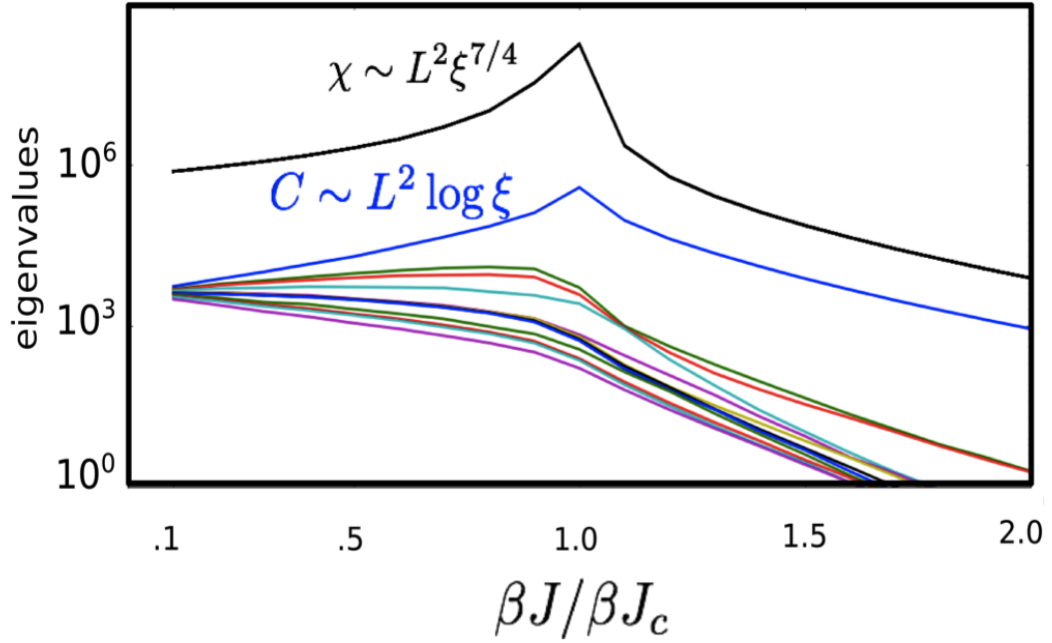
Figure 6.4: The eigenvalues of the metric for the enlarged 13 parameter Ising model described in the text is plotted along the line defined by the usual Ising model with βJ as the only parameter, and $h = 0$. Two parameter combinations become large near the critical point, each diverging with characteristic exponents describing the divergence of the susceptibility and specific heat respectively. The other eigenvalues vary smoothly as the critical point is crossed, and furthermore they have a characteristic scale and are neither evenly spaced nor widely distributed in log.

for the Ising model [113]. In fact, as we will see in the next section, these two metric eigenvalues diverge with the scaling of the susceptibility ($\chi \sim \xi^{7/4}$, whose eigenvector is simply θ^h) and specific heat ($C \sim \log(\xi)$, whose eigenvector is a combination of $\theta^{\alpha\beta}$ proportional to the gradient of the critical temperature, $\frac{\partial T_c}{\partial \theta^{\alpha\beta}}$), respectively. From an information theoretic point of view, these two parameter combinations seem to become particularly easy to measure near the critical point because the system's behavior becomes extremely sensitive to them. The behavior of these two eigenvalues seems to have no parallel in the diffusion equation viewed at its microscopic scale.

6.5.1 Scaling analysis of the Eigenvalue spectrum

To understand our Monte Carlo results for the eigenvalues of the metric, we apply a more standard renormalization group analysis to our calculation. To do this it is useful to use the form $g_{\mu\nu} = -\partial_\mu\partial_\nu F$, and in particular we focus on the critical region, close to the renormalization group fixed point θ_0. After a renormalization group transformation that reduces lengths by a factor of b the remaining degrees of freedom are described by an effective theory with parameters θ' related to the original ones by the relationship $\theta'^\mu - \theta_0^\mu = T_\nu^\mu(\theta^\nu - \theta_0^\nu)$ [12] where T has left eigenvectors and eigenvalues given by $\mathbf{e}_{\alpha,\mu}^L$ and b^{y_α}. It is convenient to switch to the so-called scaling variables, $u_\alpha = \sum_\mu \mathbf{e}_{\alpha,\mu}^L\theta^\mu$, which have the property that under a renormalization group transformation

$$u'_\alpha = b^{y_\alpha}u_\alpha \tag{6.33}$$

It is also convenient to divide our free energy into a singular piece and an analytic piece, so that:

$$F(\theta) = Af^s(u_\alpha(\theta)) + Af^a(u_\alpha(\theta))$$
$$f^s = u_1^{d/2y_1}\mathcal{U}(r_0, ..., r_\alpha) \tag{6.34}$$
$$r_\alpha = u_\alpha/u_1^{y_\alpha/y_1}$$

where fs are free energy densities, A is the system size and where f^a and $\mathcal{U}$ are both analytic functions of their arguments. Notice that by construction the rs do not transform under an RG transformation. The Fisher Information can be

---

[12]$\theta'^\mu - \theta_0^\mu = T_\nu^\mu(\theta^\nu - \theta_0^\nu)$ is strictly true only if the parameters span the space of possible Ising Hamiltonians, but our analysis holds for $g_{\mu\nu}$ on the space of the original parameters provided the θ' span all possible models, which we can assume in this analysis. Said differently, there is no need for T to be square, and it is sufficient for the analysis presented above to assume that T is 13 by infinite dimensional.

similarly divided into two parts, yielding:

$$g_{\mu\nu} = g^s_{\mu\nu} + g^a_{\mu\nu} = -A\partial_\mu\partial_\nu f^s - A\partial_\mu\partial_\nu f^a$$

$$g^s_{\mu\nu} = A \sum_{\alpha,\beta} \left(\frac{\partial u_\alpha}{\partial\theta^\mu}\frac{\partial u_\beta}{\partial\theta^\nu}\right) u_1^{(y_\alpha+y_\beta-d)/y_1} \frac{\partial}{\partial r^\alpha}\frac{\partial}{\partial r^\beta}\mathcal{U}$$

$$= A \sum_{\alpha,\beta}\left(\frac{\partial u_\alpha}{\partial\theta^\mu}\frac{\partial u_\beta}{\partial\theta^\nu}\right)\mathcal{M}^s_{\alpha\beta}(u)\xi^{y_\alpha+y_\beta-d} \qquad (6.35)$$

$$g^a_{\mu\nu} = A \sum_{\alpha,\beta}\frac{\partial u_\alpha}{\partial\theta^\mu}\frac{\partial u_\beta}{\partial\theta^\nu}\frac{\partial}{\partial u_\alpha}\frac{\partial}{\partial u_\beta}f^a$$

$$= A \sum_{\alpha,\beta}\left(\frac{\partial u_\alpha}{\partial\theta^\mu}\frac{\partial u_\beta}{\partial\theta^\nu}\right)\mathcal{M}^a_{\alpha\beta}(u)$$

where ξ is the correlation length, which diverges like $u_1^{-y_1}$. Both $\sum_{\alpha,\beta}\left(\frac{\partial u_\alpha}{\partial\theta^\mu}\frac{\partial u_\beta}{\partial\theta^\nu}\right)\mathcal{M}^a_{\alpha\beta}(u)$ and $\sum_{\alpha,\beta}\left(\frac{\partial u_\alpha}{\partial\theta^\mu}\frac{\partial u_\beta}{\partial\theta^\nu}\right)\mathcal{M}^s_{\alpha\beta}(u)$ are tensors in parameter space with two lower indices that are expected to vary smoothly as their argument is changed, with no divergent or singular behavior, and eigenvalues that all take a characteristic scale. As such, we expect that as the critical point is approached the matrices eigenvalues will scale like:

$$\lambda_i^s \sim A\xi^{2y_i-d}$$
$$\lambda_i^a \sim A \qquad (6.36)$$

As the critical point is approached we expect the singular piece to dominate provided $2y_i - d \geq 0$. In the 2D Ising model, this is true for the magnetic field, which as the critical point is approached becomes the largest eigenvector $e_0 = \theta^h$ (with $y_h = 15/8$) and for the eigenvector given by $e_1 = \partial_\mu u_1$ whose eigenvalue is $y_1 = 1$ (in this case $2y_i - d = 0$ and there is a logarithmic divergence, as with the Ising model's specific heat). The remaining eigenvectors of the $g_{\mu\nu}$ are dominated by analytic contributions, where, just as in the diffusion equation viewed at its fundamental scale, we expect the eigenvectors to cluster together at a characteristic scale and not exhibit sloppiness (though not necessarily to be exactly the identity). This analysis seems to quantitatively agree with the Monte Carlo results plotted in figure 6.4.

127

6.6 Measuring the Ising metric after coarsening

The diffusion equation became sloppy only after coarsening. Viewed at its microscopic scale all parameters could be inferred with exactly the same precision. However, when observed at a time or length scale much larger than this microscopic scale a hierarchy of importance developed, with particle non-conservation being most visible, drift being the next most dominant term and the diffusion constant being the next most observable parameter. Further parameters became geometrically less important, justifying the use of an effective continuum model containing just the first of these parameters with a non-zero value.

What happens in the Ising model? Does a similar hierarchy develop? Do the 'relevant' parameters in the Ising model behave differently under coarsening from the irrelevant ones? To answer these questions we ask how well we could infer microscopic parameters of the model from data that is coarsened in space [13]. In particular, we restrict our measurements to observations of spins that remain after an iterative checkerboard decimation procedure (see figure 6.5 [14]). In the usual RG picture a new effective Hamiltonian is constructed that describes the observable behavior at these lattice sites. Here we instead calculate the Fisher Information in the original parameters, but only using information remaining at the new, coarsened level.

Specifically, we wish to measure $g_{\mu\nu} = -\left\langle \partial_\mu \partial_\nu \log\left(P(x^n)\right) \right\rangle$ where $x^n = \left\{s_{i,j}\right\}$ for $\{i, j\}$ in level n as defined in figure 6.5. We define the mapping to level

---

[13]there is no sense of 'time' in the Ising model, since it does not specify dynamics.

[14]We use this checkerboard decimation scheme rather than a block spin scheme (say) as it is easier to implement the Compatible Monte-Carlo described below.
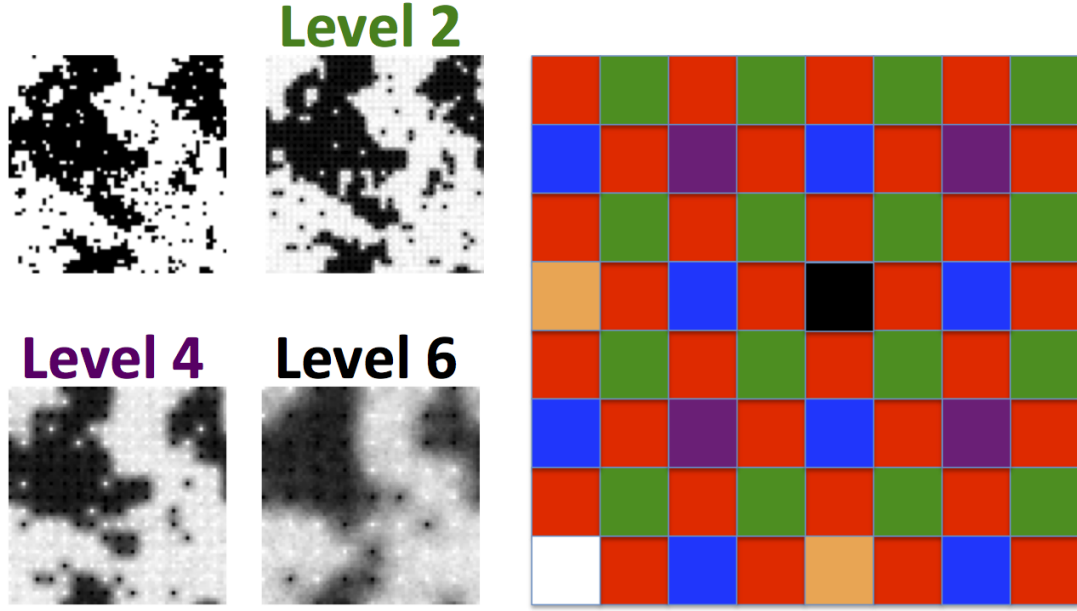
Figure 6.5: On the left, 'mean field' spin configurations are shown for ensembles that coarsen to the same state at a given level. In our implementation of iterative checkerboard decimation only a subset of spins can be observed while trying to infer parameters that describe the configuration of the entire spin ensemble. At level 0 all spins can be observed. At level 1 only the red spins can be observed. At level 2 only the green spins can be observed. At level 3 only the blue spins can be observed. Level 4 leaves purple spins, level 5 leaves orange spins and level 6 leaves just the black spin. This 8x8 chunk of lattice is tiled to make the full 64x64 bi-periodic lattice used in simulations, so that at level 6, for example, an observation is limited to an 8x8 lattice of remaining spins.

n, determined by the configuration of all spins x at level 0, as $x^n = C^n(x)$ [15]. It is useful to write $P(x^n)$ in terms of a restricted partition function :

$$P(x^n) = \tilde{Z}(x^n)/Z$$

$$\tilde{Z}(x^n) = \sum_x \exp(-H(x))\delta_{C^n(x),x^n} \tag{6.37}$$

where $\tilde{Z}(x^n)$ is the coarse-grained partition function conditioned on the sub-lattice at level n taking the value x^n while summing over the remaining degrees

---

[15]The mapping $C^n(x)$ here simply discards all of the spins that do not remain at level N, leaving an $L/2^{n/2} x L/2^{n/2}$ square lattice for even N and a rotated 'diamond' lattice for odd N. However, this formalism would also apply to other schemes, such as the commonly used block-spin procedure.

of freedom. We also introduce notation for an expectation value of an operator defined at level 0 over configurations which coarsen to the same configuration x^n

$$\{Q\}_{x^n} = \frac{\sum\limits_{x} Q(x)\delta_{C^n(x),x^n} \exp(-H(x))}{\tilde{Z}(x^n)} \tag{6.38}$$

We can now rewrite the metric at level n as:

$$\begin{aligned}
g^n_{\mu\nu} &= -\partial_\mu\partial_\nu \left\langle \log\left(P(x^n)\right)\right\rangle \\
&= \partial_\mu\partial_\nu Z - \left\langle \partial_\mu\partial_\nu \tilde{Z}(C^n(x))\right\rangle \\
&= g_{\mu\nu} - \left\langle \left\{\Phi_\mu\Phi_\nu\right\}_{C^n(x)}\right\rangle \\
&\quad + \left\langle \left\{\Phi_\mu\right\}_{C^n(x)} \left\{\Phi_\nu\right\}_{C^n(x)}\right\rangle \\
&= \left\langle \left\{\Phi_\mu\right\}_{C^n(x)} \left\{\Phi_\nu\right\}_{C^n(x)}\right\rangle - \left\langle \left\{\Phi_\mu\right\}_{C^n(x)}\right\rangle \left\langle \left\{\Phi_\nu\right\}_{C^n(x)}\right\rangle
\end{aligned} \tag{6.39}$$

This quantity $\left\langle \left\{\Phi_\mu(x)\right\}_{C^n(x)} \left\{\Phi_\nu(x)\right\}_{C^n(x)}\right\rangle$ can be measured by taking each member of an ensmble, x_q, and generating a sub-ensemble of $x'_{q,r}$ according to the distribution defined by:

$$P(x'_{q,r}|x_q) = \frac{\sum\limits_{x} \exp(-H(x))\delta_{C^n(x'_{q,r}),C^n(x_q)}}{\tilde{Z}(C^n(x))} \tag{6.40}$$

Techniques for generating this ensemble, using a form of 'compatible Monte-Carlo' [112] are discussed in section 6.7. From this ensemble we calculate:

$$g^n_{\mu\nu} = \frac{1}{(M^2 - M)(M'^2 - M')} \sum_{1<q,p<M,\ 1<r,s<M',\ q\neq p,\ r\neq s}^{M,M'} \Phi_\mu(x'_{q,r})\Phi_\nu(x'_{q,s}) - \Phi_\mu(x'_{q,r})\Phi_\nu(x'_{p,s}) \tag{6.41}$$

The results of this Monte Carlo presented for a 64×64 system at its critical point in figure 6.6. The irrelevant and marginal eigenvalues of the metric continue to behave much as the eigenvalues of the metric in the diffusion equation, becoming progressively less important under coarsening with characteristic eigenvalues. However, the large eigenvalues, dominated by singular
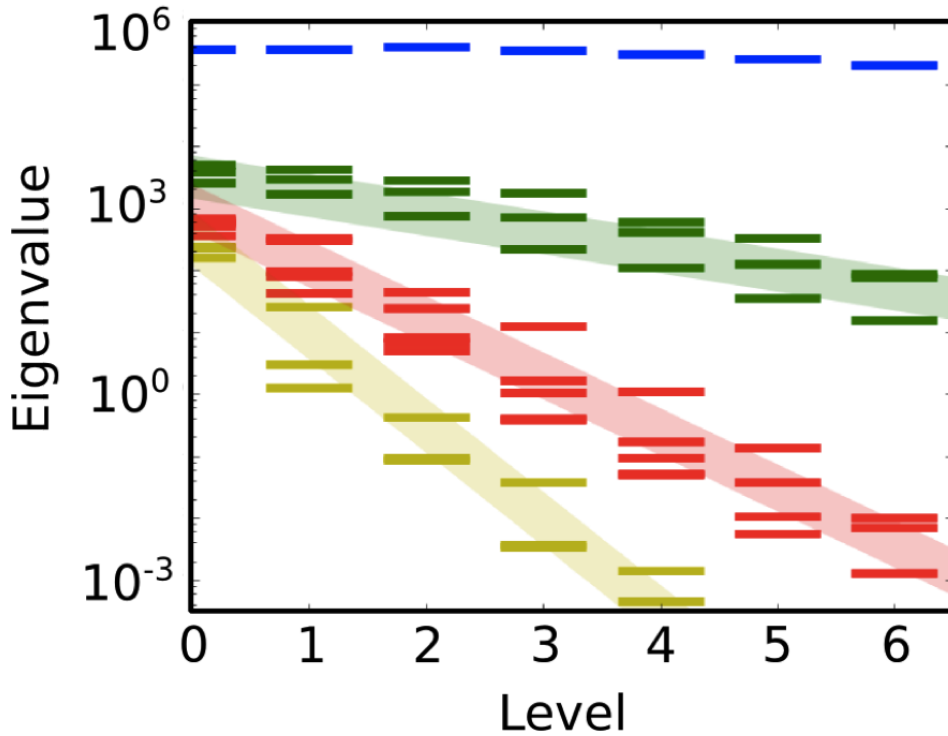
Figure 6.6: At the critical point the twelve dimensional subspace of eigenvlaues are plotted (the eigenvalue for θ^h is not shown) vs. the level of coarsening. The largest eigenvalue, which is dominated by a singular piece does not substantially shrink under coarsening. This means that the information from which we infer the temperature of the Ising model is carried in long wavelength modes, and is not lost under coarsening. All of the other eigenvalues shrink rapidly under coarsening, leading to a broad sloppy spectrum. Just as in the diffusion system, these irrelevant parameters decay with a characteristic power law which in section 6.6.1 we predict should scale like $\sqrt{2}^{\text{Level}(2y_i-d)}$, with irrelevant and marginal y_i in the Ising model taking the values 0 (line with predicted slope shown in green) -2 (line in red) and -4 (line in yellow)

corrections, do not become smaller under coarsening, presumably because they are measured by their collective effects on the large scale behavior, which is primarily measured from large distance correlations.

6.6.1 Eigenvalue spectrum after coarse-graining

To understand the values of the metric we observe after coarsening, we apply a more standard RG-like analysis to our system. We do this by constructing an effective Hamiltonian in a new parameter basis, repeating our analysis for the metric's eigenvalues in the coordinates of the parameters of that Hamiltonian, and finally transforming back into our original coordinates. After coarse-graining for n steps each observation yields the data $x^n = \left\{ s_{i,j} \right\}\Big|_{\{i,j\} \text{ in level n}}$ where only the spins $\{i, j\}$ remaining at level n are observed. The probability of observing x^n can be written:

$$P(x^n) = \frac{\exp\left(-H^n(x^n)\right)}{Z(A^n, u^n)} \tag{6.42}$$

where H^n is the effective Hamiltonian after n coarse-graining steps. H^n has new parameters most conveniently written in terms of the scaling variables defined in equation 6.33 where we can write $u_\alpha^n = b^{y_\alpha n} u_\alpha$. In addition, the area of the system is reduced to $A^n = b^{-dn} A$ [16] and $\partial u_\alpha^n / \partial \theta^\mu = b^{y_\alpha} \partial u_\alpha / \partial \theta^\mu$.

After rescaling the entropy of the model is smaller by an amount ΔS^n from the original model's entropy. It is customary in RG analysis to subtract this constant from the Hamiltonian, so as to preserve the Free energy of the system after rescaling:

$$F^n = F^{n,s} + F^{n,a} + \Delta S^n = F^s + F^a = F \tag{6.43}$$

Note that the new model's Hamiltonian would still be linear in these new parameters, allowing us to use the algebra of equation 6.12, if we were to remove the constant ΔS from the new Hamiltonian. This would of course be an identical model, since the addition of a constant does not change any observ-

---

[16] we keep our rescaling factor b general here, but in our system $b = \sqrt{2}$

ables. This change allows us to express the metric for the new observables, in terms of the original parameters, taking

$$g_{\mu\nu}^n(\theta) = \partial_\mu \partial_\nu (f^{n,s} + f^{n,a}) = \partial_\mu \partial_\nu (f^s + f^a - \Delta S) \tag{6.44}$$

After some algebra we see that:

$$g_{\mu\nu}^{s,n} = g_{\mu\nu}^s$$
$$g_{\mu\nu}^{a,n} = A \sum_{\alpha,\beta} \sqrt{2}^{(y_\alpha + y_\beta - d)n} \left(\frac{\partial u_\alpha}{\partial \theta^\mu} \frac{\partial u_\beta}{\partial \theta^\nu} \right) \mathcal{M}_{\alpha\beta}^a(u^n) \tag{6.45}$$

The singular piece is *exactly* maintained. This means that the singular piece of the free energy is exactly the piece which describes information carried in long wave-length information. On the other hand, the analytic piece is smaller by $\partial_\mu \partial_\nu \Delta S^n$. Thus, after n rescalings:

$$\lambda_i^{n,s} \sim A(\xi)^{2y_i - d}$$
$$\lambda_i^{n,a} \sim A b^{n(2y_i - d)} \tag{6.46}$$

To ensure that the Fisher information is strictly decreasing in every direction on coarsening [17] $g_{\mu\nu}^a$ must be negative semidefinite in the subspace of scaling variables where $2y_i - d > 0$. For these relevant directions, with $i = 0, 1$ $\lambda_i^n \sim A\xi^{2y_i - d} - b^{2y_i - d}n$, where the second term only becomes significant when $b^n \sim \xi$ (when the lattice spacing is comparable to the correlation length). For irrelevant directions, or relevant ones with $0 < 2y_i < d$ (corresponding to $i \geq 2$ in the Ising model), the analytic piece will dominate as the critical point is approached,

---

[17] In each coarsening step $g_{\mu\nu}^n - g_{\mu\nu}^{n+1}$ must be a positive semidefinite matrix. This is because no parameter combinations can be more measurable from a subset of the data available at level n than from its entirety.

133

yielding $\lambda_i \sim A b^{2y_i - d}$. These results are in quantitative agreement with those plotted in figure 6.6.

6.7 Simulation details

To generate ensembles x_p that are used to calculate the metric before coarsening we use the standard Wolff algorithm, implemented on 64x64 periodic square lattices. We generate $M = 10{,}000 - 100{,}000$ independent members from each ensemble, and calculate $g_{\mu\nu}$ as described above.

To generate the ensemble $x'_{p,r}$ we use variations on a method introduced in [112] which they termed 'compatible Monte-Carlo'[18]. Essentially, a Monte-Carlo chain is run with any move which proposes a switch to a configuration $x'_{p,r}$ for which $C^n(x'_{p,r}) \neq C^n(x_p)$ is summarily rejected. For us this means that no spins which remain at level n are ever allowed to be changed. We introduce several additional tricks to speed up convergence which we describe below.

Consider the task of generating a random member $x'_{p,r}$ for a given x_p at level 1. Because the spins which are free to move only make contact with fixed spins, each one can be chosen independently. As such, if we choose each 'free' spin according to its heat bath probability then we arrive at an uncorrelated member $x_{p,r}$ of the ensemble defined by x_p.

This trick can be further exploited to exactly calculate the contribution to a metric element at level 1 from a level 0 configuration x. In particular, by re-

---

[18]Ron, Swendsen and Brandt used this technique for entirely different purposes. They generated large equilibrated ensembles close to the critical point, essentially by starting from a small 'coarsened' lattice and iteratively adding layers to generate a large ensemble.

placing all of the spins with their mean field values, defined by $\tilde{s}_{i,j}(x) = \left\{ s_{i,j} \right\}_{C^n(x)}$ (which we can calculate in a single step) we can immediately write:

$$\left\{ \Phi_{\alpha\beta} \right\}_{C^n(x)} = \sum_{i,j} \tilde{s}_{i,j}(x) \tilde{s}_{i+\alpha, j+\beta}(x)$$

$$\{ \Phi_h \}_{C^n(x)} = \sum_{i,j} \tilde{s}_{i,j} \tag{6.47}$$

As such, it is possible to exactly calculate the level one quantities $\left\{ \Phi_\mu \right\}_{C^1(x)} \left\{ \Phi_\nu \right\}_{C^1(x)}$ for any microscopic configuration x and corresponding checkerboard configuration $C^1(x)$.

Beyond level 1 it becomes necessary to use compatible Monte-Carlo, but we can still take advantage of the independence of the free spins at level 1. In particular, we continue to leave the spins that are free at level 1 integrated out, so that we effectively make use of the level 1 partition function. This partition function is most conveniently written in terms of the number of up neighbors, $n^{up}_{i,j}$ that each *integrated out* spin has in the spins that do remain at level 1:

$$\log \tilde{Z}(C_1(x)) = \sum_{i,j \text{ not in level } 1} \log \left(z(n^{up}_{i,j}) \right)$$

$$z(n^{up}) = \cosh \left((\beta J)(2 - n^{up}) \right) \tag{6.48}$$

Additional spins that are not integrated out at level n are flipped using a heat bath algorithm (to avoid marching effects) with the ratio of partition functions in an 'up' vs 'down' configuration used to determine the transition probability. This is possible because these spins only interact with spins that are integrated out from level 1.

The probability of a spin (at level ≥ 2) transitioning to 'up' after being proposed from the down state is given by $z^{up}_{i,j}/(z^{up}_{i,j} + z^{down}_{i,j})$ with

$$z_{i,j}^{up} = \sum_{\{k,l\} \text{ n.n. of } \{i,j\}} z(n_{k,l}^{up} + 1)$$

$$z_{i,j}^{down} = \prod_{\{k,l\} \text{ n.n. of } \{i,j\}} z(n_{k,l}^{up})$$

$\qquad\qquad\qquad\qquad\qquad\qquad\qquad$ (6.49)

6.8 Conclusions

In this chapter we have explicitly seen the emergence of the ubiquitous sloppy spectrum from two microscopic models. In each case the model was not sloppy when all of its behavior could be observed perfectly. At this microscopic scale all of the parameters (in diffusion) could be measured to a similar level of accuracy. (In the Ising model two parameter combinations describing *emergent* properties already stood out at this microscopic scale). However, if we restricted ourselves to an experimentally feasible coarsened set of data, we found that rather than destroying all information equally, our coarsening selectively preserved just a small subset of the data, leading to a sloppy spectrum. Typical presentations of data selectively preserve or blur information about microscopic system parameters, leading to the ubiquitous sloppy spectrum seen in a wide range of effective models.

BIBLIOGRAPHY

[1] S. Amari and H. Nagaoka. *Methods of Information Geometry*. Translations of Mathematical Monographs. American Mathematical Society, 2000.

[2] PW Anderson. More is different - broken symmetry and nature of hierarchical structure of science. *Science*, 177(4047):393, 1972.

[3] R. G. Anderson and K. Jacobson. A role for lipid shells in targeting proteins to caveolae, rafts, and other lipid domains. *Science.*, 296(5574):1821–5., 2002.

[4] Nicholas L. Andrews, Keith A. Lidke, Janet R. Pfeiffer, Alan R. Burns, Bridget S. Wilson, Janet M. Oliver, and Diane S. Lidke. Actin restricts fc epsilon ri diffusion and facilitates antigen-induced receptor immobilization. *Nature Cell Biology*, 10(8):955–963, AUG 2008.

[5] L. A. Bagatolli, J. H. Ipsen, A. C. Simonsen, and O. G. Mouritsen. An outlook on organization of lipids in membranes: searching for a realistic connection with the organization of biological membranes. *Prog Lipid Res*, 49(4):378–89, 2010.

[6] T Baumgart, A T Hammond, P Sengupta, S T Hess, D A Holowka, B A Baird, and W W Webb. Large-scale fluid/fluid phase separation of proteins and lipids in giant plasma membrane vesicles. *Proc. Natl. Acad. Sci.*, 104:3165–3170, 2007.

[7] T. Baumgart, A.T. Hammond, P. Sengupta, S.T. Hess, D. Holowka, B.A. Baird, and W.W. Webb. Large-scale fluid/fluid phase separation of proteins and lipids in giant plasma membrane vesicles. *Proc. Natl. Acad. Sci. U.S.A.*, 104:3165–3170, 2007.

[8] CH Bennett. Efficient estimation of free-energy differences from monte-carlo data. *Journal Of Computational Physics*, 22(2):245–268, 1976.

[9] H. C. Berg and E. M. Purcell. Physics of chemoreception. *Biophysical Journal*, 20(2):193–219, 1977.

[10] W Bialek and S Setayeshgar. Physical limits to biochemical signaling. *Proc. Natl. Acad. Sci. USA*, 102(29):10040–10045, 2005.

[11] JM Boggs, T Yoong, and JC Hsia. Site and mechanism of anesthetic action .1. effect of anesthetics and pressure on fluidity of spin-labeled lipid vesicles. *Molecular Pharmacology*, 12(1):127–135, 1976.

[12] Daniel Bonn, Jakub Otwinowski, Stefano Sacanna, Hua Guo, Gerard Wegdam, and Peter Schall. Direct Observation of Colloidal Aggregation by Critical Casimir Forces. *Physical Review Letters*, 103(15), OCT 9 2009.

[13] R. Brewster, P. A. Pincus, and S. A. Safran. Hybrid Lipids as a Biological Surface-Active Component. *Biophysical Journal*, 97(4):1087–1094, AUG 19 2009.

[14] KS Brown, CC Hill, GA Calero, CR Myers, KH Lee, JP Sethna, and RA Cerione. The statistical mechanics of complex signaling networks: nerve growth factor signaling. *Physical Biology*, 1(3):184–195, SEP 2004.

[15] Theodore W. Burkhardt and Erich Eisenriegler. Casimir interaction of spheres in a fluid at the critical point. *Phys. Rev. Lett.*, 74:3189–3192, Apr 1995.

[16] H.C. Burstyn and J.V. Sengers. Decay rate of critical concentration fluctuations in a binary fluid. *Phys. Rev. A*, 25:448–465, 1982.

[17] B.A. Camley, C. Esposito, T. Baumgart, and F. L. H. Brown. Lipid bilayer domain fluctuations as a probe of membrane viscosity. *Biophys. J.*, 99(6):L44–L46, 2010.

[18] John Cardy. Boundary conformal field theory, 2008.

[19] John Cardy. Conformal field theory and statistical mechanics, 2008.

[20] S.A. Casalnuovo, R.C. Mockler, and W.J. O'Sullivan. Rayleigh-linewidth measurements on thin critical fluid films. *Phys. Rev. A*, 29:257–270, 1984.

[21] P.M. Chaikin and T.C. Lubensky. *Principles of Condensed Matter Physics*. University of Cambridge, Cambridge, 1995.

[22] G. R. Chichili and W. Rodgers. Cytoskeleton-membrane interactions in membrane raft structure. *Cell Mol Life Sci*, 66(14):2319–28, 2009.

[23] P. Cicuta, S.L. Keller, and S.L. Veatch. Diffusion of liquid domains in lipid bilayer membranes. *J. Phys. Chem. B*, 111(13):3328–3331, APR 7 2007.

[24] M. Combescot, M. Droz, and J. M. Kosterlitz. Two point correlation function for general fields and temperatures in the critical region. *Physical Review B*, 11(Copyright (C) 2010 The American Physical Society):4661, 1975.

[25] T.M. Cover and J.A. Thomas. *Elements of Information theory*. Wiley Interscience, New York, NY, 1991.

[26] Gavin E. Crooks. Measuring thermodynamic length. *Physical Review Letters*, 99(10), SEP 7 2007.

[27] P. Di Francesco, P. Matthieu, and P. Sénéchal. *Conformal Field Theory*. Springer-Verlag, New York, NY, 1997.

[28] C. Dietrich, L. A. Bagatolli, Z. N. Volovyk, N. L. Thompson, M. Levi, K. Jacobson, and E. Gratton. Lipid rafts reconstituted in model membranes. *Biophys J*, 80(3):1417–28, 2001.

[29] C. Dietrich, B. Yang, T. Fujiwara, A. Kusumi, and K. Jacobson. Relationship of lipid rafts to transient confinement zones detected by single particle tracking. *Biophysical Journal*, 82(1):274–284, 2002.

[30] M. A. Digman and E. Gratton. Imaging barriers to diffusion by pair correlation functions. *Biophys J*, 97(2):665–73, 2009.

[31] R. Dimova, C. Dietrich, A. Hadjiisky, K. Danov, and B. Pouligny. Falling ball viscosimetry of giant vesicle membranes: Finite-size effects. *Eur. Phys. J. B.*, 12(1):589–598, 1999.

[32] P.G. Dommersnes and J.-B. Fournier. N-body study of anisotropic membrane inclusions: Membrane mediated interactions and ordered aggregation. *The European Physical Journal B - Condensed Matter and Complex Systems*, 12:9–12, 1999.

[33] S. Doniach. Thermodynamic fluctuations in phospholipid bilayers. *Journal of Chemical Physics*, 68(11):4912–4916, 1978.

[34] M.J. Dunlavy and D. Venus. Critical slowing down in the two-dimensional Ising model measured using ferromagnetic ultrathin films. *Phys. Rev. B*, 71:144406, 2005.

[35] M. Edidin. The state of lipid rafts: from model membranes to cells. *Annu Rev Biophys Biomol Struct*, 32:257–83, 2003.

[36] Christian Eggeling, Christian Ringemann, Rebecca Medda, Guenter Schwarzmann, Konrad Sandhoff, Svetlana Polyakova, Vladimir N. Belov, Birka Hein, Claas von Middendorff, Andreas Schoenle, and Stefan W. Hell. Direct observation of the nanoscale dynamics of membrane lipids in a living cell. *Nature*, 457(7233):1159–U121, 2009.

[37] J. Ehrig, E. P. Petrov, and P. Schwille. Near-critical fluctuations and cytoskeleton-assisted phase separation lead to subdiffusion in cell membranes. *Biophys J*, 100(1):80–9, 2011.

[38] MB Elowitz, AJ Levine, ED Siggia, and PS Swain. Stochastic gene expression in a single cell. *Science*, 297(5584):1183–1186, 2002.

[39] Robert G. Endres, Olga Oleksiuk, Clinton H. Hansen, Yigal Meir, Victor Sourjik, and Ned S. Wingreen. Variable sizes of escherichia coli chemoreceptor signaling teams. *Molecular Systems Biology*, 4, 2008.

[40] C. Esposito, A. Tian, S. Melamed, C. Johnson, S. Y. Tee, and T. Baumgart. Flicker spectroscopy of thermal lipid bilayer domain boundary fluctuations. *Biophys J*, 93(9):3169–81, 2007.

[41] C. Esposito, A. Tian, S. Melamed, C. Johnson, S.-Y. Tee, and T. Baumgart. Flicker spectroscopy of thermal lipid bilayer domain boundary fluctuations. *Biophys. J.*, 93:3169–3181, 2007.

[42] Jun Fan, Maria Sammalkorpi, and Mikko Haataja. Domain formation in the plasma membrane: Roles of nonequilibrium lipid transport and membrane proteins. *Phys. Rev. Lett.*, 100(17), 2008.

[43] A. Filippov, G. Oradd, and G. Lindblom. The effect of cholesterol on the lateral diffusion of phospholipids in oriented bilayers. *Biophysical Journal*, 84(5):3079–86, 2003.

[44] M.E. Fisher. Renormalization of critical exponents by hidden variables. *Phys. Rev.*, 176:257–272, 1968.

[45] ME Fisher and PGD Gennes. Wall phenomena in a critical binary mixture. *Comptes Rendus Hebdomadeires Des Seances De L Academie Des Sciences Serie B*, 287(8):207–209, 1978.

[46] NP Franks and WR Lieb. Molecular mechanisms of general-anesthesia. *Nature*, 300(5892):487–493, 1982.

[47] NP Franks and WR Lieb. Do general-anesthetics act by competitive-binding to specific receptors. *Nature*, 310(5978):599–601, 1984.

[48] NP Franks and WR Lieb. Molecular and cellular mechanisms of general-anesthesia. *Nature*, 367(6464):607–614, FEB 17 1994.

[49] N. L. Gershfeld. The critical unilamellar lipid state: a perspective for membrane bilayer assembly. *Biochim Biophys Acta*, 988(3):335–50, 1989.

[50] A Gidwani, HA Brown, D Holowka, and B Baird. Disruption of lipid order by short-chain ceramides correlates with inhibition of phospholipase d and downstream signaling by fc epsilon ri. *Journal of Cell Science*, 116(15):3177–3187, 2003.

[51] T. Gil, J. H. Ipsen, O. G. Mouritsen, M. C. Sabra, M. M. Sperotto, and M. J. Zuckermann. Theoretical analysis of protein organization in lipid membranes. *Biochimica Et Biophysica Acta-Reviews on Biomembranes*, 1376(3):245–266, 1998.

[52] P.H. Ginsparg. Applied Conformal Field Theory. *Applied Conformal Field Theory, arXiv:hep-th/9108028*, November 1991.

[53] N. Goldenfeld. *Lectures on phase transitions and the renormalization group*. Addison-Wesley, NY, 1992.

[54] Byron Goldstein, Harold Levine, and David Torney. Diffusion limited reactions. *SIAM Journal on Applied Mathematics*, 67(4):1147–1165, 2006.

[55] R. E. Goldstein and N. W. Ashcroft. Origin of the singular diameter in the coexistence curve of a metal. *Physical Review Letters*, 55(20):2164–2167, 1985.

[56] D. Goswami, K. Gowrishankar, S. Bilgrami, S. Ghosh, R. Raghupathy, R. Chadda, R. Vishwakarma, M. Rao, and S. Mayor. Nanoclusters of gpi-anchored proteins are formed by cortical actin-driven activity. *Cell*, 135(6):1085–1097, 2008.

[57] G. Grinstein and Shang-keng Ma. Roughening and lower critical dimension in the random-field ising model. *Physical Review Letters*, 49(Copyright (C) 2010 The American Physical Society):685, 1982.

[58] SM Gruner and E Shyamsunder. Is the mechanism of general-anesthesia

related to lipid-membrane spontaneous curvature. *Annals Of The New York Academy Of Scienes*, 625:685–697, JUN 28 1991.

[59] R. N. Gutenkunst, J. J. Waterfall, F. P. Casey, K. S. Brown, C. R. Myers, and J. P. Sethna. Universally sloppy parameter sensitivities in systems biology models. *PLoS Computational Biology*, 3:1871–1878, 2007.

[60] M. Haataja. Critical dynamics in multicomponent lipid membranes. *Phys. Rev. E*, 80(2):020902(R), AUG 2009.

[61] H. Hao, R.A. Ferrell, and J.K. Bhattacharjee. Critical viscosity exponent for classical fluids. *Phys. Rev. E*, 71:021201, 2005.

[62] T. Harder and K. R. Engelhardt. Membrane domains in lymphocytes - from lipid rafts to protein scaffolds. *Traffic*, 5(4):265–275, 2004.

[63] WS Hlavacek, A Redondo, C Wofsy, and B Goldstein. Kinetic proofreading in receptor-mediated transduction of cellular signals: Receptor aggregation, partially activated receptors, and cytosolic messengers. *Bulletin of Mathematical Biology*, 64(5):887–911, 2002.

[64] P.C. Hohenberg and B.I. Halperin. Theory of dynamic critical phenomena. *Rev. Mod. Phys.*, 49(3):435–479, 1977.

[65] D Holowka, JA Gosse, AT Hammond, XM Han, P Sengupta, NL Smith, A Wagenknecht-Wiesner, M Wu, RM Young, and B Baird. Lipid segregation and ige receptor signaling: A decade of progress. *Biochimica et Biophysica Acta - Molecular Cell Research*, 1746(3):252–259, 2005.

[66] D. Holowka, E. D. Sheets, and B. Baird. Interactions between fc(epsilon)ri and lipid raft components are regulated by the actin cytoskeleton. *J Cell Sci*, 113 (Pt 6):1009–19, 2000.

[67] David Holowka, Dwaipayan Sil, Chikako Torigoe, and Barbara Baird. Insights into immunoglobulin e receptor signaling from structurally defined ligands. *Immunological Reviews*, 217:269–279, 2007.

[68] A.R. Honerkamp-Smith, P. Cicuta, M.D. Collins, S.L. Veatch, M. den Nijs, M. Schick, and S.L. Keller. Line tensions, correlation lengths, and critical exponents in lipid membranes near critical points. *Biophys. J.*, 95:236–246, 2008.

[69] A.R. Honerkamp-Smith, S.L. Veatch, and S.L. Keller. An introduction to critical points for biophysicists; observations of compositional heterogeneity in lipid membranes. *Biochim. Biophys. Acta*, 1788:53–63, 2009.

[70] Aurelia R. Honerkamp-Smith, Benjamin B. Machta, and Sarah L. Keller. Experimental Observations of Dynamic Critical Phenomena in a Lipid Membrane. *Physical Review Letters*, 108(26), JUN 28 2012.

[71] Aurelia R. Honerkamp-Smith, Sarah L. Veatch, and Sarah L. Keller. An introduction to critical points for biophysicists; observations of compositional heterogeneity in lipid membranes. *Biochimica et Biophysica Acta - Biomembranes*, 1788(1, Sp. Iss. SI):53–63, 2009.

[72] J. J. Hopfield. Kinetic proofreading - new mechanism for reducing errors in biosynthetic processes requiring high specificity. *Proc. Natl. Acad. Sci. USA*, 71(10):4135–4139, 1974.

[73] B.D. Hughes, B.A. Pailthorpe, and L.R. White. The translational and rotational drag on a cylinder moving in a membrane. *J. Fluid Mech.*, 110:349–372, 1981.

[74] Keiichiro Inaura and Youhei Fujitani. Concentration fluctuation in a two-component fluid membrane surrounded with three-dimensional fluids. *J. Phys. Soc. Jpn.*, 77(11):114603, NOV 2008.

[75] C Jarzynski. Nonequilibrium equality for free energy differences. *Physical Review Letters*, 78(14):2690–2693, 1997.

[76] L.P. Kadanoff and J. Swift. Transport coefficients near liquid-gas critical point. *Phys. Rev.*, 166(1):89–101, 1968.

[77] N. Kahya, D. Scherfeld, K. Bacia, B. Poolman, and P. Schwille. Probing lipid mobility of raft-exhibiting model membranes by fluorescence correlation spectroscopy. *Journal of Biological Chemistry*, 278(30):28109–28115, 2003.

[78] K. Kawasaki. Nonlocal shear viscosity and order-parameter dynamics near critical-point of fluids. *Phys. Rev. Lett.*, 29(1):48–51, 1972.

[79] Marc Kirschner and John Gerhart. *The plausibility of life : resolving Darwin's dilemma*. Yale University Press, New Haven, 2005.

[80] D.L. Kolin, D. Ronis, and P.W. Wiseman. k-space image correlation spectroscopy: A method for accurate transport measurements independent of fluorophore photophysics. *Biophys. J.*, 91:3061–3075, 2006.

[81] K. S. Korolev and David R. Nelson. Defect-mediated emulsification in two dimensions. *Phys. Rev. E*, 77:051702, May 2008.

[82] A. Kusumi, Y. M. Shirai, I. Koyama-Honda, K. G. Suzuki, and T. K. Fujiwara. Hierarchical organization of the plasma membrane: investigations by single-molecule tracking vs. fluorescence correlation spectroscopy. *FEBS Lett*, 584(9):1814–23, 2010.

[83] A. Kusumi and K. Suzuki. Toward understanding the dynamics of membrane-raft-based molecular interactions. *Biochim Biophys Acta*, 1746(3):234–51, 2005.

[84] J. Kwik, S. Boyle, D. Fooksman, L. Margolis, M. P. Sheetz, and M. Edidin. Membrane cholesterol, lateral mobility, and the phosphatidylinositol 4,5-bisphosphate-dependent organization of cell actin. *Proceedings of the National Academy of Sciences of the United States of America*, 100(24):13964–13969, 2003.

[85] J.B. Lastovka and G.B. Benedek. Spectrum of light scattered quasielastically from a normal liquid. *Phys. Rev. Lett.*, 17:1039–1042, 1966.

[86] Ilya Levental, Fitzroy J. Byfield, Pramit Chowdhury, Feng Gai, Tobias Baumgart, and Paul A. Janmey. Cholesterol-dependent phase separation in cell-derived giant plasma-membrane vesicles. *Biochemical Journal*, 424(Part 2):163–167, DEC 1 2009.

[87] Xuejing Li, David R. Serwanski, Celia P. Miralles, Ben A. Bahr, and Angel L. De Blas. Two pools of triton x-100-insoluble gabaa receptors are present in the brain, one associated to lipid rafts and another one to the post-synaptic gabaergic complex. *Journal of Neurochemistry*, 102(4):1329–1345, 2007.

[88] WR Lieb, M Kovalycsik, and R Mendelsohn. Do clinical-levels of general-anesthetics affect lipid bilayers - evidence from raman-scattering. *Biochemica Et Biophysica Acta*, 688(2):388–398, 1982.

[89] D. Lingwood, J. Ries, P. Schwille, and K. Simons. Plasma membranes are poised for activation of raft phase coalescence at physiological tempera-

ture. *Proceedings of the National Academy of Sciences of the United States of America*, 105(29):10005–10010, 2008.

[90] D. Lingwood and K. Simons. Lipid rafts as a membrane-organizing principle. *Science*, 327(5961):46–50, 2010.

[91] A. P. Liu and D. A. Fletcher. Actin polymerization serves as a membrane domain switch in model lipid bilayers. *Biophys J.*, 91(11):4064–70., 2006.

[92] J. L. Macdonald and L. J. Pike. A simplified method for the preparation of detergent-free lipid rafts. *J Lipid Res*, 46(5):1061–7, 2005.

[93] Benjamin B. Machta, Stefanos Papanikolaou, James P. Sethna, and Sarah L. Veatch. Minimal model of plasma membrane heterogeneity requires coupling cortical actin to criticality. *Biophysical Journal*, 100(7):1668–1677, APR 6 2011.

[94] Barry W. Connors Mark F. Bear and Michael A. Paradiso. *Neuroscience: Exploring the Brain*. Lippincott Williams and Wilkins, Maryland, 2001.

[95] F. R. Maxfield and M. Mondal. Sterol and lipid trafficking in mammalian cells. *Biochemical Society Transactions*, 34:335–339, 2006.

[96] K. A. Melkonian, T. Chu, L. B. Tortorella, and D. A. Brown. Characterization of proteins in detergent-resistant membrane complexes from madin-darby canine kidney epithelial cells. *Biochemistry*, 34(49):16161–70, 1995.

[97] Hans Meyer. Zur theorie der alkoholnarkose. *Naunyn-Schmiedeberg's Archives of Pharmacology*, 42:109–118, 1899. 10.1007/BF01834479.

[98] T. Mora and W. Bialek. Are Biological Systems Poised at Criticality? *Journal of Statistical Physics*, pages 135–+, June 2011.

[99] N. Morone, T. Fujiwara, K. Murase, R. S. Kasai, H. Ike, S. Yuasa, J. Usukura, and A. Kusumi. Three-dimensional reconstruction of the membrane skeleton at the plasma membrane interface by electron tomography. *Journal of Cell Biology*, 174(6):851–62, 2006.

[100] DB Mountcastle, RL Biltonen, and MJ Halsey. Effect of anesthetics and pressure on thermotropic behavior of multilamellar dipalmitoylphosphatidylcholine liposomes. *Proceedings of the National Academy of Sciences*, 75(10):4906–4910, 1978.

[101] S. Munro. Lipid rafts: elusive or illusive? *Cell*, 115(4):377–88, 2003.

[102] K. Murase, T. Fujiwara, Y. Umemura, K. Suzuki, R. Iino, H. Yamashita, M. Saito, H. Murakoshi, K. Ritchie, and A. Kusumi. Ultrafine membrane compartments for molecular diffusion as revealed by single molecule techniques. *Biophys J*, 86(6):4075–93, 2004.

[103] M. E. J. Newman and G. T. Barkema. *Monte Carlo methods in statistical physics*. Clarendon Press ; Oxford University Press, Oxford New York, 1999.

[104] E.P. Petrov and P. Schwille. Translational diffusion in lipid membranes beyond the Saffman-Delbruck approximation. *Biophys. J.*, 94(5):L41–L43, MAR 1 2008.

[105] L.J. Pike. Rafts defined: a report on the keystone symposium on lipid rafts and cell function. *J. Lipid Res.*, 47:1597, 2006.

[106] Michael Plischke and Birger Bergersen. *Equilibrium statistical physics*. World Scientific, Hackensack, NJ, 3rd edition, 2006.

[107] S. J. Plowman, C. Muncke, R. G. Parton, and J. F. Hancock. H-ras, k-ras, and inner plasma membrane raft proteins operate in nanoclusters with differential dependence on the actin cytoskeleton. *Proc Natl Acad Sci U S A*, 102(43):15500–5, 2005.

[108] S. J. Plowman, C. Muncke, R. G. Parton, and J. F. Hancock. H-ras, k-ras, and inner plasma membrane raft proteins operate in nanoclusters with differential dependence on the actin cytoskeleton. *Proc Natl Acad Sci U S A*, 102(43):15500–5, 2005.

[109] MJ Pringle, KB Brown, and KW Miller. Can the lipid theories of anesthesia account for the cutoff in anesthetic potency in homologous series of alcohols. *Molecular Pharmacology*, 19(1):49–55, 1981.

[110] Benedict J. Reynwar and Markus Deserno. Membrane composition-mediated protein-protein interactions. *Biointerphases*, 3(2):FA117–FA124, 2008.

[111] Benedict J. Reynwar, Gregoria Illya, Vagelis A. Harmandaris, Martin M. Mueller, Kurt Kremer, and Markus Deserno. Aggregation and vesicula-

tion of membrane proteins by curvature-mediated interactions. *Nature*, 447(7143):461–464, MAY 24 2007.

[112] D Ron, RH Swendsen, and A Brandt. Inverse Monte Carlo renormalization group transformations for critical phenomena. *Physical Review Letters*, 89(27), DEC 30 2002.

[113] G Ruppeiner. Riemanniam Geometry In Thermodynamic Fluctuation Theory. *Reviews Of Modern Physics*, 67(3):605–659, JUL 1995.

[114] J. Saarikangas, H. Zhao, and P. Lappalainen. Regulation of the actin cytoskeleton-plasma membrane interplay by phosphoinositides. *Physiol Rev*, 90(1):259–89, 2010.

[115] P.G. Saffman and M. Delbruck. Brownian motion in biological membranes. *Proc. Natl. Acad. Sci. U.S.A.*, 72(8):3111–3113, 1975.

[116] M. Schick. Membrane heterogeneity: Manifestation of a curvature-induced microemulsion. *Phys. Rev. E*, 85:031902, Mar 2012.

[117] P Schofield. Parametric representation of equation of state near a critical point. *Physical Review Letters*, 22(12):606, 1969.

[118] R. J. Schroeder, S. N. Ahmed, Y. Zhu, E. London, and D. A. Brown. Cholesterol and sphingolipid enhance the triton x-100 insolubility of glycosylphosphatidylinositol-anchored proteins by promoting the formation of detergent-insoluble ordered membrane domains. *Journal of Biological Chemistry*, 273(2):1150–7, 1998.

[119] D. Schwahn, K. Mortensen, and H. Yee-Madeira. Mean-field and ising critical behavior of a polymer blend. *Phys Rev Lett*, 58(15):1544–1546, 1987.

[120] Prabuddha Sengupta, Barbara Baird, and David Holowka. Lipid rafts, fluid/fluid phase separation, and their relevance to plasma membrane structure and function. *Seminars in Cell & Developmental Biology*, 18(5):583–590, 2007.

[121] Prabuddha Sengupta, David Holowka, and Barbara Baird. Fluorescence resonance energy transfer between lipid probes detects nanoscopic heterogeneity in the plasma membrane of live cells. *Biophysical Journal*, 92(10):3564–3574, 2007.

[122] James P. Sethna. *Statistical Mechanics: Entropy, Order Parameters, and Complexity*. Oxford Univ., Oxford, 2006.

[123] C. E. Shannon. A mathematical theory of communication. *Bell System Technical Journal*, 27(3):379–423, 1948.

[124] P Sharma, R Varma, RC Sarasij, Ira, K Gousset, G Krishnamoorthy, M Rao, and S Mayor. Nanoscale organization of multiple gpi-anchored proteins in living cell membranes. *Cell*, 116(4):577–589, 2004.

[125] ED Sheets, D Holowka, and B Baird. Critical role for cholesterol in Lyn-mediated tyrosine phosphorylation of Fc epsilon RI and their association with detergent-resistant membranes. *Journal of Cell Biology*, 145(4):877–887, MAY 17 1999.

[126] E.D. Siggia, B.I. Halperin, and P.C. Hohenberg. Renormalization-group treatment of critical dynamics of binary-fluid and gas-liquid transitions. *Phys. Rev. B*, 13(5):2110–2123, 1976.

[127] Dwaipayan Sil, Jong Bum Lee, Dan Luo, David Holowka, and Barbara Baird. Trivalent ligands with rigid dna spacers reveal structural requirements for ige receptor signaling in rbl mast cells. *ACS Chemical Biology*, 2(10):674–684, 2007.

[128] K. Simons and E. Ikonen. Functional rafts in cell membranes. *Nature*, 387(6633):569–72, 1997.

[129] K Simons and D Toomre. Lipid rafts and signal transduction. *Nature Reviews Molecular Cell Biology*, 1(1):31–39, 2000.

[130] T Sooksawate and M.A Simmonds. Effects of membrane cholesterol on the sensitivity of the gabaa receptor to gaba in acutely dissociated rat hippocampal neurones. *Neuropharmacology*, 40(2):178 – 184, 2001.

[131] O. Soubias, S. L. Niu, D. C. Mitchell, and K. Gawrisch. Lipid-rhodopsin hydrophobic mismatch alters rhodopsin helical content. *J Am Chem Soc*, 130(37):12465–71, 2008.

[132] M. M. Sperotto and O. G. Mouritsen. Mean-field and monte-carlo simulation studies of the lateral distribution of proteins in membranes. *European Biophysics Journal*, 19(4):157–168, 1991.

[133] PS Swain and ED Siggia. The role of proofreading in signal transduction specificity. *Biophysical Journal*, 82(6):2928–2933, 2002.

[134] H.L. Swinney and D.L. Henry. Dynamics of fluids near the critical point: Decay rate of order-parameter fluctuations. *Phys. Rev. A*, 8:2586–2617, 1973.

[135] C.J. Takacs, G. Nikolaenko, and D.S. Cannell. Dynamics of long-wavelength fluctuations in a fluid layer heated from above. *Phys. Rev. Lett.*, 100:234502, 2008.

[136] Gasper Tkacik and William Bialek. Cell biology: Networks, regulation, pathways, 2007.

[137] Gasper Tkacik, Curtis G. Callan, Jr., and William Bialek. Information flow and optimization in transcriptional regulation. *Proc. Natl. Acad. Sci. USA*, 105(34):12265–12270, 2008.

[138] Gasper Tkacik, Aleksandra M. Walczak, and William Bialek. Optimizing information flow in small genetic networks. i, 2009.

[139] Mark K. Transtrum, Benjamin B. Machta, and James P. Sethna. Why are Nonlinear Fits to Data so Challenging? *Physical Review Letters*, 104(6), FEB 12 2010.

[140] Mark K. Transtrum, Benjamin B. Machta, and James P. Sethna. Geometry of nonlinear least squares with applications to sloppy models and optimization. *Physical Review E*, 83(3, Part 1), MAR 3 2011.

[141] Y. Tserkovnyak and D. R. Nelson. Conditions for extreme sensitivity of protein diffusion in membranes to cell environments. *Proc Natl Acad Sci U S A*, 103(41):15002–7, 2006.

[142] W. L. C. Vaz, R. M. Clegg, and D. Hallmann. Translational diffusion of lipids in liquid-crystalline phase phosphatidylcholine multibilayers - a comparison of experiment with theory. *Biochemistry*, 24(3):781–786, 1985.

[143] Sarah L. Veatch, Ethan N. Chiang, Prabuddha Sengupta, David A. Holowka, and Barbara A. Baird. Quantitative Nanoscale Analysis of IgE-Fc epsilon RI Clustering and Coupling to Early Signaling Proteins. *Journal Of Physical Chemistry B*, 116(23):6923–6935, JUN 14 2012.

[144] Sarah L. Veatch, Ethan Nicholas Chiang, Prabuddha Sengupta, David A. Holowka, and Barbara A. Baird. Quantitative nano-scale analysis of ige-fcri clustering and coupling to early signaling proteins. *The Journal of Physical Chemistry B, In print*, 2012.

[145] Sarah L. Veatch, Benjamin B. Machta, Sarah A. Shelby, Ethan N. Chiang, David A. Holowka, and Barbara A. Baird. Correlation Functions Quantify Super-Resolution Images and Estimate Apparent Clustering Due to Over-Counting. *Plos One*, 7(2), FEB 27 2012.

[146] Sarah L. Veatch, Olivier Soubias, Sarah L. Keller, and Klaus Gawrisch. Critical fluctuations in domain-forming lipid mixtures. *Proc. Natl. Acad. Sci. USA*, 104(45):17650–17655, 2007.

[147] S.L. Veatch, P. Cicuta, P. Sengupta, A. Honerkamp-Smith, D. Holowka, and B. Baird. Critical fluctuations in plasma membrane vesicles. *ACS Chem. Biol.*, 3:287–293, 2008.

[148] S.L. Veatch, K. Gawrisch, and S.L. Keller. Closed-loop miscibility gap and quantitative tie-lines in ternary membranes containing diphytanoyl pc. *Biophys. J.*, 90:4428–4436, 2006.

[149] S.L. Veatch and S.L. Keller. Seeing spots: Complex phase behavior in simple membranes. *Biochim. Biophys. Acta*, 1746:172–185, 2005.

[150] S.L. Veatch, O. Soubias, S.L. Keller, and K. Gawrisch. Critical fluctuations in domain-forming lipid mixtures. *Proc. Natl. Acad. Sci. U.S.A.*, 104:17650–17655, 2007.

[151] J. Wang, C. A. Cerdeirina, M. A. Anisimov, and J. V. Sengers. Principle of isomorphism and complete scaling for binary-fluid criticality. *Phys Rev E Stat Nonlin Soft Matter Phys*, 77(3 Pt 1):031127, 2008.

[152] Joshua J. Waterfall, Fergal P. Casey, Ryan N. Gutenkunst, Kevin S. Brown, Christopher R. Myers, Piet W. Brouwer, Veit Elser, and James P. Sethna. Sloppy-model universality class and the Vandermonde matrix. *Physical Review Letters*, 97(15), OCT 13 2006.

[153] B Widom. Plait points in 2 and 3-component liquid mixtures. *J. Chem. Phys.*, 46(9):3324, 1967.

[154] M. Wu, D. Holowka, H. G. Craighead, and B. Baird. Visualization of

plasma membrane compartmentalization with patterned lipid bilayers. *Proc Natl Acad Sci U S A*, 101(38):13798–803, 2004.

[155] T.T. Wu, B.M. McCoy, C.A. Tracy, and E. Barouch. Spin-spin correlation functions for the two-dimensional ising model: Exact theory in the scaling region. *Phys. Rev. B.*, 13:316–374, 1976.

[156] M.C. Yalabik and J.D. Gunton. Monte carlo renormalization-group studies of kinetic Ising models. *Phys. Rev. B*, 25:534–537, 1982.

[157] A. Yethiraj and J. C. Weisshaar. Why are lipid rafts not observed in vivo? *Biophysical Journal*, 93(9):3113–3119, 2007.

[158] C. Yolcu, I. Z. Rothstein, and M. Deserno. Effective field theory approach to Casimir interactions on soft matter surfaces. *EPL*, 96(2), OCT 2011.

[159] Cem Yolcu, Ira Z. Rothstein, and Markus Deserno. Effective field theory approach to fluctuation-induced forces between colloids at an interface. *Phys. Rev. E*, 85:011140, Jan 2012.

[160] C. Yuan, J. Furlong, P. Burgos, and L. J. Johnston. The size of lipid rafts: an atomic force microscopy study of ganglioside gm1 domains in sphingomyelin/dopc/cholesterol membranes. *Biophys J*, 82(5):2526–35, 2002.

[161] Z. P. Zhang, M. M. Sperotto, M. J. Zuckermann, and O. G. Mouritsen. A microscopic model for lipid protein bilayers with critical mixing. *Biochimica Et Biophysica Acta*, 1147(1):154–160, 1993.

[162] B. Zheng. Erratum to "monte carlo simulations of critical dynamics with conserved order parameter" [phys. lett. a 277 (2000) 257]. *Phys. Rev. A*, 282:132, 2001.

[163] Etay Ziv, Ilya Nemenman, and Chris H. Wiggins. Optimal signal processing in small stochastic biochemical networks, 2006.

[164] J. A. Zollweg and Mulholla.Gw. Law of rectilinear diameter. *Journal of Chemical Physics*, 57(3):1021–, 1972.